Multiscale Modeling of Shock Wave Propagation through High Energetic Composites

by

Adam V. Duran

A dissertation submitted in partial fulfillment
of the requirements for the degree of
Doctor of Philosophy
(Aerospace Engineering)
in the University of Michigan
2017

Doctoral Committee:

Associate Professor Veera Sundararaghavan, Chair
Assistant Professor Karthik Duraisamy
Professor Adam J. Matzger
Associate Professor Henry Sodano

If you want to build a ship, don't drum up the men to gather wood, or divide the work and give orders. Instead, teach them to yearn for the vast and endless sea.

ANTOINE DE SAINT-EXUPERY, *THE WISDOM OF THE SANDS*

Adam V. Duran
avduran@umich.edu
ORCID iD: 0000-0003-3826-9104

To Adriana.

ACKNOWLEDGEMENTS

I first and foremost would like to thank my brilliant advisor, Professor Veera Sundararaghavan, for his support throughout my challenging academic career at Michigan. I appreciate all the time he gave me during our long pen and paper sessions where he facilitated any question, no matter how obvious or outrageous. His encouragement to pursue opportunities outside of the university allowed me to grow as an engineer and decide where to set my career goals. His personal advice allowed me to cope with the difficulties associated with academic life and helped me believe that I could accomplish anything. I will always be grateful for his unrelenting optimism.

I would like to acknowledge Professors Karthik Duraisamy, Adam Matzger, and Henry Sodano for joining my committee. I would also like to acknowledge the Defense Threat Reduction Agency, the National Science Foundation and the Rackham Graduate School for supporting my work through the years. I am thankful to the Department of Aerospace Engineering, in particular Denise Phelps, Michigan Advanced Research Computing and Computer Aided Engineering Network, in particular Amadi Nwankpa, for providing resources for my academics and research. I am thankful to the Mary A. Rackham Institute, in particular Colleen Carr and Nora Erickson.

I would like to thank both James Hwang and Professor Anthony Waas, for their contributions and advice on research outside the scope of this dissertation. I would like to thank my MSSL lab mates Abhishek, Jiangyi, Nick, Pinar,

Shang, Shardul, Siddhartha and Sriram for their encouragement, and my office mates Dave, Jonathan and Nick for keeping things interesting.

I am also grateful to my family and friends for their support. Thank you to my parents, Elizabeth and Juan, for showing me the meaning of hard work. Thank you to my sisters, Priscilla for traversing the difficult terrain for her younger siblings, and Amber for always being herself. Thank you to my in-laws, in particular Roy, Lilian, and Sonia, for making me feel welcome in the family. Thank you to my friends, Nabil for never letting me forget where I come from, and Weston for giving me someone to look up to.

Finally, and most importantly, I would like to thank my wife Adriana who has made this all possible. Thank you so much for keeping me safe, sane and allowing me to dream big. I love you and Duke forever.

TABLE OF CONTENTS

LIST OF FIGURES

LIST OF TABLES

LIST OF APPENDICES

ABSTRACT

This dissertation studies shock loading of Polymer-Bonded Explosives (PBXs) with varying degrees of microstructural information. PBXs are a class of multi-component solid-state composites consisting of energetic crystals (HMX) embedded in a polymeric binder and are used as propellants, munitions, fuel cell components and explosives for mining.

The rapid energy release involves tightly coupled nonlinear interactions between chemistry and mechanics. While the evolution and transfer of chemical energy to thermal and mechanical energy occurs at larger scales, decomposition and energy release take place at the molecular level. Between the molecular and continuum levels, material behavior is governed by the material microstructure; as the shock wave propagates through the energetic material, it is influenced by the particulate matrix interactions.

Typical hydrocodes that are currently used to simulate detonation of energetic composites do not explicitly model material heterogeneities. Continuum methods require the least amount of fidelity and use homogenized material properties. On the other end of the spectrum, Direct Numerical Simulation (DNS) explicitly models the microstructure and requires the highest amount of fidelity. A novel approach is introduced in this work which exploits the attractive features (speed/accuracy) of each method; the First-Order multiscaling approach incorporates micro-scale effects by using volume averaging schemes. A hydrocode was developed to study shock loading of PBXs for all methods.

The Eulerian hydrocode is based on the finite element method. The governing Euler Equations are solved using an explicit, one-step, second-order Taylor-Galerkin scheme. The solution procedure includes a high-resolution shock capturing scheme needed for numerical treatment of shocks. Continuum numerical results were validated by comparing to variety of experimental and numerical PBX results. To incorporate material heterogeneity effects, synthetic microstructures were generated using Markov Random Field (MRF) approach, with varying levels of material composition. Initiation of these microstructures and a continuum were studied for four different loading conditions.

Results shown that material behavior is significantly influenced by information from the microscale. In general, a continuum approach is less reactive than material models that include microscale information. For most loading conditions the continuum model was vastly different than the heterogeneous material systems and never achieved pressure, temperature and burn fractions values by those of the heterogeneous material systems. Although the continuum approach includes binder effects through material properties, this inclusion isn't sufficient to fully capture heterogeneous material behavior.

Loading conditions also played a role in material response. Uniformly distributed loading within regions known as "hot volumes" produced different responses for various material systems. Loading conditions with multiple interactions, not higher hot volumes, were found to have higher pressure and temperature outputs. Binder content affects heterogeneous material performance and safety. HMX heavy materials required less initiation energy and produced the highest temperature and pressure outputs, while binder heavy materials followed the opposite trend. These results showed material performance is at competition with material safety and have implications for material

by design.

Finally, First-Order Multiscale modeling showed promise in capturing the influence of heterogeneity on shock loading of PBXs. The multiscale approach compared well to high fidelity DNS results, especially for material systems with reduced heterogeneity, at the fraction of the cost associated with DNS. Applying the methodologies and techniques used in this dissertation to various PBX systems can allow materials to be designed and tailored to specific applications without having to run physical experiments.

CHAPTER 1

Introduction

1.1 Motivation

Polymer-bonded explosives (PBXs) are a class of multi-component solid-state composites consisting of energetic crystals and metal particles embedded in a polymeric binder. Unlike traditional fiber based composite structures, PBXs are designated as particulate composites. They are comprised of a thermoplastic, typically $5 - 20\%$ of the formulation by weight, and organic explosive crystals, such as cyclotetramethylene-tetranitramine (HMX) [1] which contains fuel and oxidizer needed for combustion processes. These energetic materials react rapidly producing expanding gaseous products, at high pressures and temperatures, and consequently are used as propellants, munitions, fuel cell components and explosives for mining. The rapid energy release (detonation) involve tightly coupled nonlinear interactions between chemistry and mechanics which produce a self-sustaining shock wave. These detonation waves have extreme features; they travel at typical speeds of thousands of meters per second, the reaction zone is a few hundred micrometers wide, the reaction times are of the order of microseconds and the peak pressures can reach about $100GPa$ [2]. Given the extreme nature of this phenomena there is significant interest in material performance and, more importantly, safety (accidental detonation).

These two material behaviors, however, are heavily influenced by the material heterogeneities. As the shock wave propagates through the energetic material, it is influenced by the particulate matrix interactions. While the evolution and transfer of chemical energy to thermal and mechanical energy occurs at larger scales, decomposition and energy release take place at the molecular level. Between the molecular and continuum levels, material behavior is governed by the material microstructure [3–7]. Consequently there is great interest in energetic materials by design; i.e. controlling the shock wave by manipulating the microstructure.

However, energetic materials by design has many challenges. There is a great amount

of resources needed to develop PBXs. Manufacturing restrictions and safety concerns affect development time and, thus, experimental studies of detonation phenomena are expensive and sometimes impossible. Numerical methods have become a useful alternative method of solution, which, if carefully used, can assist in the design of explosives. Typical hydrocodes that are currently used to simulate detonation of energetic composites do not explicitly model material heterogeneities. The aim of this work is to begin the construction of a multiscale model hydrocode, for shock loading of PBXs, that incorporates material microstructure information and will ultimately aid in the expedition of the development process.

1.2 Detonation Physics

Explosives are materials that release energy at exceedingly rapid rates. Fundamentally, their behavior is a result of the coupling between the well-developed fields of fluid mechanics and chemistry. In the past, explosive science was relatively primitive and relied heavily on empirical observations. Recently, however, modern diagnostic techniques [8] and computational technologies have encouraged growth in the understanding of explosives.

Explosives may be categorized by the rate at which the material expands: low or high explosives [9]. Low explosives expand at subsonic speeds (deflagration), while high explosives, expand at supersonic speeds through a shock wave (detonation). High explosives may be classified further by their sensitivity to mechanical or thermal insult [10]. High explosives that are extremely sensitive to heat, shock and electrical discharge are known as primary explosives. High explosives that require a shock of another explosive or a high-energy impulse in order to detonate are known as secondary explosives. Secondary high explosives include additives such as metals, binders and plasticizers, and are the focus of this work.

The distinguishing feature of detonation is the self-sustaining shock wave maintained by the inertia of the explosive itself. Shock waves are compression wave fronts where the flow across the front results in an abrupt change of state [11]. The shock process is irreversible and is associated with a steep pressure rise nearing a discontinuity in fluid properties. Shock waves may propagate through both reactive and inert liquids or solids. During detonation, the material in front of the wave is unaffected until the detonation wave passes through it as the wave front separates stationary materials from material in motion. Just behind the wave front, pressures and temperatures are extremely high and are produced by the rapid energy release in the explosive; waves travel at speeds on the order

of kilometers per second, pressures are on the order of tens of gigapascals, temperatures range from $2000 - 4000K$, and 90% of chemical reaction is complete within $10^{-6} - 10^{-9}$ seconds [12]. A detonation wave precedes and is driven by the zone of chemical reaction, in turn creating high pressures and temperatures necessary to drive chemical reaction. This coupling provides the necessary conditions to maintain fast chemical reaction and thus the self-sustaining propagation of the detonation wave.

The detonation wave largely depends on the composition and initiation of the explosive. Explosives with uniform composition are known as homogeneous explosives and are typically liquid explosives, such as nitromethane, FEFO, IPN, and hydrogen peroxide/water [13, 14]. Initiation of the detonation wave occurs via shock heating from compression and thermal explosion at the interface between the material and an impactor. This creates a super detonation that eventually overtakes the initial shock front. Eventually the shock is overdriven and steady detonation is reached. This process is illustrated in Fig. 1.1. The wave travels at a constant velocity, heating the material to a bulk temperature. In order to detonate, the bulk material must be heated above the activation energy; therefore, homogeneous explosives are less sensitive.

Explosive materials whose composition varies spatially are known as heterogeneous explosives and are the focus of this work [15–18]. These materials are not heated uniformly to a bulk temperature. Instead hot regions (hot spots) build in various locations due to shock loading of the microstructure. Hot spot mechanisms have been studied in explosives [19, 20] and in the context of engines [21]and propellants [22] as a crucial mechanism in initiation. The collective interactions of hot spots results in energy release close to the shock front, resulting in an increase in pressure and temperature. This localized energy continuously accelerates the shock front until the shock-to-detonation transition occurs as shown on Fig. 1.1. This transition can be measure as the run-to-detonation and can be measured in distance or time.

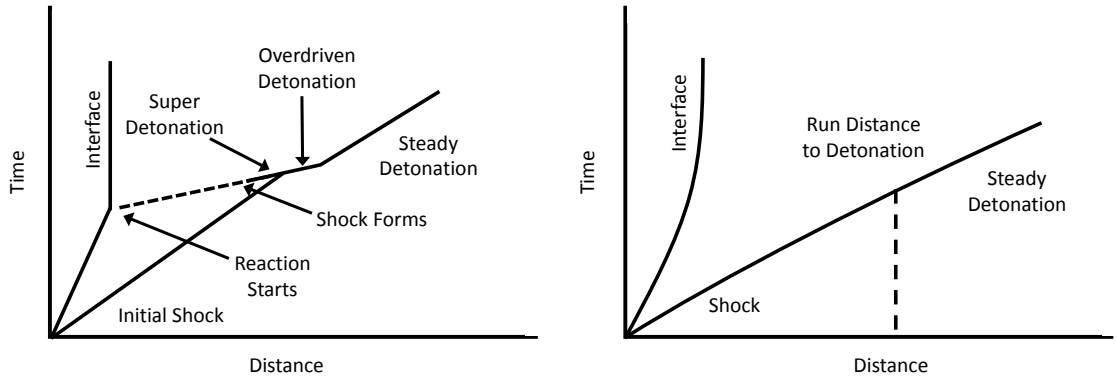

Figure 1.1: Shock-to-detonation transitions for homogeneous explosives(left) and heterogeneous explosives(right).

Run-to-detonation is the main measurement used to assess an explosive's sensitivity and is calculated as a function of input pressure [23]. It is determined experimentally by embedding gauges within the explosive at multiple points. The material is then shocked with an impactor and the shock-to-detonation wave profiles are measured. Note, as the shock waves propagate through the material, the embedded gauges move with the material. From these reactive wave profiles, the location or time at which the explosive reaches steady detonation is determined. As an example, the wave profiles for a heterogeneous explosive with five embedded gauges are shown on the left of Fig. 1.2. The y-axis represents pressure and the x-axis represents time. The initial pressure can be measured from the first gauge at $x1$. The shock wave strengthens at gauges $x2$ and $x3$ as chemical reaction occurs until steady detonation is reached by the time the wave reaches the gauges located at $x4$ and $x5$. From the plot, it can be determined that the run-to-detonation distance lies between gauges located at $x3$ and $x4$. This experiment is repeated for various input pressures, each corresponding to different run-to-detonation quantities.

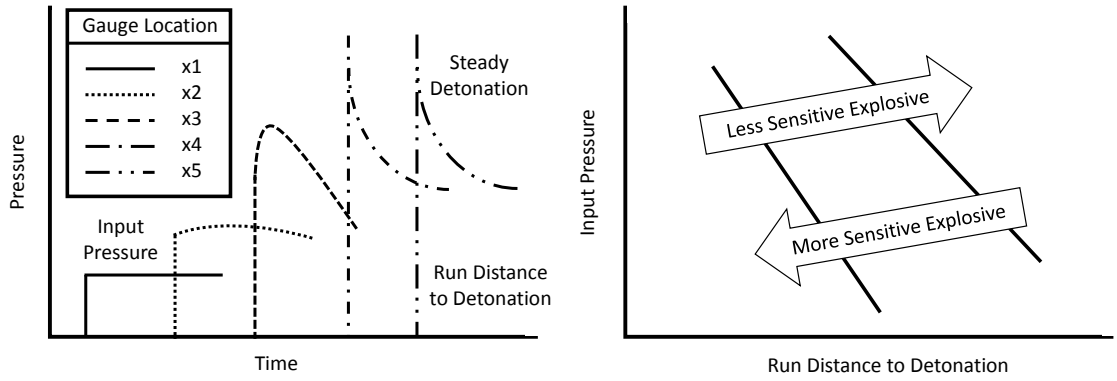

Figure 1.2: Run-to-detonation example with shock wave profiles(left) and Pop plot(right).

The data generated from these experiments are used to make Pop-plots, logarithmic plots of run-to-detonation distance versus incident shock [24]. When the data is plotted in a logarithmic scale the relationship between run-to-detonation and incident pressure appears linear as shown on the right of Fig. 1.2. Pop-plots for various explosives can be quite different from each other. In this example two explosives are shown, each represented by a solid line, with varying sensitivity. As input pressure increases, run-to-detonation decreases. For the same input pressure, the explosive on the left has a shorter run-to-detonation than the explosive on the right. This means that the explosive on the left is more sensitive than the explosive on the right; i.e. less energy is required for the explosive on the left to detonate when compared to the explosive on the right. When presented this way (pressure on the y-axis and run-to-detonation on the x-axis) explosives occupying the right side of the Pop-plot are less sensitive than those occupying the left side.

1.3 Hydrocodes

Large computer programs, known as hydrocodes, are typically used to simulate large deformations of materials in response to dynamic processes [25–27]. Initially developed in national laboratories for defense problems, these codes have grown in complexity and sophistication and are used in various fields. Hydrocodes are used for problems in penetration mechanics, fracture mechanics, astronomy [28] and, in particular, have become a useful tool for blast and detonation analysis by providing insight into phenomena observed in experiments. Many well-developed codes, including CTH [29] DYNA [30, 31], EPIC [32] and PRONTO [33, 34], solve the continuum equations for the nonlinear response of dynamic materials. Like computational fluid dynamics codes (CFD), hydrocodes solve the Euler equations for the conservation of mass, momentum, energy and species. Hydrocodes differ from CFD codes in their use of advanced equations of state to model solids in addition to liquids and gases. Coupled with a method for dealing with shock discontinuities, hydrocodes allow shock compression of realistic materials to be simulated in complex engineering geometries. Accuracy of hydrocodes demands high resolution of the smallest scale; the chemical reaction zone must be resolved accurately, for it is the very mechanism that sustains the leading shock. Hydrocodes are based on Eulerian or Lagrangian methods.

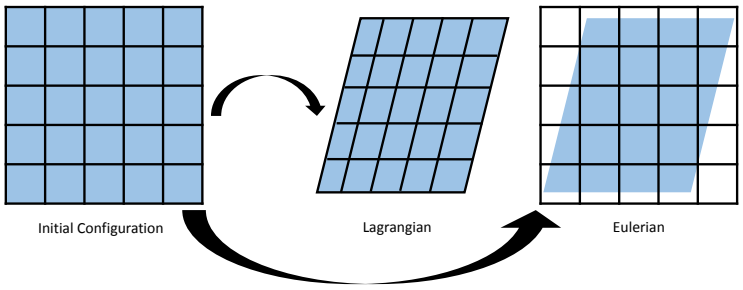

Figure 1.3: Lagrangian and Eulerian descriptions; Lagrangian mesh deforms while Eulerian mesh remains fixed

The Lagrangian description moves with the fluid at the fluid velocity while the Eulerian description has the fluid moving through it [35]. This is depicted in Fig.1.3 where the Lagrangian description in shown in the center, the Eulerian description is shown to the right and the fluid and mesh are represented in blue and black respectively. In the Lagrangian or material description, one would calculate fluid properties at the moving points attached to the material for each point in time. Mass within the cell is invariant, but the volume of the cell changes due to the expansion and compression of the material. However, in the Eulerian or spatial description, one would calculate fluid properties at the fixed points of the grid at all points in time. The cell volume is invariant since the points and cell boundaries remain fixed in space. While the Lagrangian codes allow materials to remain pure (due to moving interfaces) Eulerian codes are attractive in that the spatially-fixed mesh allow for arbitrarily large deformations; Lagrangian grids may distort without bound and become unsolvable. Therefore, the Eulerian description is used in the work. These methods can be combined to take advantage of each description. Arbitrary Lagrangian Eulerian (ALE) methods perform a Lagrangian time step and follows with a remap step that maps the solution from the distorted Lagrangian mesh on to the spatially-fixed Eulerian mesh [36].

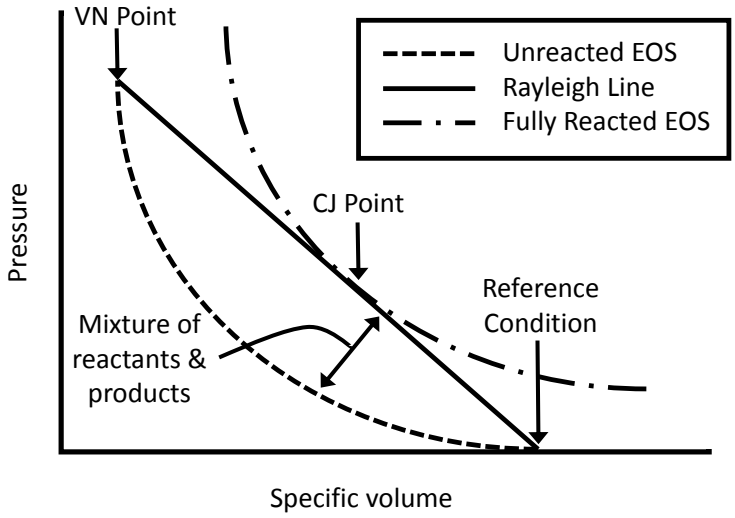

Figure 1.4: Curves for CJ and ZND detonation theories. Equations of state for solid unreacted explosive and fully gaseous products, with Rayleigh line, CJ point and VN point.

Hydrocode models are based on the CJ and ZND detonation theories. The CJ theory, developed by Chapman [37] and Jouguet [38], provides a framework for inferring material properties from detonation experiments by relating the detonation wave velocity to the properties of the gases behind the detonation wave front. The theory assumes that as the detonation front passes through the material, the explosive goes from an unreacted material to fully reacted gaseous products instantly. This produces a self-sustaining shock wave traveling at a constant velocity. The material properties for the detonation products are represented as an equation of state on Fig.1.4. In this figure, the y-axis represents pressure and the x-axis represents specific volume. A straight line is drawn from the initial reference condition (unreacted material) and runs tangent to the fully reacted gaseous products equation of state curve. This line is the Rayleigh line, whose slope represents the constant detonation velocity. The point at which the Rayleigh line runs tangent to the reacted gaseous products equation of state curve is known as the "CJ" point; the unique point necessary for stable detonation. Programmed burn hydrocode models uses the CJ theory as its basis and is advantageous due to its computational cost [39]. Programmed burn initially prescribes the features of the detonation front where a synthetic chemical reaction zone is used and the reaction rate is assumed to be constant. As a result, the state of the explosive at the end of the reaction zone is computed at a relatively modest cost.

The ZND theory, developed by Zeldovich [40], von Neumann [41] and Doering [42], is an extension of CJ theory and accounts for the finite time required for chemical reaction to occur, a more realistic assumption. It assumes that as the detonation wave shocks the unreacted material, chemical reaction begins to occur transforming the solid material into

gaseous reaction products. During this process, there exists a finite reaction zone where the explosive is partially reacted. This process is depicted on Fig.1.4 where the solid unreacted equation of state is additionally required. Note, the area between the both equation of state curves represents the partially-reacted explosive. The ZND theory assumes that the Rayleigh line extends passed the CJ point and intercepts the solid unreacted equation of state at the von Neumann point. To initiate the explosive, the solid material is shocked to the von Neumann point. As chemical reaction occurs, pressure decreases along the Rayleigh line, through the partially-reacted region until it reaches the CJ point, the point where all reaction has occurred. Reactive burn model use ZND theory as its basis and assumes a finite chemical reaction rate to be pressure, temperature or entropy-dependent [43–46]. These rates rely heavily on empirical data, indicating the difficulties associated in predicting the response of energetic materials under shock loading. This work uses reactive burn models.

1.4 Polymer-Bonded Explosives

Polymer-bonded explosives (PBXs) are a class of multi-component (heterogeneous) solid-state composites consisting of energetic crystals (HMX) and metal (Al) particles embedded in a polymeric binder (e.g. estane). PBX's are pressed from molding powders using several techniques and methods [47]. One such method is the slurry technique in which a crystalline explosive is agitated in a closed container with water. A plastic solvent is added to the container and wets the crystalline surfaces. The solvent is removed by distillation allowing the plastic phase to precipitate on the explosive as a coating, creating plastic-explosive beads. This process continues until the solvent and water is removed, producing a molding powder. PBX molding powder can be pressed using fluid pressure (i.e. hydrostatic pressure) to obtain densities up to 97% of the theoretical density. The final shape of the explosive is machined similar to that of conventional plastics.

The characteristics and classifications of PBXs depends on the polymeric coating, typically 5 to 20 of each formulation by weight, that binds the explosive and the amount of energetic crystals [48]. As an example, PBX 9404 is 94% HMX by weight with the remaining composition consisting of the plasticizers, nitrocellulose and tris-beta chloroethylphosphate, and the stabilizer diphenylamine. PBX 9501 is 95% HMX by weight with the remaining composition consisting of Estane and bis(2,2-dinitropropyl)acetal and bis(2,2-dinitropropyl)formal. Materials properties and models for both of these components are considered in this work.

A common organic explosive crystals, an the one considered in this work, is 1,3,5,7-Tetranitro-1,3,5,7-tetraazacyclooctane [49], commonly known as Octogen or HMX (high

melting explosive). HMX crystals are round and approximately isotropic, containing both fuel and oxidizer components needed for combustion processes. HMX is the most powerful military explosive in current use; compared to the common cast munition trinitrotoluene (TNT), HMX-based PBXs are stronger [50]. Consequently, the cost of production is higher when compared to other explosives (e.g. RDX) and is therefore restricted to military applications for use as high performance propellants and explosives. As with any explosive, there is risk for premature detonation of HMX. The use of explosives in a polymeric matrix greatly reduces sensitivity and, thus, risk of premature detonation from impact and friction.

The polymeric matrix, or binder, consists of both a polymer and a plasticizer [51]. While providing good energy absorbing properties, lowering the vulnerability of the overall explosive, binders are difficult to recover and demilitarize. Binder may be inert or energetic. Inert binders, such as like hydroxy-terminated polybutadiene (HTPB), contributes no energy to the explosive decreasing the sensitivity and, therefore decreasing the overall performance of the explosive. Energetic binders, such as glycidyl azide polymer (GAP), poly(3-nitratomethyl-3-methyloxetane) (polyNIMMO) and poly(glycidyl nitrate) (polyGLYN), increase the energy output of the explosive at the expense of safety. This work assumes that the polymeric binder is energetic or reactive.

The formulation of the binder affects the hardness, stability and safety of the explosive. Soft PBXs are susceptible to creep and lack strength, while brittle PBXs can sustain damage in normal handling and succumb to thermal shocks [52]. However, in general, PBXs are relatively safe to handle as the polymer absorbs shock and reduces sensitivity to accidental detonation. This, and the fact that the binder provides mechanical rigidity and dimensional stability makes PBXs highly malleable. Typical machining methods and tools, such as CNC machines, band saws and lathes can be used with care [53]. Recently, advanced manufacturing techniques, such as 3-d printing, have been studied [54] laying groundwork for the maximum control of material composition and sophisticated geometry.

While decomposition and energy release take place at the molecular level, the evolution and transfer of chemical energy to thermal and mechanical energy occurs at much larger scales. Between the molecular and continuum levels, material behavior is greatly influenced by the material heterogeneities (the microstructure). The microstructure's complicated geometry arises from the manufacturing process where a mixture of fine and coarse energetic crystals with random orientations are coated with a thin layer of polymeric binder. The manufacturing process has an effect on energetic crystal size [55, 56], and may produce microscale features like cracks [57]. The microstructure can be obtained experimentally [58] using methods such as Polarized Light Microscopy (PLM), Scanning Electron Microscopy (SEM), and small angle neutron scattering (SANS). A binary representative

microstructure is illustrated on Fig. 1.5 with the black regions depicting the energetic crystals and white regions depicting the polymeric binder. Energetic crystals vary in both size and orientation. The schematic shows a mixture of both fine and coarse energetic crystals with diameters ranging from 1 -1000μm. The height of Fig. 1.5 is approximately $0.5mm$.

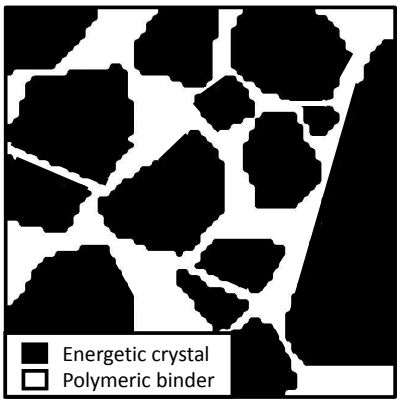

Figure 1.5: Binary schematic of typical PBX microstructure. Energetic crystals(black) range from 1 -1000μm in diameter. Polymeric binder(white) is typically 5 to 20% of the material by weight. The scale of the figure is approximately $0.5mm$.

A large body of experimental work in this area indicate the importance of these features. Crystal size effects are known to have an influence on the sensitivity and performance of PBXs. Smaller HMX particles have lesser run times to detonation than larger particles [3]. However, large grains are more sensitive than small grains at low pressures, while small grains are more sensitive at high pressures [4]. Adding aluminum (Al) content to the composition decreases detonation velocity while increasing heat of explosion [5]. Finer Al particles increase the acceleration ability of the explosive; nanoparticles of Al achieve higher peak pressures and detonation velocities [6]. The polymeric matrix affects the time to detonation, as it increases with the strength and content of the binder [7]. Porosity is also known to have an effect on run-to-detonation of PBXs [48] as pore collapse creates hot spots, the main mechanism for initiation in heterogeneous explosives (Section 1.2). However, other hot spot mechanisms exist such as critical hot spots [59]. Critical hot spots are areas of the explosive that are large and hot enough to initiate the surrounding cooler explosive. Another mechanism responsible for hot spots is the shock heating of crystals and binder.

1.5 Modeling of PBXs

Detonation in PBXs initiate with a rapid shock wave. The reaction zone must be resolved accurately, for it is the very mechanism that sustains the leading shock. Accurate simulation of the reaction zone entails bridging the length and time scales associated with microstructure evolution, reaction kinetics and mass transport. For example, the time scale associated with the reactive flow is several magnitudes of time larger than the times associated with the chemical reactions. The remedies proposed include high resolution grids in the reaction zone [60] and time-operator splitting to deal with source terms with different time scales [61]. However, these numerical techniques do not fully model the physicochemical aspects of detonation phenomena. With the advent of parallel computing power, it may now be possible to resolve these aspects using fine-scale simulations.

At the nano-scale, Ab-initio (quantum mechanical) [62] and molecular dynamics [63] studies have been used to study the chemical mechanisms involved in HMX decomposition. MD simulations have also been used, along with reactive force fields calibrated from quantum mechanical calculations, to model detonation waves and chemical kinetics [64, 65]. The conventional non-equilibrium MD approach involves creating a shock on one side of the simulation cell and propagating the shock to another side, but the simulation time is limited by the time to reach the other side (in order to avoid shock reflection). The quality of MD simulations depends on a number of factors including the representation of the force field [66]. New types of shock simulation techniques have been developed that constrain the computational cell to jump conditions across the shock [67, 68]in order to realize larger simulation times. These methods constrain the energy, velocities or stress in the simulation cell to converge to the thermodynamic jump conditions across a shock. Recently, a multi-scale shock technique (MSST [69]) has been proposed that combines atomistic simulations with the Euler equations to achieve longer simulation times and length scales. However, these new methods do not scale to level of the microstructure (micro-scale consisting of grains, particles) where other physical features such as localized heating, formation of hot spots [70] and interaction between particles need to be considered. However, MD methods are useful to compute thermophysical parameters such as strength and conductivity [71–75] that can be used in micro- and meso- scale simulations.

At the micro-scale, studies have been performed that include models for microstructural information (e.g. grain size). These models include the statistical hot spot models [76, 77], stochastic material attribute models [78] and the mixture model [79]. The microstructure may also be represented explicitly. Studies have been performed using discretized microstructures solved within multi-material hydrodynamics computer codes described in

Section 1.3. Coupled with a method for dealing with shock discontinuities, hydrocodes allow shock compression of realistic materials to be simulated in complex engineering geometries. In this work, the use of hydrocodes at the microstructural scale is termed "direct numerical simulation"(DNS). This is done to differentiate this approach to the conventional method of modeling PBXs as a homogenized material within a hydrocode. The homogenized approach is termed the "continuum". This model does not explicitly model material heterogeneities and, therefore, does not require high fidelity. For comparison, note that the mesh sizes of continuum-scale models are of the order of 100 micrometers while the mesh size in the micro-scale model is about 0.1 micrometers (which resolves the crystalline aggregate).

DNS simulations of PBXs have been performed for numerous experiments using a variety of computational methods and models. The response of HMXestane microstructures, with varying volume fractions, to transient stress waves has been studied using a cohesive finite element framework [80]. Split Hopkinson Pressure Bar (SHPB) measurements for PBX9501 has been numerically studied using Mori–Tanaka models [81, 82] . The response of PBX9501 has also been measured for weak shock using discrete element [83] and particle-in-cell methods. [84, 85]. Both Eulerian and Lagrangian hydocodes have been used to study the compaction of granular HMX [86–88]. However, the focus of this work is modeling shock propagation and detonation of PBXs. This phenomena has been investigated previously in the following studies. High resolution three-dimensional simulations of shock loading on heterogeneous materials found that hot spots are strongly influenced by multiple crystal interactions [89, 90]; inter-granular voids in porous HMX leads to greater deformation of the grains and higher temperatures. These types of simulations provide detailed insight into hot spots size [70] and mechanisms such as pore collapse [91]. High resolution simulation data like this was then used to determine statistical and mean properties of the shock fields [92]. Two-dimensional simulations of shock loading has also been studied and has provided insight into ignition times associated with hot spot temperatures [93] and the hot spot criteria for polymeric binders [94]. In this work, three-dimensional and two-dimensional DNS simulations will be studied.

Ideally all length and time scales associated with shock loading of PBXs can be simulated and coupled. That is, when the material is shocked at the continuum-scale, the traveling detonation wave creates high pressures and hot spots at the micro-scale. These hot spots then spread and heat cooler regions of the solid unreacted material. At the nano-scale, molecules vibrate until molecular bonds break creating a chain reaction. At the micro-scale, these reactions increase temperature and convert unreacted material to gaseous products. The hot spots then spread as chemical reaction continues heating the material to

a bulk temperature. Ultimately, the average quantities across the micros-scale would reproduce experimental shock and detonation phenomena measured at the continuum-scale. Unfortunately, the fidelity required for such an idealized model is intractable. The emerging paradigm of "multiscaling" is a useful alternative to the idealized model and is shown below on Fig. 1.6.

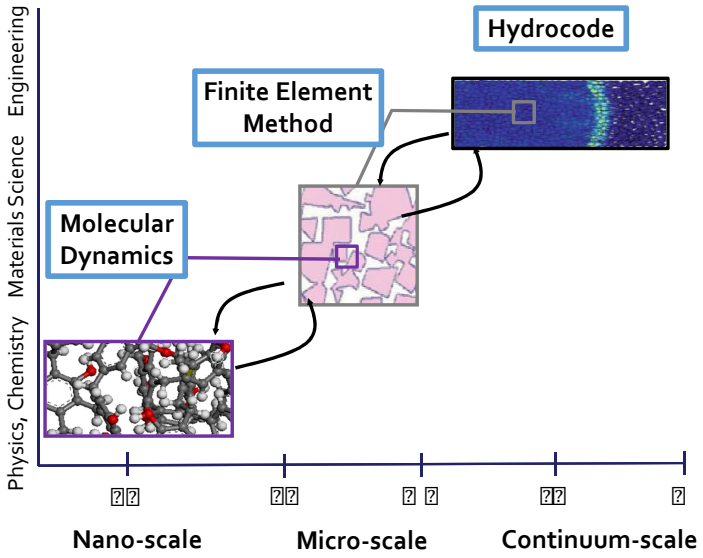

Figure 1.6: Paradigm of "multiscaling" applied to shock loading of energetic materials. Possible methods and models are shown for each length scale (continuum-, micro-, nano-)

Multiscale modeling or, coupling of simulations at various length scales, allow for the incorporation of important physical behaviors from fine to coarse length and time scales. Most existing methods are based on concurrent multiscaling, i.e. dividing the computational domain into atomistic, micro and continuum regions. For example, in quasicontinuum methods, a coarse-grained Hamiltonian is used to model the dynamics of the system [95] and a matching condition is devised for the continuum-atomistic interface. There have been several intrinsic difficulties in extending these methodologies to study dynamics and finite temperature systems. One most obvious obstacle is the issue of time scales. Even though the domain decomposition approach addresses the spatial scale issue, time scales are still coupled between the atomistic and continuum regions. Another issue is the matching conditions at the atomistic-continuum interface. Ideally the presence of the boundary should not influence the results in the atomistic region. In practice, however, it is usually too expensive to find such boundary conditions. This is especially true when the atomistic regions change in time, e.g. in order to track a moving shock. Although

multiscale modeling has been applied to the field of detonation in fluids [96], literature search reveals that a general methodology to couple simulations at different length scales (nano-micro-continuum) for shock loading in PBXs is currently lacking.

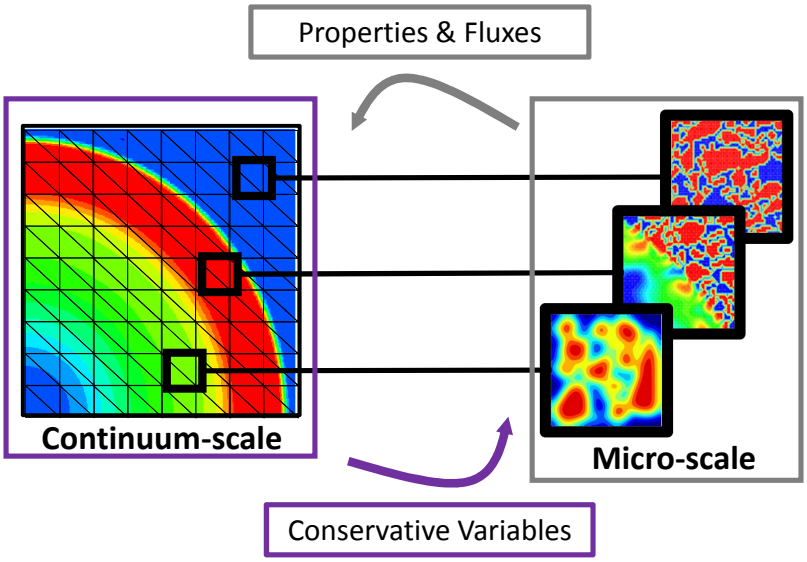

Figure 1.7: Computational Homogenization: Each numerical integration point has a varying microstructure. Information from the continuum-scale is passed to the micro-scale as conservative variables. Fluxes and properties are returned to the continuum-scale

The multiscale linking methodology considered here is called "computational homogenization" [97–101]. The approach is general and allows one to embed atomistic simulations into micro- scale simulations or micro-scale simulations into continuum-scale simulations. The idea of computational homogenization is to start with a continuum problem and find the missing information in the form of fluxes and material properties by performing local simulations of the microscale models. These microscale models are constrained to be consistent with the local continuum state of the system. A crucial component of the method is how to enforce such constraints so as to conserve energy and mass across length scales. The underlying principle is scale separation, which uses the fact that the length-scales of continuum-, micro- and nano- are vastly separated. Hence, properties at a point in the coarse-scale can be obtained from a fine-scale unit cell (with finite volume). The continuum-scale fields are passed to the micro-scale and uniformly distributed. Continuum fluxes and properties (at all integration points) are computed from the underlying microstructural sub-problem using averaging schemes. Information from the continuum is passed to the micro-scale as conservative variables and is returned as fluxes and properties as illustrated on Figure 1.7. This

approach allows for straightforward incorporation of physical and geometrical nonlinearities in material response and is based on the direct extraction of the constitutive behavior from the heterogeneity of a material. This provides significantly faster computational time than a direct numerical simulation.

Detonation models require as input the initial state of the explosive, the equations of state of the unreacted explosive and the gaseous detonation products, and the reaction rates. Currently, empirical reaction rates and equations of state are used that are tuned to a suite of macroscopic experimental data on each explosive composition. In the microstructural model, separate HMX, and binder regions are used, and each require a material model. It is necessary to represent both the unreacted material and the reaction products of all three species. This is accomplished using an equation of state for the solid unreacted material and an equation of state for the gaseous reaction products, along with a chemical reaction scheme and a mixing rule to define the properties of partially reacted states [102]. A variety of equations of state (EOS) have been used to represent explosives including Jones-Wilkins-Lee (JWL) form [46], the Murnaghan form [103] and Gruneisen form [90]. Since the primary purpose of the proposed work is to test the multiscale approach rather than focus on EOS development, a simple linear Grüneisen equation of state will be employed for the unreacted HMX and binder. The JWL form will be used to model the EOS of gaseous reaction products for both HMX and the binder. The data for the model is readily available from carefully calibrated experiments and using molecular simulations for data such as specific heat and thermal conductivity [104, 105].

Various studies have focused on the detailed reaction kinetics of HMX. Arrhenius kinetics schemes have been proposed with single-step [106] or multi-step reactions [107]. In particular a three-step scheme for HMX (depolymerization, gaseous decomposition of depolymerized HMX followed by gas phase decomposition to form the final reaction products) was proposed. A wide variety of data has been compiled for the time to explosion in HMX, including one-dimensional time-to-explosion (ODTX) and detonation data [108]. For the binders, two-step Arrhenius schemes have been proposed and fit to limited experimental data available in literature [109]. The empirical based Ignition and Growth model [46] is a pressure-dependent model formulated to represent the ignition of hot spots and the growth of reaction from hot spots into the surrounding explosive. A simplified version of the Ignition and Growth model is the JWL++ model [103]. The JWL++ model uses a mixture rule for the total pressure and has found that it is equivalent to enforcing pressure equilibrium. Both Arrhenius kinetics schemes and Ignition and Growth model will be considered in this work.

1.6 Outline

The aim of this work is begin the construction of a multiscale model, for shock loading of PBXs, that incorporates material microstructure information. This thesis is divided into 6 Chapters. Chapter 2 discusses hydrocode development and includes a review of the governing equations and models used in this work. The numerical method and shock capturing scheme are described in detail. Chapter 3 presents continuum methods and validates the solution procedure with classical fluid dynamics problems. Numerical results for shock loading of PBXs are compared with experimental data. Mesh convergence studies are presented. Chapter 4 discusses the framework and numerical results for Direct Numerical Simulation (DNS). This chapter includes the development of synthetic microstructures with varying volume fractions and material models for the binary representation. Multiple loading conditions are investigated. Multiscale modeling is presented in Chapter 5. A First-Order approach is considered, where volume averages are used. This chapter compares all methods and provides further discussion of the advantages of each method. Finally, concluding remarks and future work and implications are given in Chapter 6.

1.7 Summary

This chapter presented the motivation behind the need for a multiscale model of shock loading of PBXs. It began with a review of detonation physics and the classifications of explosives. The theories behind hydrocodes and their descriptions in the Lagrangian and Eulerian frame followed. Polymer bonded explosives and their compositions were discussed at great length with experimental work indicating the importance of the microstructure in shock loading. The existing literature for the modeling of polymer bonded explosives has been reviewed and showed the need for a multiscale model. Current models for the continuum-scale, nano-scale, micro-scale, equations of state and reaction schemes needed for the multiscale model were also discussed. Finally, the outline of this thesis was presented.

CHAPTER 2

Numerical Methods

This chapter presents the numerical methods used in this work to model shock loading of polymer bonded explosives. Section 2.1 presents the governing equations and models needed for simulating shock loading of PBXs at various scales. The reactive Euler equations are presented as well as models for the equation of state, temperature and the rate of change of mass fraction for each species. A one-step second-order finite element scheme is presented in Section 2.2 where the conservation variables are discretized in time and space. The elements used in this work are also described in this section. Next, Section 2.3 describes the high-resolution scheme used for the numerical treatment of shock waves. Finally, Section 2.4 discusses the implementation into the computational environment and speed tests.

2.1 Governing Equations and Models

The evolution of the solid-state composite during detonation can be computed by solving the reactive flow problem [110]. During detonation, a broad range of physical phenomena (e.g. expansion, diffusion, chemical reaction) interact over various scales in time and space. The scales considered in this work are on the order of microseconds for time, and between $0.1cm - 10cm$ for space. These scales are necessary for modeling at the microscale and continuum levels where experimental results may be considered. Therefore, all physical phenomena are not considered in this work. The effects due to gravity, electromagnetic forces and radiation are widely neglected in explosives modeling and are neglected in this work. It is also assumed that the flow is inviscid.

The dynamics of a continuous media can be described with a set of differential equations. Continuum mechanics uses the principles of conservation of mass, momentum, and energy to establish these equations. They relate the material density ρ, velocity $\mathbf{u}$ and the specific total energy E. However, reactive media also requires a transport equation for

each species Y_j. The two fundamental descriptions of the kinematic deformation of continuous media were presented in Section 1.3. The reactive Euler equations, or conservation equations, are shown in the Eulerian (spatial) description below

$$\frac{\partial \rho}{\partial t} + \nabla \cdot (\rho \mathbf{u}) = 0 \tag{2.1}$$

$$\frac{\partial \rho \mathbf{u}}{\partial t} + \nabla \cdot (\rho \mathbf{u} \otimes \mathbf{u} + p\mathbf{I}) = 0 \tag{2.2}$$

$$\frac{\partial \rho E}{\partial t} + \nabla \cdot ((\rho E + p)\mathbf{u}) = \sum_{j=1}^{n_{species}} q_j \rho \dot{Y_j} \tag{2.3}$$

$$\frac{\partial \rho Y_j}{\partial t} + \nabla \cdot (\rho \mathbf{u} Y_j) = \rho \dot{Y_j}, \qquad \text{for } j = 1 \ldots n_{species-1} \tag{2.4}$$

where equation 2.1 relates the rate of change in density to the spatial derivatives of the velocity vector $\mathbf{u}$. Equation 2.2 relates the rate of change in momentum to the spatial derivatives of pressure, p. Equation 2.3 relates the rate of change of total energy per unit volume to the hydrodynamic work and the rate of change of mass for each chemical species $\dot{Y_j}$, where q is the heat release. A transport equation is needed for each number of j species, for a total of $n_{species}$ with $\sum Y_j = 1$ and $\sum \dot{Y_j} = 0$ leading to $n_{species-1}$ independent equations. Equation 2.4 relates the rate of change of species mass fraction to the convection of mass fraction through space and the rate of change of mass for each chemical species $\dot{Y_j}$. Models are needed for the rates of change for each species. The reactive Euler equations, equations (2.1)-(2.4), are closed with equation of state, relating the state variables of the material $(\rho, \rho\mathbf{u}, \rho E, \rho Y_j)$ to the pressure, p and temperature, T. Pressure and temperature are functions of specific volume ν and specific internal energy e and are related to the conservation variables by

$$\nu = 1/\rho, \tag{2.5}$$

$$E = e + \frac{1}{2} \parallel \mathbf{u} \parallel^2 \tag{2.6}$$

In reactive flow, it is necessary to represent the material response of both the unreacted material and the reaction detonation products as described in Section 1.3, figure 1.4; therefore, equations of state are needed for both extremes. The pressure for a solid unreacted material is given by a linear Mie-Grüneisen equation of state [90] of the form:

$$p_s(\nu_s, e_s) = \frac{a^2(\nu_0 - \nu_s)}{(\nu_0 - b(\nu_0 - \nu_s))^2} + \frac{\gamma(\nu_s)}{\nu_s}\left(e_s - \frac{a^2(\nu_0 - \nu_s)^2}{2(\nu_0 - b(\nu_0 - \nu_s))^2}\right) \tag{2.7}$$

where the subscript "s" denotes the solid unreacted material and γ denotes the Grüneisen

parameter. The linear relationship between shock speed U_s and particle velocity u_p, or the Hugoniot $U_s = a + bu_p$, is used as the reference curve where a and b are experimental constants. Following reference [94], when the Grüneisen parameter $\gamma \equiv \gamma_0 = 1$ and the specific heat c_v is held constant temperature is calculated analytically as

$$T_s(\nu_s, e_s) = \left(\frac{\nu_0}{\nu_s}\right)^{\gamma_0} \left(T_0 + \frac{1}{c_{v,s}} \left(\frac{\nu_s}{\nu_0}\right)^{\gamma_0} (e_s - e_i(\nu_s))\right) \tag{2.8}$$

where

$$e_i(\nu_s) = \frac{-a^2}{b^3} \left(\frac{\nu_0}{\nu_s}\right) \left(\frac{3b(\nu_0 - \nu_s)}{2\nu_0} + (3-b) ln \left(\frac{\nu_0 - b(\nu_0 - \nu_s)}{\nu_0}\right) - \left(b - \frac{3}{2}\right) \frac{b(\nu_0 - \nu_s)}{\nu_0 - b(\nu_0 - \nu_s)}\right) \tag{2.9}$$

A typical model for the reaction products is the Jones-Wilkins-Lee (JWL) form [46]. The pressure is given by

$$p_g(\nu_g, e_g) = \left(1 - \frac{w\nu_0}{R_1\nu_g}\right) Aexp\left(-R_1\frac{\nu_g}{\nu_0}\right) + \left(1 - \frac{w\nu_0}{R_2\nu_g}\right) Bexp\left(-R_2\frac{\nu_g}{\nu_0}\right) + \frac{we_g}{\nu_g} \tag{2.10}$$

where the subscript "g" denotes the gaseous reaction products, and the Grüneisen parameter $\gamma \equiv w$. Again, following reference [94], when the Grüneisen parameter w and the specific heat c_v are held constant temperature is calculated analytically as

$$T_g(\nu_g, e_g) = \left(\frac{\nu_{CJ}}{\nu_g}\right)^{w} \left(T_{CJ} + \frac{1}{c_{v,CJ}} \left(\frac{\nu_g}{\nu_{CJ}}\right)^{w} (e_g - e_i(\nu_g))\right) \tag{2.11}$$

where

$$e_i(\nu_g) = \frac{\nu_0}{R_1} Aexp\left[-R_1\frac{\nu_g}{\nu_0}\right] + \frac{\nu_0}{R_2} Bexp\left[-R_2\frac{\nu_g}{\nu_0}\right] + \frac{C\nu_0}{w}\left(\frac{\nu_0}{\nu_g}\right)^{w} \tag{2.12}$$

The constants for the solid equations of state (a, b, ν_0, c_v) and gaseous equations of state $(A, B, C, \nu_{CJ}, w, c_v)$ are determined experimentally and are taken from references [47, 48, 94]. The following chapters specify each constant for each material.

Although material states are calculated for two extremes(unreacted/fully reacted) using equations (2.7)-(2.12), according to ZND theory, described in Section 1.3, there exists a finite reaction zone where the explosive is partially reacted. This state of the explosive

is determined by the burn fraction. The mass fraction of detonation products, or burn fraction, is described as λ and is a subset of Y_j. As an example, for a one-step reaction Y_1 would describe the mass fraction for unreacted PBX and Y_2 would describe the mass fraction of gaseous products. Since mass is conserved (equation 2.4), $Y_1 + Y_2 = 1$ and $\lambda = Y_2 = 1 - Y_1$. The burn fraction describes the state of the material: fully reacted material is given by $\lambda = 1$, unreacted material is given by $\lambda = 0$ and partially reacted material is given by $0 < \lambda < 1$. The pressure for a partially reacted explosive is calculated using the following mixture rule.

$$p = (1 - \lambda)p_s + \lambda p_g \tag{2.13}$$

For temperature, typically equilibrium is enforced and the following energy mixture is used.

$$e = (1 - \lambda)e_s + \lambda e_g \tag{2.14}$$

However, $e = c_p T$. By assuming a constant specific heat and considering the previous relation, the following equation is obtained; a mixture rule for temperature. Partially reacted temperature is calculated with Equation (2.15). The conventional equilibrium approach and mixture rules are compared in Appendix D.

$$T = (1 - \lambda)T_s + \lambda T_g \tag{2.15}$$

According to the mixture rule shown on equation (2.13), when $\lambda = 0$, the total pressure is equivalent to the pressure of a solid (equation (2.7)). When λ increases, the total pressure is a combination of the solid p_s, and gaseous p_g, equations of state. As λ increases and approaches unity, the total pressure is equivalent to the fully reacted equation of state (equation (2.10)). The total temperature follows the same mixing rule as shown on equation (2.15).

The transport equation (2.4) for mass fraction, and consequently the burn fraction λ, is governed by the source term modeling the reaction rate $\dot{Y_j}$. In this work it is assumed that a one-step reaction occurs for each material, including HMX, binder and homogenized PBX; i.e. the reaction scheme for each material is described by A $\xrightarrow{1}$ B, where Y_A is the mass fraction of the unreacted explosive and Y_B is the mass fraction of the gaseous reaction products(Note, $\lambda = Y_B = 1 - Y_A$). Two different models are considered in this work. The first is the Ignition and Growth model [46]. This model is empirical and based on total pressure.

$$\dot{Y_B} = I(1 - Y_B)^{\tau_1} V^{\tau_2} + G(1 - Y_B)^{\tau_1} Y_B^{\tau_3} p^{\tau_4} \tag{2.16}$$

here, I is the ignition parameter, G is the growth parameter and the parameters τ's are empirical constants. The relative volume $V = \rho/\rho_0$ where ρ_0 is the reference density. Similar to the mixture rules described in equations (2.13) and (2.15), the rate is bound by two extremes; for a solid unreacted material $\lambda = 0$ and for the completely reacted products $\lambda = 1$. At these two extremes the reaction rate for the Ignition and Growth model is zero. The second reaction rate considered in this work is in the Arrhenius model.

$$\dot{Y_A} = Y_A Z e^{-E_1/RT} \tag{2.17}$$

where q is the heat release, Z is the static frequency factor, E_1 is the activation energy and R is the molar gas constant. Detailed reaction kinetics like these are complex, however these reaction schemes have the considerable advantage of being based on appropriate chemistry. Parameter for moth the Ignition and Growth model and the Arrhenius model are provided in the following chapters.

2.2 Taylor-Galerkin Scheme

Shock wave propagation through reactive materials is simulated by solving the reactive Euler equations (2.1)-(2.4), a nonlinear set of hyperbolic conservation laws. Classical formulations of solid dynamics based on displacement approach are unsuitable for this problem due to locking issues at extreme mesh distortions and numerical errors in the velocity of propagation of waves. This problem has been largely addressed in the fluid dynamics community using Riemann solvers in the context of finite volume methods [91]. In the context of standard finite element methods, various stabilized methods such as Petrov Galerkin (PG) methods, Galerkin/least-squares (GLS) methods and the Taylor–Galerkin (TG) methods have been developed to address the issue. In the PG and GLS methods, a stabilization term with a coefficient is added to the weak form to act as an artificial diffusion, however, the choice of the coefficient is semi-empirical [111, 112]. The basic TG algorithm was proposed by Donea [113], Baker et al. [114] and Löhner et al. [115] for first-order systems of hyperbolic equations in which Taylor expansion in time precedes the Galerkin space discretization. TG finite element schemes are especially attractive since the diffusion arises from an improved Taylor approximation to the time derivative of the fields. When compared to the PG methods, TG methods were found to be approximately three times faster [116]. TG algorithms have been successfully applied in areas such as pollutant transport [117], shallow water computations [118] and high speed compressible flows [119]. Recently they have been applied to detonation of energetic particles [120–122]. The reac-

tive Euler equations are solved numerically using the TG scheme.

Consider a the domain $\Omega \subset \mathbb{R}^{n_{sd}}$ with piecewise smooth boundary Γ. Here, $n_{sd} = 1, 2$ or 3 denotes the number of space dimensions. In vector form and in 3D ($n_{sd} = 3$) the Euler equations (2.1)-(2.4) can be rewritten as

$$\frac{\partial \mathbf{U}}{\partial t} + \frac{\partial \mathbf{F_1}}{\partial x_1} + \frac{\partial \mathbf{F_2}}{\partial x_2} + \frac{\partial \mathbf{F_3}}{\partial x_3} = \mathbf{S} \tag{2.18}$$

where $\mathbf{U}$ is the vector of conservation variables, $\mathbf{F_i}$ are the associated flux vectors for each spatial dimension and $\mathbf{S}$ is the source term. They are defined as follows

$$\mathbf{U} = \begin{bmatrix} \rho \\ \rho \mathbf{u} \\ \rho E \\ \rho Y_j \end{bmatrix}, \quad \mathbf{F_i} = \begin{bmatrix} \rho u_i \\ \rho \mathbf{u} u_i + p \\ (\rho E + p) u_i \\ \rho u Y_j \end{bmatrix}, \quad i = 1, \ldots, n_{sd}, \quad \mathbf{S} = \begin{bmatrix} 0 \\ 0 \\ q_j \rho \dot{Y_j} \\ \rho \dot{Y_j} \end{bmatrix} \tag{2.19}$$

The velocity vector $\mathbf{u}$ contains components $\mathbf{u} = [u, v, w]$ and the position vector $\mathbf{x}$ contains components $\mathbf{x} = [x_1, x_2, x_3]$. Equation (2.19) can be compacted further using the divergence of the flux vector

$$\mathbf{F} = \begin{bmatrix} \mathbf{F_1} & \mathbf{F_2} & \mathbf{F_3} \end{bmatrix} \tag{2.20}$$

and the conservation equations, boundary conditions and initial conditions induce the strong form of the problem, where $\mathbf{n}$ is the normal and t is time

$$\mathbf{U}_t + \nabla \cdot \mathbf{F} = \mathbf{S} \qquad in\ \Omega \times]0, T[, \tag{2.21a}$$

$$\mathbf{F^{in}} \cdot \mathbf{n} = \mathbf{G} \qquad on\ \Gamma \times]0, T[, \tag{2.21b}$$

$$\mathbf{U}(\mathbf{x}, 0) = \mathbf{U}_0(\mathbf{x}) \qquad on\ \Omega\ at\ t = 0 \tag{2.21c}$$

Further, the Euler equations can be expressed in a quasi-linear form where flux components are written as

$$\mathbf{F_i}(\mathbf{U}) = \mathbf{A_i}(\mathbf{U})\mathbf{U} \tag{2.22}$$

where $\mathbf{A_i}(\mathbf{U}) = \partial \mathbf{F_i} / \partial \mathbf{U}$, with $i = 1, \ldots, n_{sd}$ are the Jacobian matrices and are divergence free. Thus, from equation (2.18), the quasi-linear form of the Euler equations is given by

$$\frac{\partial \mathbf{U}}{\partial t} + \mathbf{A_1} \frac{\partial \mathbf{U}}{\partial x_1} + \mathbf{A_2} \frac{\partial \mathbf{U}}{\partial x_2} + \mathbf{A_3} \frac{\partial \mathbf{U}}{\partial x_3} = \mathbf{S} \tag{2.23}$$

or in compact form

$$\mathbf{U}_t + (\mathbf{A} \cdot \nabla)\mathbf{U} = \mathbf{S}. \tag{2.24}$$

The TG algorithm for the Euler equations begins with a truncated Taylor expansion in time about the conservation variables followed by the Galerkin space discretization. For the next time step $n+1$ the Taylor expansion is

$$\mathbf{U}^{n+1} = \mathbf{U}^n + \Delta t\ \mathbf{U}_t^n + \frac{1}{2}\Delta t^2\, \mathbf{U}_{tt}^n + \mathcal{O}(\Delta t^3) \tag{2.25}$$

where $(\cdot)_t$ denotes the partial derivative in time and Δt denotes the time increment. The time derivatives are replaced by spatial derivatives using the quasi-linear form and equation (2.21). The first derivative is found by rearranging equation (2.21a)

$$\mathbf{U}_t = -\nabla \cdot \mathbf{F} + \mathbf{S}. \tag{2.26}$$

The second derivative is found by differentiating the first derivative, found in equation (2.26), in time

$$(\mathbf{U}_t)_t = \mathbf{U}_{tt} = (-\nabla \cdot \mathbf{F} + \mathbf{S})_t = -\nabla \cdot \mathbf{F}_t + \mathbf{S}_t = -\nabla \cdot \left(\frac{\partial \mathbf{F}}{\partial t}\right) + \frac{\partial \mathbf{S}}{\partial t}. \tag{2.27}$$

producing, $\mathbf{S}_t$ the rate of the source term. It is approximated by finite differences on the known source vector $\mathbf{S}$; i.e. $\mathbf{S}_t = (\mathbf{S}^n - \mathbf{S}^{n-1})/\Delta t$. Applying the chain rule to the second term of the R.H.S. and using $\mathbf{A_i}(\mathbf{U}) = \partial \mathbf{F_i}/\partial \mathbf{U}$ from equation (2.24) the equation above becomes

$$\mathbf{U}_{tt} = -\nabla \cdot \left(\frac{\partial \mathbf{F}}{\partial \mathbf{U}}\frac{\partial \mathbf{U}}{\partial t}\right) + \frac{\partial \mathbf{S}}{\partial t} = -\nabla \cdot \left(\mathbf{A}\frac{\partial \mathbf{U}}{\partial t}\right) + \frac{\partial \mathbf{S}}{\partial t}. \tag{2.28}$$

but the first derivative of time is known from equation (2.26); therefore the second derivative is

$$\mathbf{U}_{tt} = -\nabla \cdot (\mathbf{A}\mathbf{U}_t) + \mathbf{S}_t = \nabla \cdot (\mathbf{A}(\nabla \cdot \mathbf{F} - \mathbf{S})) + \mathbf{S}_t. \tag{2.29}$$

The resulting second-order accurate explicit time-stepping method results from combining equations (2.25), (2.26) and (2.29).

$$\mathbf{U}^{n+1} = \mathbf{U}^n + \Delta t\ (-\nabla \cdot \mathbf{F}^n + \mathbf{S}^n) + \frac{1}{2}\Delta t^2\, (\nabla \cdot (\mathbf{A}^n(\nabla \cdot \mathbf{F}^n - \mathbf{S}^n)) + \mathbf{S}_t^n) \tag{2.30}$$

rearranging and using equation(2.22) the final strong form is obtained

$$\frac{\mathbf{U}^{n+1} - \mathbf{U}^n}{\Delta t} = -\nabla \cdot \mathbf{F}^n + \mathbf{S}^n + \frac{1}{2}\Delta t\, \nabla \cdot (\mathbf{A}^n\, \mathbf{A}^n \cdot \nabla \mathbf{U}^n - \mathbf{A}^n\, \mathbf{S}^n) + \frac{1}{2}\Delta t\, \mathbf{S}_t^n \tag{2.31}$$

Now that the governing equation is discretized in time, Galerkin space discretization follows. The weak form is obtained with a weighted residual formulation. The test functions, $\widetilde{\mathbf{U}}$, do not vary in time and belong to $\boldsymbol{\mathcal{V}} := \boldsymbol{\mathcal{H}}^{\mathbf{1}}(\boldsymbol{\Omega})$, a space of vector functions. The space trial functions, $\mathbb{S}_{\mathbf{t}}$ varies as a function of time t

$$\mathbb{S}_{\mathbf{t}} := \{\mathbf{U} \mid \mathbf{U}(\cdot, t) \in \boldsymbol{\mathcal{H}}^{\mathbf{1}}(\boldsymbol{\Omega}), t \in [0, T]\}\,. \tag{2.32}$$

The strong form in equation (2.31) is multiplied by the test functions $\widetilde{\mathbf{U}}$ containing $\widetilde{\rho}$, $\widetilde{\rho u_i}$ $\widetilde{\rho E}$, and $\widetilde{\rho Y}_j$, and integrated over space

$$\begin{aligned}\int_\Omega \widetilde{\boldsymbol{U}}^{\boldsymbol{T}} \frac{\mathbf{U}^{n+1} - \mathbf{U}^n}{\Delta t}\, d\boldsymbol{\Omega} = &- \int_\Omega \widetilde{\boldsymbol{U}}^{\boldsymbol{T}} \nabla \cdot \mathbf{F}^n\, d\boldsymbol{\Omega} + \int_\Omega \widetilde{\boldsymbol{U}}^{\boldsymbol{T}}\, \mathbf{S}^n\, d\boldsymbol{\Omega} \\ &+ \frac{1}{2}\Delta t \int_\Omega \widetilde{\boldsymbol{U}}^{\boldsymbol{T}}\, \nabla \cdot \left(\mathbf{A}^n \mathbf{A}^n\, \nabla \cdot \mathbf{U}^n - \mathbf{A}^n\, \mathbf{S}^n\right)\, d\boldsymbol{\Omega} + \frac{1}{2}\Delta t \int_\Omega \widetilde{\boldsymbol{U}}^{\boldsymbol{T}}\, \mathbf{S}_t^n\, d\boldsymbol{\Omega}\end{aligned} \tag{2.33}$$

The divergence theorem is used to weaken the smoothness requirement of the trial solution and produces

$$\begin{aligned}\int_\Omega \widetilde{\boldsymbol{U}}^{\boldsymbol{T}} \frac{\mathbf{U}^{n+1} - \mathbf{U}^n}{\Delta t}\, d\boldsymbol{\Omega} = &\int_\Omega \nabla\widetilde{\boldsymbol{U}}^{\boldsymbol{T}} \mathbf{F}^n\, d\boldsymbol{\Omega} - \int_\Gamma \widetilde{\boldsymbol{U}}^{\boldsymbol{T}} \mathbf{n} \cdot \mathbf{F}^n\, d\boldsymbol{\Gamma} + \int_\Omega \widetilde{\boldsymbol{U}}^{\boldsymbol{T}}\, \mathbf{S}^n\, d\boldsymbol{\Omega} \\ &- \frac{1}{2}\Delta t \int_\Omega \nabla\widetilde{\boldsymbol{U}}^{\boldsymbol{T}}\, \left(\mathbf{A}^n \mathbf{A}^n\, \nabla \cdot \mathbf{U}^n - \mathbf{A}^n\, \mathbf{S}^n\right)\, d\boldsymbol{\Omega} \\ &+ \frac{1}{2}\Delta t \int_\Gamma \widetilde{\boldsymbol{U}}^{\boldsymbol{T}}\, \left(\mathbf{A}^n \mathbf{A}^n\, \nabla \cdot \mathbf{U}^n - \mathbf{A}^n\, \mathbf{S}^n\right)\, \mathbf{n}\, d\boldsymbol{\Gamma} + \frac{1}{2}\Delta t \int_\Omega \widetilde{\boldsymbol{U}}^{\boldsymbol{T}}\, \mathbf{S}_t^n\, d\boldsymbol{\Omega}\end{aligned} \tag{2.34}$$

containing boundary terms along $\boldsymbol{\Gamma}$. Using equation (2.21b) and rearranging terms results in the final problem statement: for $t \in]0, T[$, find $\mathbf{U}(\mathbf{x}, t) \in \mathbb{S}_{\mathbf{t}}$ such that $\mathbf{U}(\mathbf{x}, 0) = \mathbf{U}_0(\mathbf{x})$ and

$$\begin{aligned}\int_\Omega \widetilde{\boldsymbol{U}}^{\boldsymbol{T}} \frac{\mathbf{U}^{n+1} - \mathbf{U}^n}{\Delta t}\, d\boldsymbol{\Omega} = &\int_\Omega \nabla\widetilde{\boldsymbol{U}}^{\boldsymbol{T}} \mathbf{F}^n\, d\boldsymbol{\Omega} + \int_\Omega \widetilde{\boldsymbol{U}}^{\boldsymbol{T}}\, \mathbf{S}^n\, d\boldsymbol{\Omega} + \frac{1}{2}\Delta t \int_\Omega \widetilde{\boldsymbol{U}}^{\boldsymbol{T}}\, \mathbf{S}_t^n\, d\boldsymbol{\Omega} \\ &+ \frac{1}{2}\Delta t \int_\Omega \nabla\widetilde{\boldsymbol{U}}^{\boldsymbol{T}} \mathbf{A}^n\, \mathbf{S}^n\, d\boldsymbol{\Omega} - \frac{1}{2}\Delta t \int_\Omega \nabla\widetilde{\boldsymbol{U}}^{\boldsymbol{T}} \mathbf{A}^n \mathbf{A}^n\, \nabla \cdot \mathbf{U}^n\, d\boldsymbol{\Omega} \\ &- \int_\Gamma \widetilde{\boldsymbol{U}}^{\boldsymbol{T}} \left(\mathbf{F}^n + \frac{1}{2}\Delta t\, \left(\mathbf{A}^n\, \mathbf{S}^n - \mathbf{A}^n \mathbf{A}^n\, \nabla \cdot \mathbf{U}^n\right)\right)\, \mathbf{n}\, d\boldsymbol{\Gamma}\end{aligned} \tag{2.35}$$

for all test functions $\widetilde{\boldsymbol{U}} \in \boldsymbol{\mathcal{V}}$. Furthermore, approximating $\mathbf{F}^{n+1} = \mathbf{F}^n + \Delta t/2\ \mathbf{F}_t^n$, the

boundary term is modified and the final weak form is obtained.

$$\int_\Omega \widetilde{\boldsymbol{U}}^{\boldsymbol{T}} \frac{\mathbf{U}^{n+1}-\mathbf{U}^n}{\Delta t}\, d\boldsymbol{\Omega} = \int_\Omega \nabla\widetilde{\boldsymbol{U}}^{\boldsymbol{T}}\mathbf{F}^n\, d\boldsymbol{\Omega} + \int_\Omega \widetilde{\boldsymbol{U}}^{\boldsymbol{T}}\,\mathbf{S}^n\, d\boldsymbol{\Omega} + \frac{1}{2}\Delta t \int_\Omega \widetilde{\boldsymbol{U}}^{\boldsymbol{T}}\,\mathbf{S}_t^n\, d\boldsymbol{\Omega} + \frac{1}{2}\Delta t \int_\Omega \nabla\widetilde{\boldsymbol{U}}^{\boldsymbol{T}}\mathbf{A}^n\,\mathbf{S}^n\, d\boldsymbol{\Omega} - \frac{1}{2}\Delta t \int_\Omega \nabla\widetilde{\boldsymbol{U}}^{\boldsymbol{T}}\mathbf{A}^n\mathbf{A}^n\nabla\cdot\mathbf{U}^n\, d\boldsymbol{\Omega} - \int_\Gamma \widetilde{\boldsymbol{U}}^{\boldsymbol{T}}\left(\mathbf{F}^n + \frac{1}{2}\Delta t\,(\mathbf{F}_t^n)\right)\mathbf{n}\, d\boldsymbol{\Gamma} \quad (2.36)$$

The conservation variables in vector **U** are approximated spatially within an element using standard finite element shape functions $N_\alpha(\mathbf{x})$ where $\alpha = 1, 2, \ldots nne$ is the node number and i is the direction.

$$\rho(\mathbf{x}) = N_\alpha(\mathbf{x})(\rho)_\alpha \quad (2.37a)$$

$$\rho u_i(\mathbf{x}) = N_\alpha(\mathbf{x})(\rho u_i)_\alpha \quad (2.37b)$$

$$\rho E(\mathbf{x}) = N_\alpha(\mathbf{x})(\rho E)_\alpha \quad (2.37c)$$

$$\rho Y_j(\mathbf{x}) = N_\alpha(\mathbf{x})(\rho Y_j)_\alpha \quad (2.37d)$$

producing the elemental conservation vector $\mathbf{U}_k = N_{km}U_m$ where the matrix of shape function N_{km} contains N_α's with $k = 1, 2, \ldots dof$(degrees of freedom) and $m = 1, 2, \ldots dof*$ nne (degrees of freedom by number of nodes per element); i.e.

$$N_{km} = \quad (2.38)$$

$$\begin{array}{c} \\ k=1, \\ 2, \\ \vdots \\ dof \end{array} \begin{array}{c} \begin{array}{cccccccccc} m=1, & 2, & \cdots & nne & \cdots & (dof-1)nne & \cdots & & dof*nne \end{array} \\ \begin{bmatrix} N_1 & 0 & \cdots & 0 & & N_{nne} & 0 & \cdots & 0 \\ 0 & N_1 & & & \bullet\bullet\bullet & 0 & N_{nne} & & \\ \vdots & & \ddots & & & \vdots & & \ddots & \\ 0 & & & N_1 & & 0 & & & N_{nne} \end{bmatrix} \end{array}$$

Similarly, the test functions inside $\widetilde{\boldsymbol{U}}$ can be interpolated locally using the same shape functions. The elemental test function vector $\widetilde{\boldsymbol{U}}_k = N_{km}\widetilde{U}_m$. Here, $\widetilde{U}_m$ contains the virtual

functions $(\widetilde{\rho})_\alpha$, $(\widetilde{\rho u_i})_\alpha(\widetilde{\rho E})_\alpha$, and $(\widetilde{\rho Y_j})_\alpha$; therefore, $\widetilde{\boldsymbol{U}}_k$ is

$$\widetilde{\rho}(\mathbf{x}) = N_\alpha(\mathbf{x})(\widetilde{\rho})_\alpha \tag{2.39a}$$

$$\widetilde{\rho u}_i(\mathbf{x}) = N_\alpha(\mathbf{x})(\widetilde{\rho u}_i)_\alpha \tag{2.39b}$$

$$\widetilde{\rho E}(\mathbf{x}) = N_\alpha(\mathbf{x})(\widetilde{\rho E})_\alpha \tag{2.39c}$$

$$\widetilde{\rho Y}_j(\mathbf{x}) = N_\alpha(\mathbf{x})(\widetilde{\rho Y_j})_\alpha \tag{2.39d}$$

The gradients of all functions are evaluated by differentiating the interpolation functions. For example the displacement vector can also be interpolated as $\widetilde{x}_i(\mathbf{x}) = N_\alpha(\mathbf{x})(\widetilde{x}_i)_\alpha$; therefore

$$\frac{\partial \widetilde{x}_i}{\partial x_j} = \frac{\partial N_\alpha(\mathbf{x})}{\partial x_j}(\widetilde{x}_i)_\alpha \tag{2.40}$$

An issue with finite element discretization of nonlinear hyperbolic problem is the choice of the local approximation for the nonlinear flux function $\mathbf{F}$. Two options are presented here, the first being the classical representation. The flux is determined by fist evaluating the conservative vector $\mathbf{U}_k$ at the desired point within the element and then evaluating the flux.

$$\mathbf{F}_k(\mathbf{U}) = F_k(\mathbf{U}_k) = F_k(N_{km}U_m) \tag{2.41}$$

The other approximation considered is the group representation.

$$\mathbf{F}_k(\mathbf{U}) = N_{km}F_m(U_m) \tag{2.42}$$

Here the flux is approximated directly with the same interpolation functions N_{km}. Group representation is advantageous as the spatial dependency of the flux function is described directly by the element shape functions. Therefore, in regions of compression where $\partial\mathbf{u}/\partial\mathbf{x} < 0$, flux is computed based on a group representation. The weak form equation (2.35) is formulated for all three spatial directions with their Jacobian's $\mathbf{A}$ in Appendices A,B and C.

As shown in equations (2.37) and (2.39) values at points inside an element need to be represented in terms of the nodal values of the element. Although all three spatial directions are considered in this work, a two-dimensional element is described as an example. Other formulations can be found in reference [123]. The general quadrilateral element commonly used in finite element hydrocodes. It has four nodes and is depicted in $x-y$ space on Figure 2.1(left).

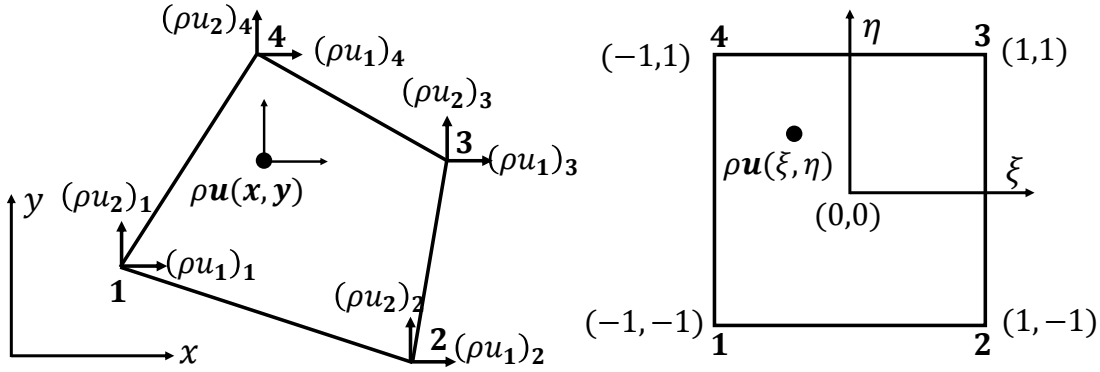

Figure 2.1: The 4-noded quadrilateral element depicted in $x-y$ space(left) and isoparametric coordinates(right) for momentum ρu_i

The local nodes, α are numbered in a clockwise fashion where $\rho u_i(x,y)$ is the momentum at point (x,y). Again, $\rho u_i(x,y)$ can be calculated from the values at the nodes using the interpolation functions; i.e.

$$\rho u_i = N_1(\rho u_i)_1 + N_2(\rho u_i)_2 + N_3(\rho u_i)_3 + N_4(\rho u_i)_4. \tag{2.43}$$

To simplify the interpolation functions N_α a pair of local curvilinear coordinates (ξ,η) known as isoparametric coordinates are introduced. These coordinates range from -1 to 1 as shown on Figure 2.1(right). Interpolation functions must be continuous within the element, sum to unity at any point within the element and the value of N_α at node β is $\delta_{\alpha,\beta}$. A set of bilinear interpolation functions satisfy these requirements and are described for the quadrilateral element in $\xi-\eta$ space as

$$N_\alpha = \frac{1}{4}(1+\xi\xi_\alpha)(1+\eta\eta_\alpha). \tag{2.44}$$

Coordinates may also be expressed using the same shape functions

$$x_i(\mathbf{x}) = N_\alpha(\mathbf{x})(x_i)_\alpha \tag{2.45}$$

Subsequently, derivatives of functions in $x-y$ space need to be expressed in $\xi-\eta$ space. Take an arbitrary function $\mathbf{f}$, that is a function of x and y and therefore a function of ξ and η through equations (2.44) and (2.45); i.e. $\mathbf{f} = \mathbf{f}(x(\xi,\eta), y(\xi,\eta))$. Using the chain rule

$$\begin{bmatrix} \partial\mathbf{f}/\partial\xi \\ \partial\mathbf{f}/\partial\eta \end{bmatrix} = \boldsymbol{J} \begin{bmatrix} \partial\mathbf{f}/\partial x \\ \partial\mathbf{f}/\partial y \end{bmatrix}. \tag{2.46}$$

where the Jacobian

$$\mathbf{J} = \begin{bmatrix} \partial x/\partial \xi & \partial y/\partial \xi \\ \partial x/\partial \eta & \partial y/\partial \eta \end{bmatrix} \tag{2.47}$$

Equation (2.46) can be inverted to transform between these two spaces. From these relationships, derivatives can be computed in both spaces and the following result is found.

$$dxdy = \mathbf{det}(\mathbf{J}) d\xi d\eta \tag{2.48}$$

where the $\mathbf{det}(\cdot)$ is the determinant of the matrix. This relation is needed when numerically integrating the weak form, equation (2.35). Consider the following integral

$$I = \int_{-1}^{1} \int_{-1}^{1} f(\xi, \eta) d\xi d\eta \tag{2.49}$$

The Gaussian quadrature approach is used for evaluating integrals in this work. The n point approximation of the integral is given as

$$I \approx \sum_{i=1}^{n} \sum_{j=1}^{n} w_i w_j f(\xi_i, \eta_j) \tag{2.50}$$

where w_i and w_j are the weights and ξ_i and η_j are the Gauss points. Equation (2.50) provides an exact answer for polynomials $f(\xi, \eta)$ when n Gauss points and n weights are selected, even if $f(\xi, \eta)$ is not a polynomial. Gauss point and weights are readily available [123] for multiple degrees on polynomials and are shown for the 2×2 quadrilateral element in Figure 2.2. The same elemental formulation is considered for the 3-noded constant strain triangle (CST) whose shape functions are given by

$$N_1 = \xi, \quad N_2 = \eta, \quad N_3 = 1 - \xi - \eta \tag{2.51}$$

The 3-dimensional interpretation of the quadrilateral element is the 8-noded brick element whose shape functions are given by

$$N_i = \frac{1}{8}(1 + \xi_i \xi)(1 + \eta_i \eta)(1 + \zeta_i \zeta) \tag{2.52}$$

where $i = 1, 2, \ldots, 8$ with ζ representing the 3rd dimension for the isoparametric coordinate system.

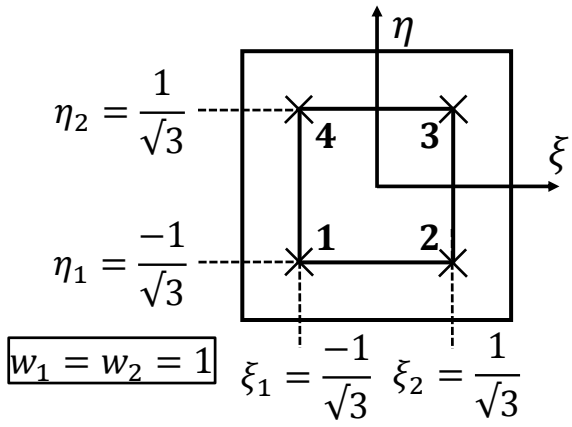

Figure 2.2: Gauss points and weights for the 2×2 quadrilateral element

2.3 Numerical Treatment of Shocks

Fluid variables are related across a shock wave through the Rankine-Hugoniot jump conditions. Although the conditions guarantee a solution for the inviscid equations, numerical computation of the shock flows with the jump conditions is prohibitive. However, the Rankine-Hugoniot jump conditions can be satisfied by numerical solutions with the introduction of an artificial viscosity term in the conservation law equations. Essentially, this term smears the discontinuity over multiple elements removing the spurious oscillations near the shock front. Great care must be taken when choosing this term; increasing the dissipation can destroy the shock front, the very mechanism needed for detonation of PBXs. Pseudo viscous pressure methods [124] are often used and produce local smoothing within the Euler equations (2.18) by the introduction of an additional pressure term. However, monotone schemes, such as these, are generally too dissipative and can spread shocks over too many grid points. Higher-order schemes have been developed and implicitly introduce the damping mechanism by choosing the appropriate form of the discrete equations through the definition of flux functions [125–127]. Limiters produce a high-order method, at least second-order accuracy, in the smooth parts of the flow and impose constraints on the flux function (flux limiters) or on the gradient of the dependent variables (slope limiters). Such schemes automatically control amount of added numerical dissipation. Note, shock capturing schemes for use in finite elements is an active area of research.

A high-resolution scheme is used for the numerical treatment of shocks in this work and follows [128]. This scheme is used for the purpose of adding minimal numerical dissipation and to give non-oscillatory solutions in the presence of steep solution gradients. Numerical dissipation is applied in the neighborhood of a discontinuity where the diffusion

coefficient is calculated based on the local behavior of the solution. After Galerkin spatial discretization, described in Section 2.2, equation (2.35) can be expressed as the algebraic equation

$$\mathbf{M}(\mathbf{U}^{n+1} - \mathbf{U}^n) = \Delta t \mathbf{B}^n \tag{2.53}$$

where **M** is the mass matrix and **B** is the force vector. The consistent mass matrix **M** acting on $\mathbf{U}^{n+1}$ is replaced by the diagonal matrix M^L, obtained by row sum. This is done to reduce the second-order scheme to first-order near the shock front. Now Eq.2.53 becomes the first-order scheme

$$\mathbf{M}^L\mathbf{U}^{n+1} = \mathbf{M}\mathbf{U}^n + \Delta t \mathbf{B}^n \tag{2.54}$$

which can be rewritten as

$$\mathbf{M}^L\mathbf{U}^{n+1} = \mathbf{M}^L\mathbf{U}^n + (\mathbf{M} - \mathbf{M}^L)\mathbf{U}^n + \Delta t \mathbf{B}^n \tag{2.55}$$

where the term $(\mathbf{M} - \mathbf{M}^L)\mathbf{U}^n$ represents added dissipation. This term is multiplied by the parameter d, where $0 \leq d \leq 1$. Now the system is written as

$$\mathbf{M}^L\mathbf{U}^{n+1} = \mathbf{M}^L\mathbf{U}^n + d(\mathbf{M} - \mathbf{M}^L)\mathbf{U}^n + \Delta t \mathbf{B}^n \tag{2.56}$$

For a $d = 1$ a first-order method is obtained for maximum dissipation. When $d = 0$ the second order scheme is recovered, equation (2.53), and no dissipation is added. This can be divided into a two stage procedure. The first stage corresponds to the second-order Taylor-Galerkin scheme and the second stage introduces dissipation.

$$\mathbf{M}(\mathbf{U}^* - \mathbf{U}^n) = \Delta t \mathbf{B}^n \tag{2.57}$$

$$\mathbf{M}^L(\mathbf{U}^{n+1} - \mathbf{U}^*) = d(\mathbf{M} - \mathbf{M}^L)\mathbf{U}^* \tag{2.58}$$

The procedure entails solving equation (2.57) initially using the Taylor-Galerkin scheme and thus obtaining $\mathbf{U}^*$, followed by solving for the new solution $\mathbf{U}^{n+1}$ using equation (2.57). Second-order phase accuracy of the method is preserved in the smooth part of the flow, while introducing dissipation around shocks. For a value of $d > 0$ the system adds dissipation to the entire system; i.e. global smoothing. Local smoothing is produced by controlling d locally, in the presence of shocks. Locally, at a node "i" the right hand side of equation (2.58) is

$$\sum_j d_{ij} M_{ij} (U_j^* - U_i^*) \tag{2.59}$$

where nodes j are connected to node i. The dissipation parameter d_{ij} is constructed by the

following equation

$$d_{ij} = min[\chi max(d_i, d_j), 1] \tag{2.60}$$

where χ is a free parameter and d_i and d_j are the local dissipation parameters at nodes i and j respectively. These local parameters activate at the presence of shocks. An effective shock sensor is constructed using pressure gradients

$$\begin{aligned} d_i &= |\frac{pj - 2pi + pi_-}{pj + 2pi + pi_-}|, \\ d_j &= |\frac{pj_+ - 2pj + pi}{pj_+ + 2pj + pi}| \end{aligned} \tag{2.61}$$

where

$$\begin{aligned} pi_- &= pj - 2(xj - xi) \cdot [\nabla p]i, \\ pj_+ &= pi - 2(xj - xi) \cdot [\nabla p]j. \end{aligned} \tag{2.62}$$

The effects of the adjustable free parameter χ and the smoothing parameter d will are studied in the following Chapter.

2.4 Computational Implementation

The computational implementation of the explicit, one-step, second-order Taylor-Galerkin scheme developed in Section 2.2 was developed in-house using resources at the University of Michigan Center for Advanced Computing (CAC). The numerical scheme was written in the object-oriented programming language C++, which is often used for high performance computing(HPC) code development within scientific computing community [129] due to its performance qualities. To aid in speeding up the solution process, the assembly process and solution scheme are parallelized. The solution requires sparse matrix inversion as seen in (2.57). The hydrocode was developed using the parallel toolbox PETSc [130] and the solution of linear systems is accomplished using a GMRES solver along with block Jacobi and ILU preconditioning. The University of Michigan CAC's Flux cluster(27,000 cores-4 GB of RAM per core) was utilized for fast numerical implementation. The overall solution procedure is shown in the following Algorithm 2.4.

To test the computational performance of the solution process, scalability tests were performed. In general these tests examine the capability of solution process to an increase in data load or in resources. The solution procedure was ran for a $0.5cm \times 0.5cm$ sample for a total of 10 time steps, Δt with results shown on Figure 2.3. Strong scaling, defined

by how the solution time varies with the number of processes for a fixed total problem size was preformed for various problem sizes. The strong scaling efficiency (as a percentage of linear) is given as by

$$100\left(\frac{t_1}{N\ t_N}\right) \tag{2.63}$$

where t_1 is the amount of time to complete a work unit with 1 process and t_N is the amount of time to complete the same unit of work with N processes. As expected, scaling efficiency decreases as the number of processes increases due to communication overhead; however, total computational time decreases. Increasing fidelity, or number of elements per centimeter, provides a higher scaling efficiency when the number of processes increases.

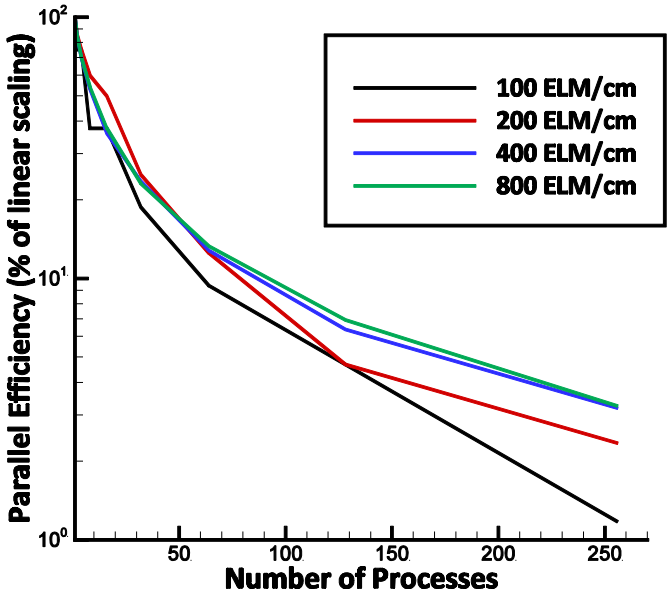

Figure 2.3: The strong scaling efficiency (as a percentage of linear) versus number of processes for a $0.5cm \times 0.5cm$ sample for a total of 10 time steps, Δt

2.5 Summary

This chapter presented the numerical methods and models needed to simulate shock loading of PBXs. It began with the presentation of the governing Euler equations followed by the presentation of various equations of state. Models for reaction rates based on temperature and pressure were presented. Next, the explicit, one-step, second-order Taylor-Galerkin scheme developed resulting in the variational form of the governing equations. The finite element method was discussed with the development of the quadrilateral element and its associated numerical integration scheme. A high-resolution scheme was presented for the

purpose of adding minimal numerical dissipation in the presence of steep solution gradients. Finally, the computational implementation of the solution procedure was discussed along with the scaling efficiency.

input : $\mathbf{U}^n$
output : $\mathbf{U}^{n+1}$
initialize : $\mathbf{U}(0, \mathbf{x}), t, \mathbf{x}, \Delta x, \Delta t$

for $i := \Delta t; \quad + + \Delta t; \quad$ **to** t **do**
  for $j := 1; \quad + + 1; \quad$ **to** *Number of elements* **do**
    for $k := 1; \quad + + 1; \quad$ **to** *Number of integration points* **do**
      `calculate(`$\boldsymbol{U}^n$`)` $\Rightarrow$ Eq. (2.37);
      `calculate(`$\boldsymbol{F}$`)`;
      if $\partial \boldsymbol{u} / \partial \boldsymbol{x} < 0$ **then**
        $\mathbf{F} :=$ group representation $\Rightarrow$ Eq. (2.42);
      else
        $\mathbf{F} :=$ classical representation $\Rightarrow$ Eq. (2.41);
      `calculate(`$P\&T$`)`;
      if $\lambda = 0$ **then**
        $P = P_s \Rightarrow$ Eq. (2.7);
        $T = T_s \Rightarrow$ Eq. (2.8) - (2.9);
      else if $\lambda = 1$ **then**
        $P = P_g \Rightarrow$ Eq. (2.10);
        $T = T_g \Rightarrow$ Eq. (2.11) - (2.12);
      else
        Mixture Rule $\Rightarrow$ Eq. (2.13) - (2.15);
      `calculate(`$\boldsymbol{S}$`)` $\Rightarrow$ Eq. (2.16) or (2.17);
      `calculate(`$\boldsymbol{S}_t = (\boldsymbol{S}^n - \boldsymbol{S}^{n-1})/\Delta t$`)`;
      `calculate(`$\boldsymbol{A}$`)` $\Rightarrow$ App. A - C;
      `calculate(`*Local Mass Matrix & Force Vector*`)` $\Rightarrow$ Eq. (2.35);
    $\circledast$*Assemble* $\boldsymbol{M}$ *and* $\boldsymbol{B}$;
  Apply boundary conditions;
  $\circledast$*Invert* $\boldsymbol{M}$ *and* `calculate(`$\boldsymbol{U}^*$`)` $\Rightarrow$ *Eq.* (2.57);
  `calculate(`$\circledast$*Smoothing Parameter* d`)` $\Rightarrow$ Eq. (2.60);
  `calculate(`$\boldsymbol{U}^{n+1}$`)` $\Rightarrow$ Eq. (2.58);
  Update Values & Print Data;
$\circledast$ *Parallelized process*;

Figure 2.4: Numerical solution procedure

CHAPTER 3

Continuum Methods

This chapter presents the continuum methods used to simulate shock loading of polymer bonded explosives. These methods do not explicitly model material heterogeneities and treat PBXs as homogenized materials which is a conventional approach used within hydrocodes. Numerical results using the Taylor-Galerkin Scheme described in Chapter 2 are presented for, ideal gases, homogenized PBXs, and individual species of HMX and polymeric binder. Section 3.1 compares numerical results with analytically obtained solutions for classical fluid dynamics problems and the effects of the free smoothing parameters discussed in Section 2.3. Model validation of PBXs is presented in Section 3.2. First, Section 3.2.1 presents the Hugoniot for each material considered in this work. The linear shock relations are calculated and compare to experimental curves. Section 3.2.2 presents the run-to-detonation data and their corresponding Pop-plots. Section 3.2.3 measures the effect of mesh density on known shock values for differing reaction models and materials. Finally, Section 3.2.4 presents 2D experiments for shock loading.

3.1 Model Validation: Test Problems

To test the stability and accuracy of Taylor-Galerkin Scheme described in Chapter 2, the classical fluid dynamics Sod's Shock Tube problem is solved. The test consists of two ideal fluids at differing pressures separated by a membrane at time $t = 0$. The flow is non-reactive and thus equation (2.4) is neglected and the hydrodynamics equations, that is, the equations for the conservation of mass (2.1), momentum (2.2) and energy (2.3) are solved. No chemical reaction occurs and therefore, the source terms $\mathbf{S}$, or the right hand side of hydrodynamics equations are zero. At $t > 0$ the membrane is removed and a rarefaction wave, contact discontinuity and shock wave is formed. The analytical solution is obtained using Riemann invariants [131]. The numerical solution is obtained using the 1D T-G scheme with no damping (i.e. $d = 0$ or $\chi = 0$)to study the effect of the smoothing

parameters discussed in Section 2.3. The analytical solution for density, velocity, pressure, speed of sound, enthalpy and entropy at $t = 0.15$ is compared with numerical results on Figure 3.1. Numerical results were obtained with linear 2-noded elements using a mesh size of $\Delta x = 0.01$ and a time step of $\Delta t = 0.001$ for a domain of length $L = 1$. The numerical results on Figures 3.1 show good agreement with the exact solution and the distinct characteristics of the test are captured. However, near the shock wave fronts, at which abrupt changes in the fluid properties occur, spurious oscillations are observed showing the need for an artificial viscosity term. Great care must be taken when choosing this term; increasing dissipation can destroy the shock front, the very mechanism needed for detonation of PBXs. The high resolution scheme, described in Section 2.3, is introduced to the test problem. Essentially, this scheme smears the discontinuity over multiple elements, smoothing the solution. The dissipation is controlled globally or locally with a free parameter. The effects of the global free parameter d on the numerical solution are studied on Figure 3.2(a). For a value of $d > 0$ the system adds dissipation to the entire system; i.e. global smoothing. When $d = 0$ there is no smoothing and the results from Figures 3.1 is obtained. Figure 3.2(a) shows the average error per node as a function of the parameter for varying time steps and mesh sizes. In general, error increases with increasing the parameter and decreasing the time step increases the average error per node. The value near $d = 0.005$ produces the minimum average error per node for each case. Similarly, the effects of the local free parameter χ on the numerical solution are studied on Figure 3.2(b). For the local scheme, d is controlled locally using Equation (2.60), pressure gradients for shock sensing and the free parameter χ. When $\chi = 0$ there is no smoothing and the results from Figures 3.1 is obtained. Figure 3.2(b) follows a similar trend to that produced by the global smoothing study and produces the minimum average error per node near $\chi = 0.2$. This value is used for the numerical results in the following studies and in subsequent sections. Figure 3.3 shows the analytical solution for density, velocity, pressure, speed of sound, enthalpy and entropy at $t = 0.15$ compared to the numerical results using $\chi = 0.2$. Again, the numerical results show good agreement with the exact solution and the distinct characteristics of the test are captured with the spurious oscillations dissipated.

Next, to verify that the numerical scheme described above is accurate for reactive flow, a simple detonation model is tested. This model is based on ZND theory described in Section 1.2, which accounts for the finite time required for chemical reaction to occur. It assumes that as the detonation wave shocks the unreacted material, chemical reaction begins to occur transforming the solid material into gaseous reaction products. Chemical reaction is governed by Arrhenius' law, producing exponentially small reactions near the von Neumann temperature. Here, $n_{sd} = 1$ and the vector form of the Euler equations (2.18)

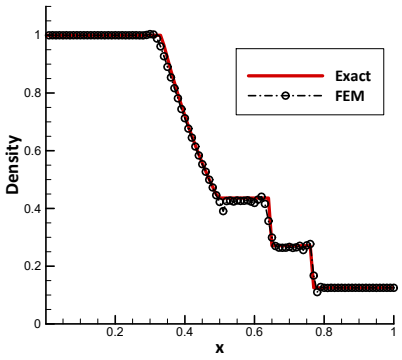

(a) Density

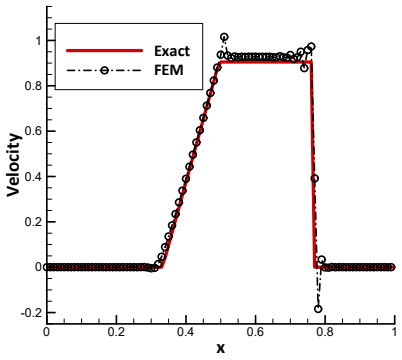

(b) Velocity

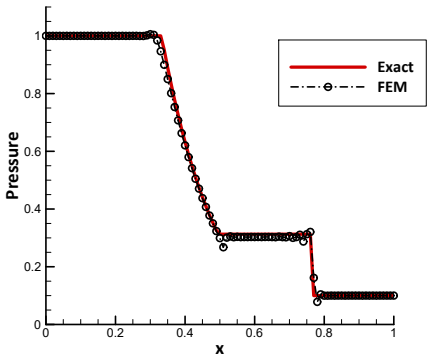

(c) Pressure

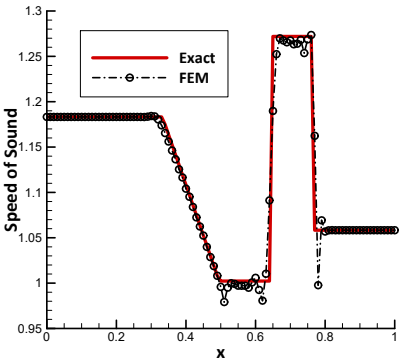

(d) Speed of Sound

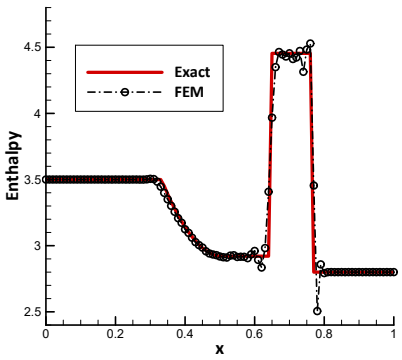

(e) Enthalpy

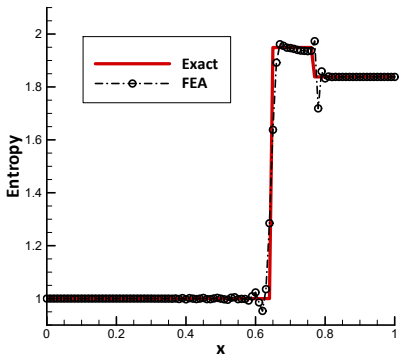

(f) Entropy

Figure 3.1: SOD's Shock Tube problem at $t = 0.15$. Analytical solution (red) compared with unsmoothed numerical solution (black). Numerical results show spurious oscillations near the shock fronts

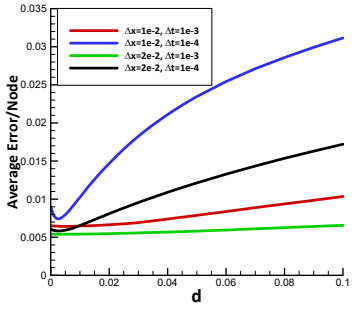

(a) Global smoothing

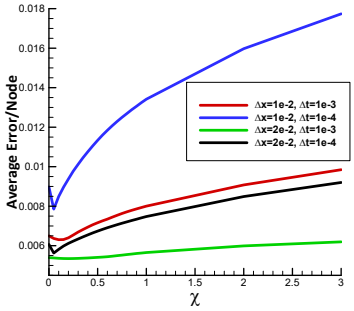

(b) Local smoothing

Figure 3.2: Average error per node as a function of the free global parameter d and of the free local parameter χ for the high-resolution scheme discussed in Section 2.3

is considered with

$$\mathbf{U} = \begin{bmatrix} u \\ Y \end{bmatrix}, \qquad \mathbf{F} = \begin{bmatrix} \frac{1}{2}u^2 \\ 0 \end{bmatrix}, \qquad and \ \mathbf{S} = \begin{bmatrix} -q\dot{Y} \\ \dot{Y} \end{bmatrix} \tag{3.1}$$

where u is energy and Y is mass fraction. The ZND detonation model is tested on Figure 3.4. Similar to SOD's Shock Tube problem, the test consists of two fluids at differing energies separated by a membrane at time $t = 0$. At $t > 0$ the membrane is removed and chemical reaction occurs producing a von Neumann spike that propagates at a constant speed. Numerical results for damped and undamped schemes are compared with the analytical solution [132] at $t = 2.5$. The unsmoothed solution shown on Figures 3.4(a) and 3.4(b) show good agreement with the exact solution and the distinct characteristics of the test are captured; however, spurious oscillations are observed near the shock front. The local high resolution scheme is introduced into the solution using $\chi = 0.2$. However, pressure is not included in this formulation thus, the shock sensing variable is replaced with energy gradients. This shows the adaptability of the scheme described in Section 2.3. The numerical results for the smoothed solution are shown on Figures 3.4(c) and 3.4(d). The spurious oscillations are dissipated and the numerical solution shows good agreement with the exact solution.

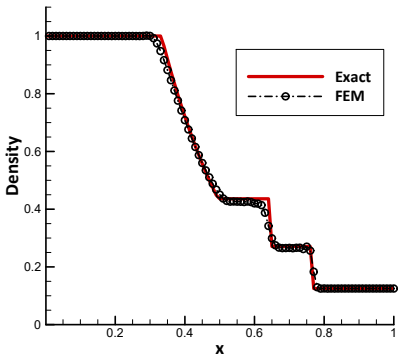

(a) Density

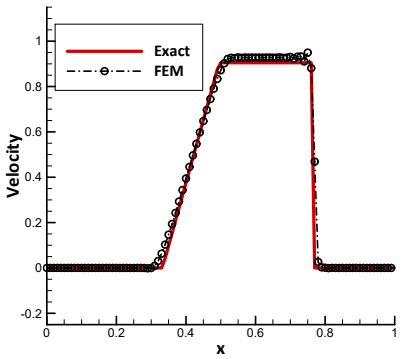

(b) Velocity

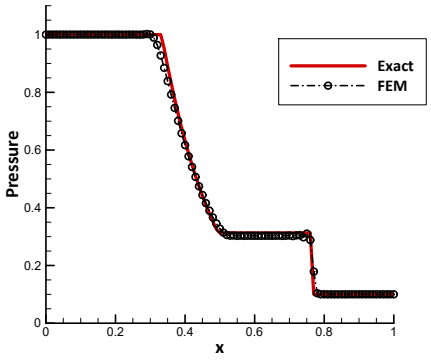

(c) Pressure

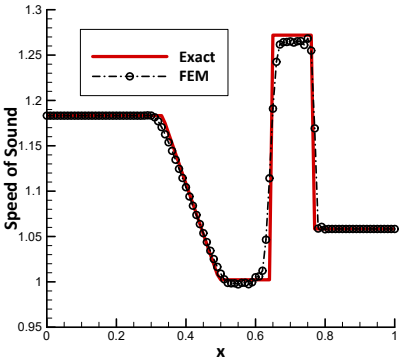

(d) Speed of Sound

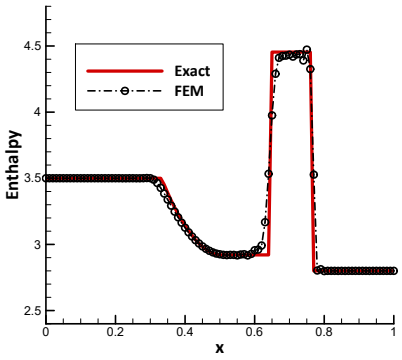

(e) Enthalpy

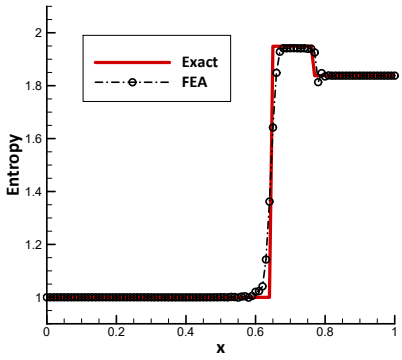

(f) Entropy

Figure 3.3: Sod's Shock Tube problem at $t = 0.15$. Analytical solution (red) compared with smoothed numerical solution (black). Numerical results show good agreement with the exact solution and the distinct characteristics of the test are captured

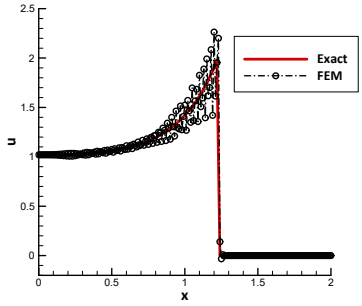

(a) Unsmoothed Energy

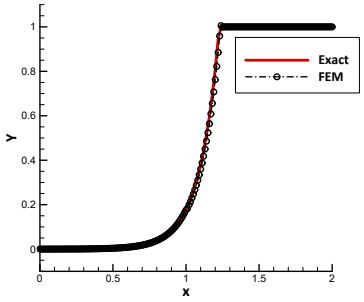

(b) Unsmoothed Mass Fraction

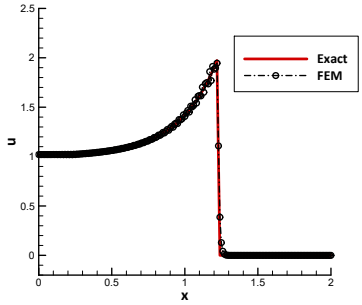

(c) Smoothed Energy

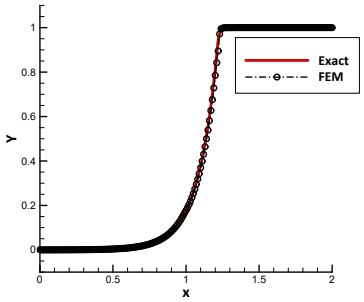

(d) Smoothed Mass Fraction

Figure 3.4: ZND detonation test problem at $t = 2.5$. Analytical solution (red) compared with unsmoothed(a)(b) and smoothed(c)(d) numerical solution (black). Numerical results show good agreement with the exact solution and the distinct characteristics of the test are captured

3.2 Model Validation: Polymer-Bonded Explosives

In this section, the models and methods used to simulate shock loading of polymer bonded explosives are tested and compared to experimental results. Although these models are informed by empirical data, it is important to validate them with results from experiments. Reaction rates, material behavior and shock features are tested in the following subsections. These tests are necessary in developing confidence in the solution scheme and a foundation for future results in later sections.

3.2.1 Shock Hugoniot

In reactive flow, it is necessary to represent the material response of both the unreacted material and the reaction detonation products. Equations of state for both extremes were presented in Section 2.1. The Mie-Grüneisen form given by Equations (2.7) and (2.8) is used to describe the behavior of the unreacted explosive. The Jones-Wilkins-Lee (JWL) form given by Equations (2.10) and (2.11) is used for the fully reacted material. Although material states are calculated for two extremes(unreacted/fully reacted) there exists a finite reaction zone where the explosive is partially reacted. This state of the explosive is determined by the burn fraction or the mass fraction of detonation products λ. The pressure and temperature for a partially reacted explosive is calculated using the mixture rules described in Equations (2.13) and (2.15). The constants for the solid equations of state (a, b, ν_0, c_v) and gaseous equations of state $(A, B, C, \nu_{CJ}, w, c_v)$ are determined experimentally and are taken from references [47, 48, 94]. They are described for PBX 9501, HMX and Polymeric binder on Table 3.1 and the appropriate units. These equations of state are function of density ($\nu = 1/\rho$) and internal energy ($e = E - 1/2\mathbf{u}^2$). Pressure and Temperature profiles for each material system are plotted below. According to the mixture rule shown on Equation (2.13), when $\lambda = 0$, the total pressure is equivalent to the pressure of Mie-Grüneisen form. When λ increases, the total pressure is a combination of the solid p_s, and gaseous p_g, equations of state. As λ increases and approaches unity, the total pressure is equivalent to the Jones-Wilkins-Lee (JWL) form. The total temperature follows the same mixing rule as shown on Equation (2.15). Equation of state parameters are fixed to the values recorded on Table 3.1. Adjusting the parameters to better fit experimental measurements is outside the scope of this thesis. Quantifying uncertainty in these parameters and will be left to future work.

The pressure and temperature profiles for PBX 9501 are shown in density-energy space on Figures 3.5(a)-3.5(f) and 3.6(a)-3.6(f) respectively. On the y-axis, specific internal energy varies from $e = 0.0 - 0.1\, Mbarcm^3/g$. On the x-axis density varies from $\rho = 1.0 - 3.5\, g/cm^3$. Although these bounds reach extreme values of pressure and temperature, they ensure that the regions of interest (detonation) are captured. The contours on Figures 3.5(a)-3.5(f) depict pressures ranging from $P = 0.0 - 1.0\, Mbar$. The contours on Figures 3.6(a)-3.6(f) depict temperatures ranging from $T = 295 - 5000\, K$. Ambient, or reference conditions of the explosive are $P = 0.0\, Mbar$ and $T = 295\, K$ with $\rho = 1.844\, g/cm^3$ and $e = 0.0\, Mbarcm^3/g$. Regions of blue may indicate nonphysical regimes; i.e. $(T < 0\, K)$. Figures 3.5(a)-3.5(f) and 3.6(a)-3.6(f) vary by burn fraction λ, where each figure varies by $\Delta\lambda = 0.2$. Thus the initial Figures 3.5(a) and 3.6(a), where $\lambda = 0$, refers to the Mie-Grüneisen equation of state, or Equations (2.7) and (2.8). These initial contours are used in

Constant	HMX	Binder	PBX 9501	Units
ρ_0	1.89	1.27	1.844	g/cm^3
T_0	295	295	295	K
$c_{v,s}$	1.1×10^{-5}	1.6×10^{-5}	1.1×10^{-5}	$Mbar\, cm^3/gK$
a	0.2901	0.24	0.2668	$cm/\mu s$
b	2.058	1.70	1.906	$--$
Γ	1.0	1.0	1.0	$--$
A	7.717	2.0879	8.52	$Mbar$
B	0.1064	0.0071	0.1802	$Mbar$
C	0.0085	0.0038	0.01207	$Mbar$
R_1	4.2	4.33	4.55	$--$
R_2	1.0	0.645	1.30	$--$
w	0.3	0.09	0.38	$--$
T_{CJ}	3000	2000	3000	K
$c_{v,CJ}$	2.0×10^{-5}	2.87×10^{-5}	1.0×10^{-5}	$Mbar\, cm^3/gK$
ν_{CJ}	0.3873	0.5901	0.4019	cm^3/g

Table 3.1: Material parameters for the unreacted Mie-Grüneisen and fully reacted Jones-Wilkins-Lee equations of state. Materials considered are HMX, polymeric binder and PBX 9501.

future sections to choose initial conditions that are sufficiently high to cause detonation in materials. The final Figures 3.5(f) and 3.6(f), where $\lambda = 1$, refers to the Jones-Wilkins-Lee equation of state, or Equations (2.10) and (2.11). Figures where $0 < \lambda < 1$ are goverend by the mixture rules described by Equations (2.13) and (2.15). As λ increases it is observed that contours for both pressure and temperature gradually shift. Areas that occupy high pressures grow smaller as λ increases. Alternatively, areas of high temperatures increases. Following the passage of a shock wave through a material the Hugoniot is determined. This curve, shown schematically on Figure 1.4, represents the various states of the material and is calculated experimentally. The linear relationship between shock speed U_s and particle velocity u_p is $U_s = a + bu_p$ where a and b are experimental constants. These constants are shown on Table 3.1. Matching Hugoniot data is necessary to validate detonation models especially since both equations of state are informed by the experimental constants a and b. The Hugoniot is calculated using Rankine-Hugoniot equations which relate the fluid properties before and after the shock.

The shock velocity U_s versus particle velocity u_p is shown on Figure 3.7 for PBX 9501. The experimental curve fit is shown in red, while the numerical results are shown in black. The numerical solution was obtained by choosing initial conditions sufficient enough to

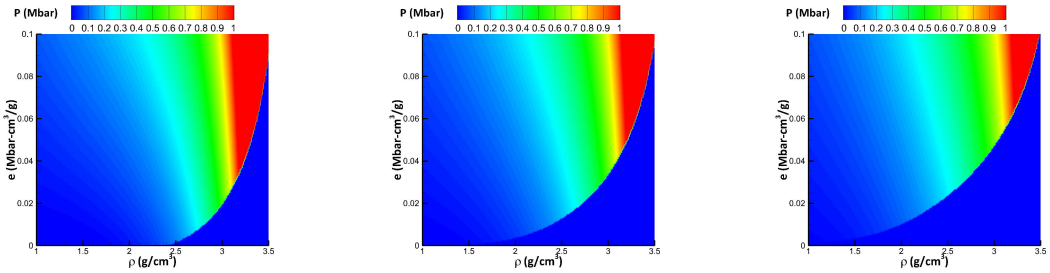

(a) $\lambda = 0.0$ (b) $\lambda = 0.2$ (c) $\lambda = 0.4$

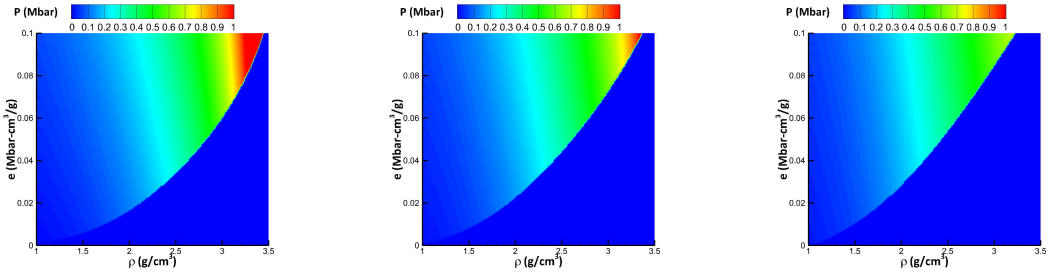

(d) $\lambda = 0.6$ (e) $\lambda = 0.8$ (f) $\lambda = 1.0$

Figure 3.5: Pressure profiles for PBX 9501 in density-energy space. Plots vary by $\Delta\lambda = 0.2$.

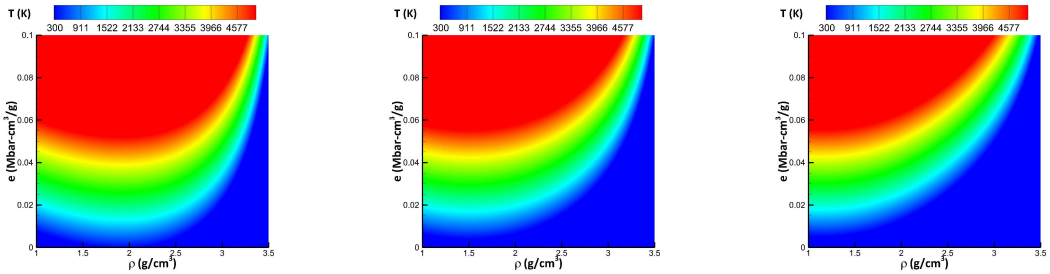

(a) $\lambda = 0.0$ (b) $\lambda = 0.2$ (c) $\lambda = 0.4$

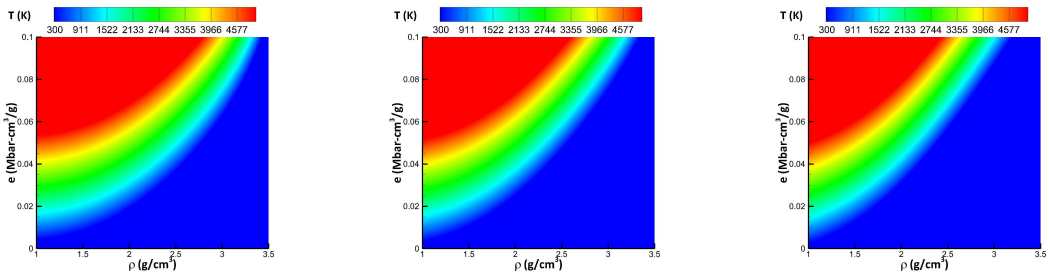

(d) $\lambda = 0.6$ (e) $\lambda = 0.8$ (f) $\lambda = 1.0$

Figure 3.6: Temperature profiles for PBX 9501 in density-energy space. Plots vary by $\Delta\lambda = 0.2$.

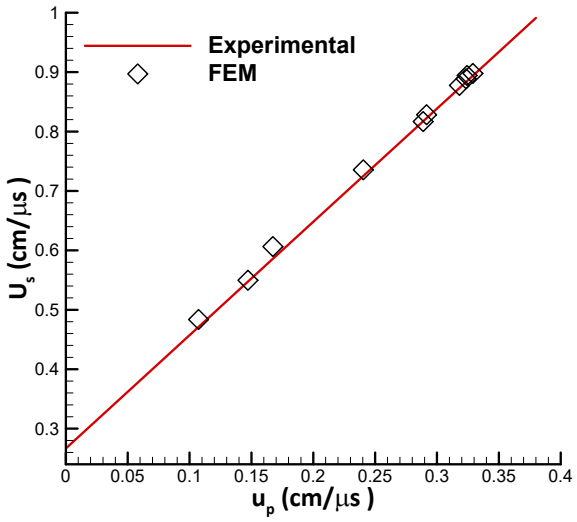

Figure 3.7: Shock velocity U_s versus particle velocity u_p for PBX 9501. Experimental curve fit (red) compared with numerical solution (black). Numerical results show good agreement with experimental data.

react the material and transition to detonation. For this experiment the Ignition and Growth model, Equation (2.16), was used as the reaction rate law. The numerical results show good agreement with the experimental curve fit signifying that the pre and post shock states are captured accurately, as expected.

Next, the pressure and temperature profiles for HMX are shown in density-energy space on Figures 3.8(a)-3.8(f) and 3.9(a)-3.9(f) respectively. On the x and y axes, density and energy varies with the same bounds of the previous pressure and temperature contours. The contours on Figures 3.8(a)-3.8(f) depict pressures ranging from $P = 0.0 - 1.0\,Mbar$. The contours on Figures 3.9(a)-3.9(f) depict temperatures ranging from $T = 295 - 5000\,K$. Ambient, or reference conditions of the explosive are $P = 0.0\,Mbar$ and $T = 295\,K$ with $\rho = 1.89\,g/cm^3$ and $e = 0.0\,Mbarcm^3/g$. Regions of blue may indicate nonphysical regimes; i.e. ($T < 0\,K$). Again, these figures vary by burn fraction λ, where each figure varies by $\Delta\lambda = 0.2$ and the initial Figures 3.8(a) and 3.9(a) refers to the Mie-Grüneisen equation of state and the final Figures 3.8(f) and 3.9(f) refers to the Jones-Wilkins-Lee equation of state. Compared to the PBX 9501, HMX equations of state follow similar trends by gradually shifting over λ. HMX and PBX behave similarly for pressure and temperature.

The shock velocity U_s versus particle velocity u_p is shown on Figure 3.10 for HMX. The experimental curve fit is shown in red, while the numerical results are shown in black.

The numerical solution was obtained by choosing initial conditions sufficient enough to react the material and transition to detonation. For this experiment the Ignition and Growth model, Equation (2.16), and the Arrhenius model, Equation (2.17), were used as the reaction rate law. The numerical results show good agreement with the experimental curve fit signifying that the pre and post shock states are captured accurately, as expected.

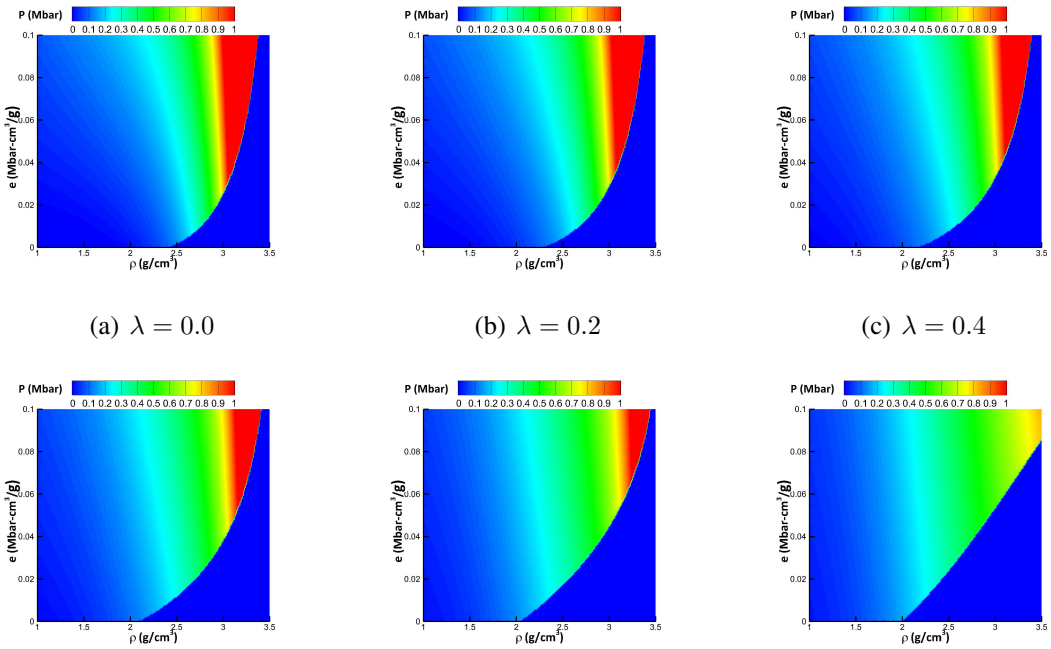

(a) $\lambda = 0.0$ (b) $\lambda = 0.2$ (c) $\lambda = 0.4$

(d) $\lambda = 0.6$ (e) $\lambda = 0.8$ (f) $\lambda = 1.0$

Figure 3.8: Pressure profiles for HMX in density-energy space. Plots vary by $\Delta\lambda = 0.2$.

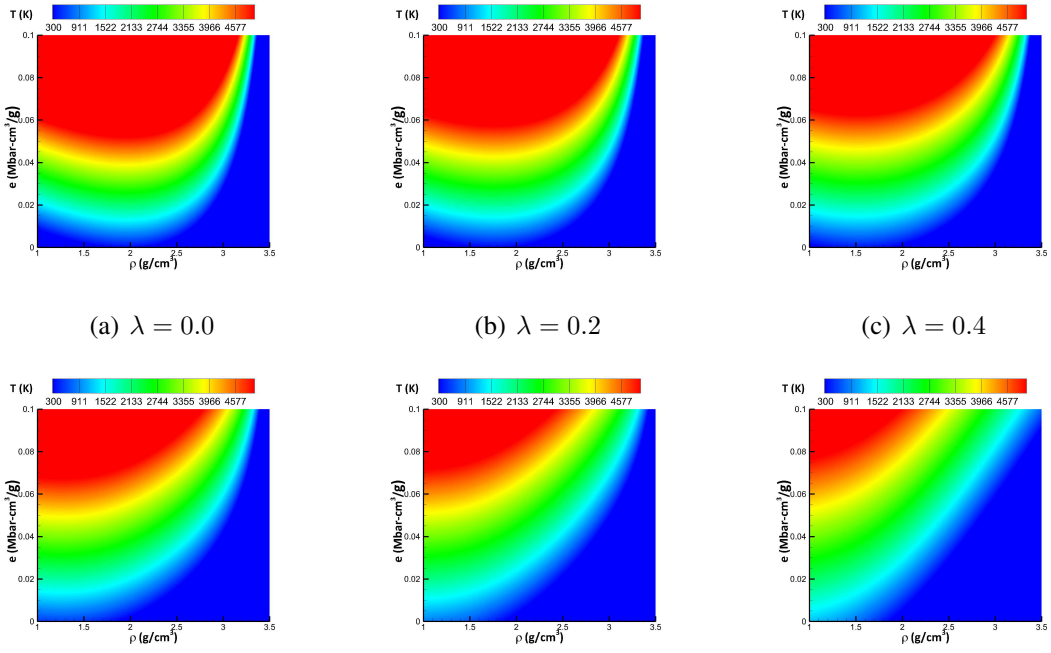

(a) $\lambda = 0.0$ (b) $\lambda = 0.2$ (c) $\lambda = 0.4$

(d) $\lambda = 0.6$ (e) $\lambda = 0.8$ (f) $\lambda = 1.0$

Figure 3.9: Temperature profiles for HMX in density-energy space. Plots vary by $\Delta\lambda = 0.2$.

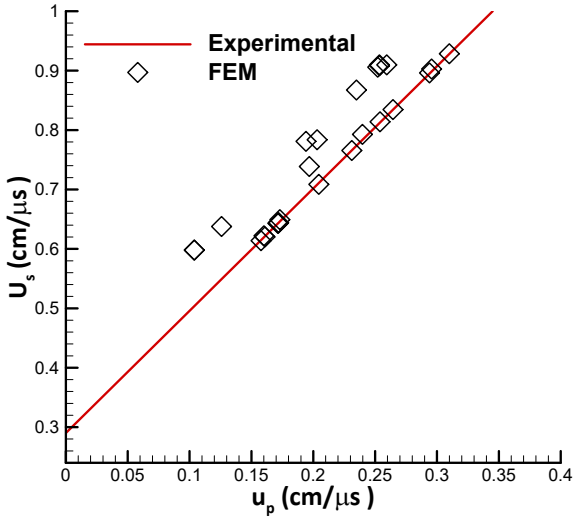

Figure 3.10: Shock velocity U_s versus particle velocity u_p for HMX. Experimental curve fit (red) compared with numerical solution (black). Numerical results show good agreement with experimental data.

Next, the pressure and temperature profiles for polymeric binder are shown in density-energy space on Figures 3.11(a)-3.11(f) and 3.12(a)-3.12(f) respectively. On the y-axis, energy varies with the same bounds of the previous pressure and temperature contours. However, the x-axis density varies from $\rho = 1.0 - 3.0\, g/cm^3$, a narrower band due to unrealistic regions ($T < 0\, K$). The contours on Figures 3.11(a)-3.11(f) depict pressures ranging from $P = 0.0 - 1.0\, Mbar$. The contours on Figures 3.12(a)-3.12(f) depict Temperatures ranging from $T = 295 - 5000\, K$. Ambient, or reference conditions of the explosive are $P = 0.0\, Mbar$ and $T = 295\, K$ with $\rho = 1.27\, g/cm^3$ and $e = 0.0\, Mbarcm^3/g$. These figures vary by burn fraction λ, where each figure varies by $\Delta\lambda = 0.2$ and the initial Figures 3.11(a) and 3.12(a) refers to the Mie-Grüneisen equation of state and the final Figures 3.11(f) and 3.12(f) refers to the Jones-Wilkins-Lee equation of state. Compared to the PBX and HMX equations of state for the binder follow similar trends, by gradually shifting with λ. Similar to PBX and HMX, as λ increases areas that occupy high pressures grow smaller. Areas of high temperatures also decrease like HMX temperature profiles. However, binder behaves much differently than PBX and HMX. At a density of $2.2g/cm^3$ and and energy of $0.02Mbarcm^3/g$ pressures and temperatures reach $0.29163Mbar$ and $388.22K$. This is substantially higher than PBX and HMX for pressure but an order of magnitude lower for temperature.

The shock velocity U_s versus particle velocity u_p is shown on Figure 3.13 for polymeric binder. The experimental curve fit is shown in red, while the numerical results are shown in black. The numerical solution was obtained by choosing initial conditions sufficient enough to react the material and transition to detonation. For this experiment the Ignition and Growth model, Equation (2.16), and the Arrhenius model, Equation (2.17), were used as the reaction rate law. The numerical results show good agreement with the experimental curve fit signifying that the pre and post shock states are captured accurately, as expected.

3.2.2 Run-to-Detonation

Run-to-detonation is the main measurement used to assess an explosive's sensitivity and is calculated as a function of input pressure. It is determined experimentally by embedding gauges within the explosive at multiple points. The material is then shocked with an impactor and the shock-to-detonation wave profiles are measured. A schematic of this process is shown on the left of Figure 1.2. This experiment is repeated for various input pressures, each corresponding to different run-to-detonation quantities. The data generated from these experiments are used to make Pop-plots, logarithmic plots of run-to-detonation distance versus incident shock. When the data is plotted in a logarithmic scale the rela-

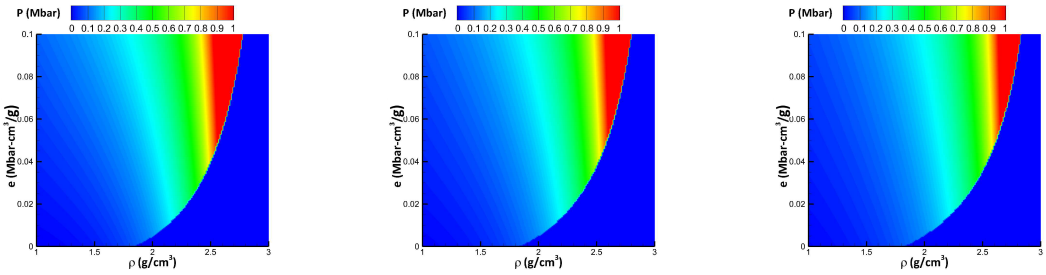

(a) $\lambda = 0.0$ (b) $\lambda = 0.2$ (c) $\lambda = 0.4$

(d) $\lambda = 0.6$ (e) $\lambda = 0.8$ (f) $\lambda = 1.0$

Figure 3.11: Pressure profiles for polymeric binder in density-energy space. Plots vary by $\Delta\lambda = 0.2$.

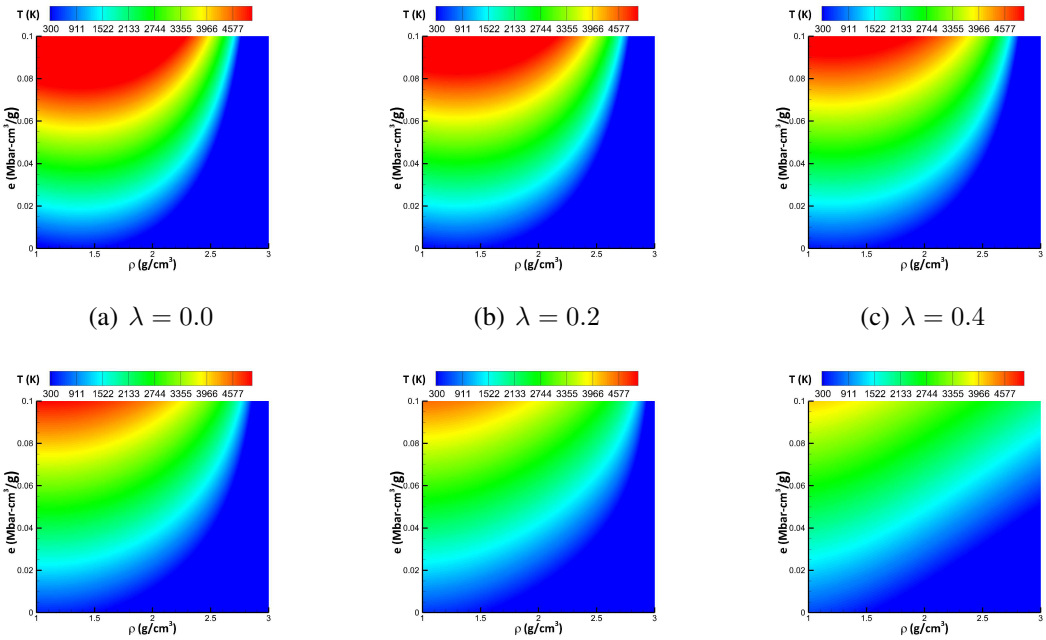

(a) $\lambda = 0.0$ (b) $\lambda = 0.2$ (c) $\lambda = 0.4$

(d) $\lambda = 0.6$ (e) $\lambda = 0.8$ (f) $\lambda = 1.0$

Figure 3.12: Temperature profiles for polymeric binder in density-energy space. Plots vary by $\Delta\lambda = 0.2$.

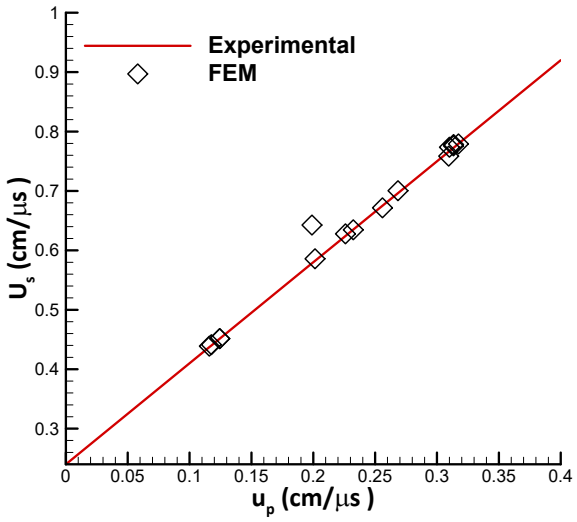

Figure 3.13: Shock velocity U_s versus particle velocity u_p for polymeric binder. Experimental curve fit (red) compared with numerical solution (black). Numerical results show good agreement with experimental data.

tionship between run-to-detonation and incident pressure appears linear as shown schematically on the right of Figure 1.2. Experimentally measured pop-plot data is compared to numerical results obtained for PBX and HMX material systems. It is important to validate the numerical model with pop-plot data as it is an accurate assessment of reaction rate laws. Table 3.2 shows the reaction rate constants for the Ignition and Growth model described by Equation (2.16) taken from reference [46]. Table 3.3 shows the reaction rate constants for the Arrhenius model described by Equation (2.17) taken from reference [94]. Adjusting the parameters to better fit experimental measurements is outside the scope of this thesis; therefore, they are fixed for this work. Quantifying uncertainty in these parameters and will be left to future work.

First, detonation of PBXs are studied, using the material parameters of PBX 9501 and the reaction parameters for the Ignition and Growth model, shown on Table 3.2. A sample of length $L = 1.0cm$ is shocked on the left boundary of the domain at various input pressures. Virtual gauges are are placed at $0.02cm$ increments. The domain is discretized in time and space with a $\Delta x = 5 \times 10^{-4} cm$ and a $\Delta t = 1 \times 10^{-4} \mu s$. Spatial discretization effects are considered in the following section. The following plots show a PBX sample shocked with an input pressure of approximately $P = 15 Mbars$. Figures 3.14(a)-3.14(d) show the conserved quantities, density ρ, velocity u, total energy E and the burn fraction λ. Each plot contains various curves corresponding to differing gauge positions. The x-

Constant	PBX	Units
I	44	Z in μs^{-1}
G	200	$\mu s^{-1} Mbar^{-\tau_4}$
τ_1	0.222	$--$
τ_2	4.0	$--$
τ_3	0.666	$--$
τ_4	1.6	$--$

Table 3.2: Reaction rate parameters for the Ignition and Growth Model for PBX

Constant	HMX	Binder	Units
$ln(Z)$	12.5	13.2	Z in μs^{-1}
E_1	1.49	1.49	$Mbar\, cm^3/mol$
q	0.05861	0.044959	$Mbar\, cm^3/g$

Table 3.3: Reaction rate parameters for Arrhenius Model for HMX and polymeric binder

Constant	PBX 9501	Units
$Z = k$	2.85×10^5	μs^{-1}
$E_1/R = T_a$	17900	K
q	0.05861	$Mbar\, cm^3/g$

Table 3.4: Global Reaction rate parameters for PBX 9501

axis represents time in μs, showing how each conserved quantity at a specific gauge point changes in time. In general, it is obvious to see that once the material is shocked it transitions to steady detonation. At the initial gauge, density velocity and energy capture the initial shock. As time increases, chemical reaction occurs as observed by the burn fraction and von Neumann spikes. The material is fully reacted and the detonation wave travels at a constant speed.

Figure 3.15(a) shows the pressure profiles of multiple gauges as a function of time. Although there are more gauge location colors correspond to gauges from the previous figure. Comparing this plot to the schematic the left of Figure 1.2, it is obvious that the transition to detonation occurs. The initial gauge captures the input pressure of $P = 15Mbars$. As the shock wave propagates chemical reaction occurs. A detonation wave precedes and is driven by the zone of chemical reaction, in turn creating high pressures and temperatures necessary to drive chemical reaction. This coupling provides the necessary conditions to maintain fast chemical reaction and thus the self-sustaining propagation of the detonation wave. The transition to detonation occurs near the gauge located at $x = 0.192cm$. A peak pressure of $P = 57.0Mbars$ is reached and maintained as steady detonation is reached. The location of the shock front is tracked on Figure 3.15(b). The x-axis shows the location of the wave front in cm, and the y-axis shows the time in μs. When compared to the schematic to the right of Figure 1.1, it is obvious that the transition to detonation occurs. Taking the inverse of the slope of this plot gives the detonation velocity D. Initially the slope remains constant, as chemical reaction occurs, the shock wave accelerates and the slope changes to the constant detonation velocity. The detonation velocity will be studied in the following section.

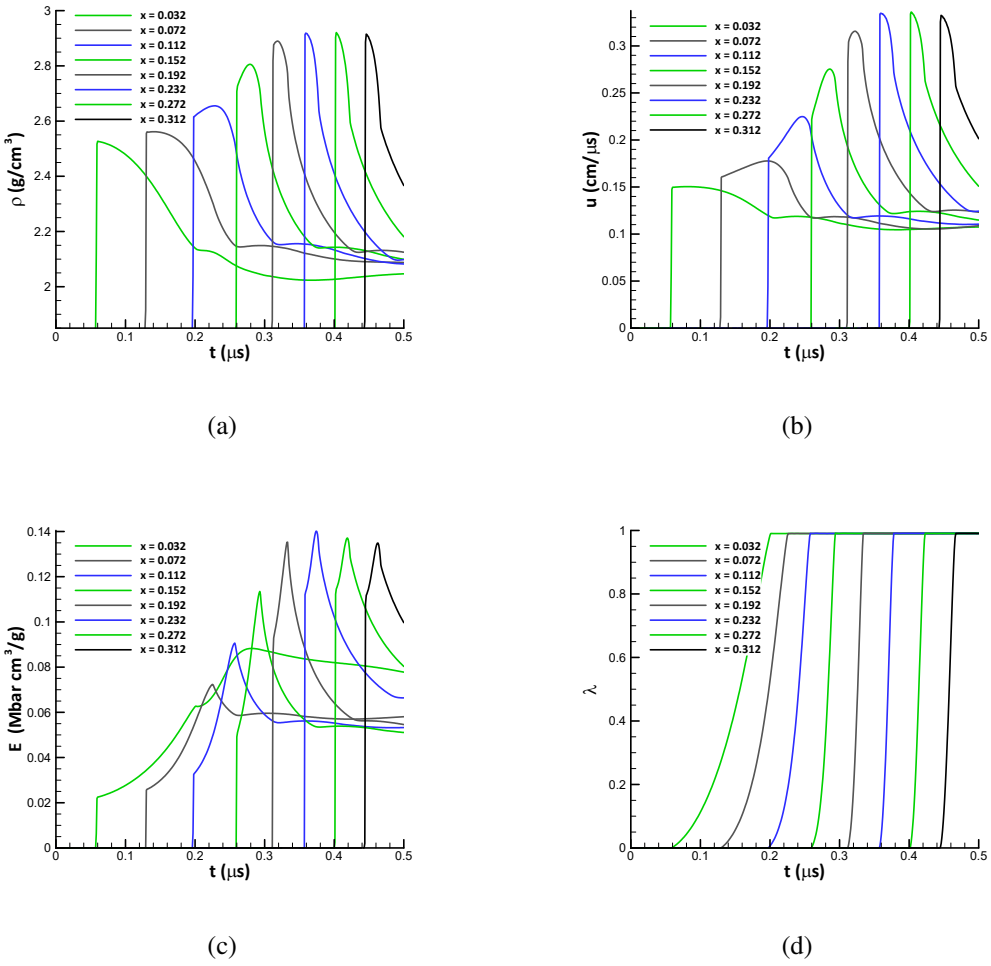

Figure 3.14: Conservation variables as a function of time as a PBX sample is shocked with an input pressure $P = 15Mbars$. Colors correspond to varying gauge positions.

The data generated from this experiment is used to make a Pop-plot, where the run-to-detonation distance is plotted versus the incident shock pressure. This experiment is repeated for multiple shock pressures, generating multiple run-to-detonation distances. Numerical results for the PBX shock loading experiments are shown on Figure 3.16 and are compared to a host of experiments for various PBXs [47, 133, 134]. Logarithmic plots of run-to-detonation distance versus incident shock are shown on Figure 3.16. Note the x-axis is shown in GPa and the y-axis is shown in mm, common units for these plots. Here experimental data is represented by variously colored scatter points. Numerical results are represented by "X"s where the solid line is the best curve. Experimental results range from $2 - 25GPa$ with run-to-detonation distances below $x = 1mm$ and as long as $x = 25mm$. Numerical results are in the pressure ranges of $P = 4 - 18GPa$ and are within the range

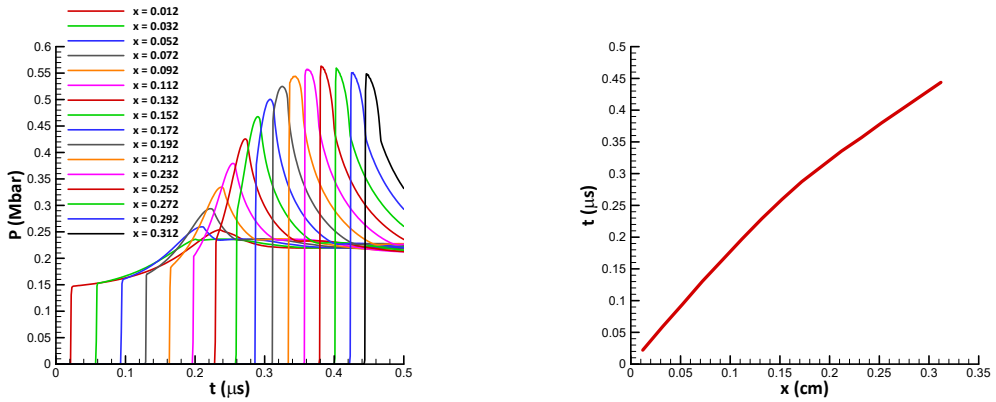

(a) Pressure as a function of time. Colors correspond to varying gauge positions

(b) Shock front location

Figure 3.15: Pressure profiles and shock front of PBX sample. The transition to detonation occurs near the gauge located at $x = 0.192cm$.

of experimental data. Numerical results show good agreement with experimental results in lower pressure ranges but begin to diverge around $P = 9GPa$. Numerical results show that the explosive is less sensitive that experimental data. For example, for an incident shock of $P = 14GPa$ numerical results give a run-to-detonation distance less than $x = 1mm$ while numerical results give a distance near $x = 2mm$; i.e. for the same input pressure the numerical simulation takes a greater distance, and time, to reach steady detonation than the experimental data for pressures above $P = 9GPa$. This same behavior is observed on Figure 6 in reference [46]. In the cited work, the Ignition and Growth parameters listed on Table 3.2 are used and are adjusted for each input pressure. No such attempt has been made in this work to adjust parameters. However, for fixed parameter, this work matches the same trend. Figure 3.17 shows the numerical curve fit from the previous plot and the experimental curve fit provided in reference [46]. This plot is in good agreement with the Figure 6 in the cited work. This is expected as the Ignition and Growth parameters listed on Table 3.2 are taken from this reference, thus validating the finite element model in this work.

Next, detonation of HMX is studied, using the material constants of HMX found on Table 3.1. For this experiment both Ignition and Growth model and the Arrhenius model is considered with constants taken from Tables 3.2 and 3.3. The same experimental setup is considered; a sample of length $L = 1.0cm$ is shocked on the left boundary of the domain at various input pressures. Virtual gauges are placed at $0.02cm$ increments. The domain is discretized in time and space with a $\Delta x = 5^{-4}cm$ and a $\Delta t = 1^{-4}\mu s$. This experiment is repeated for multiple shock pressures, generating multiple run-to-detonation distances. Nu-

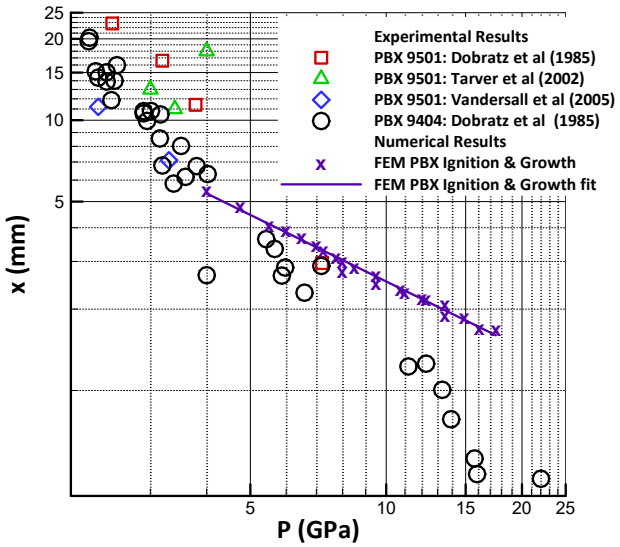

Figure 3.16: Logarithmic plots of run-to-detonation distance versus incident shock pressure for PBXs. Experimental results shown as scatter points, with numerical results represented by ”X”s with best fit. Results show good agreement in lower pressure ranges and are less sensitive in higher pressure ranges.

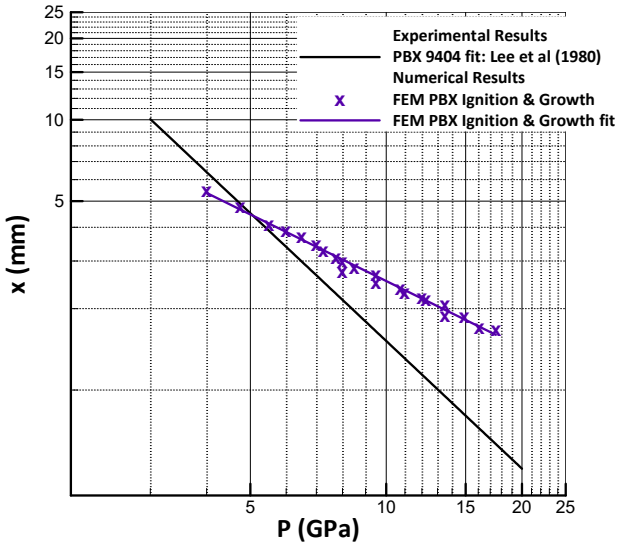

Figure 3.17: Logarithmic plots of run-to-detonation distance versus incident shock pressure for PBXs. Experimental curve fit compared to numerical curve fit shows expected behavior; numerical results are less sensitive than experimental results.

merical results for HMX shock loading experiments are shown on Figure 3.18 and are compared to experiments and numerical studies for both solvent-pressed HMX (poly-crystal) and single crystal HMX [47, 94]. Logarithmic plots of run-to-detonation distance versus incident shock are shown on Figure 3.18, with the x-axis shown in GPa and the y-axis shown in mm. Here, data from cited works, including experimental and numerical studies are represented by variously colored scatter points. Numerical results are represented by solid lines through scatter points as best curve fits. Results range from $3 - 45GPa$ with run-to-detonation distances below $x = 1mm$ and as long as $x = 10mm$.

Comparing numerical results of HMX using the Ignition and Growth Model (red line) to experimental results of solvent-pressed HMX (blue scatter points) shows good agreement. Much like the PBX study before, HMX shows good agreement with lower pressures but is less sensitive to higher pressures when compared to these experiments. Good agreement is expected for the this model as Ignition and Growth Models incorporate ignition mechanisms (hot spots) that are observed when shock loading solvent-pressed HMX. These observations validate the Ignition and Growth model for HMX in this work.

However, when comparing the Ignition and Growth Model to single crystal data (pink and orange scatter points), there is a great disparity. Single crystal data performs much more like a homogeneous explosive rather than a heterogeneous explosive, which are compared on Figure 1.1. In general homogeneous explosives are less sensitive than heterogeneous explosives which have mechanisms that create localized regions of energy release (hot spots). As an example, for a run-to-detonation distance of $x = 2mm$ numerical results using the Ignition and Growth model need an input pressure near $P = 17GPa$. For the numerical single crystal study [94], a $P = 26GPa$ input pressure is required. Similarly a higher input pressure $P = 35 - 40GPa$ is required to reach the same run-to-detonation distance for the experimental data [47]. However, when comparing these cited results with numerical results for the Arrhenius model (green line) there is better agreement. It is observed that the Arrhenius model performs like a homogeneous explosive, due to its lack of hot spot mechanisms and matches well with the numerical single crystal study. When comparing numerical results to the experimental data (orange scatter), the numerical results are more sensitive. As an example, for a run-to-detonation distance of $x = 4mm$ numerical results need an input pressure near $P = 25GPa$. For the experimental single crystal data, a $P = 35GPa$ input pressure is required. This sensitivity disparity is not addressed in this work as agreement with the other numerical study validates the Arrhenius model for shock loading of HMX. To summarize, all numerical results from this work, including PBX and HMX Ignition and Growth and Arrhenius models, and are shown on Figure 3.19. Comparing Ignition and Growth models for PBX and HMX, it is observed that PBX is more

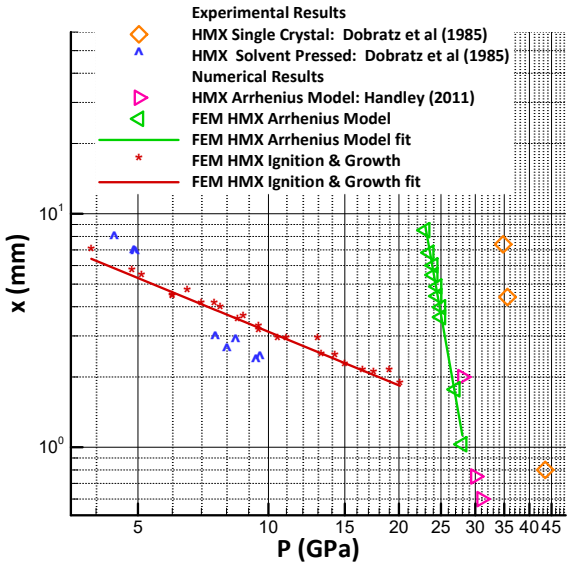

Figure 3.18: Logarithmic plots of run-to-detonation distance versus incident shock pressure for HMX. Cited experimental and numerical results shown as scatter points, with numerical results represented by best fit curves. Ignition and Growth model results show good agreement solvent-pressed experimental data. Arrhenius model results show good agreement single crystal data.

sensitive than HMX. As an example, an input pressure of $P = 10GPa$, PBX produces a run-to-detonation distance of $x = 2.5mm$ while HMX produces a distance of $x = 3.0mm$. This behavior is supported by experimental data [47] as the polymeric matrix in PBX is known to affect detonation [7].

3.2.3 Mesh Density Studies

In this section the effects of mesh fidelity on known shock values for differing reaction models and materials are studied. It is necessary to validate this model with these features needed to fully capture the reaction zone. First, PBXs are considered. A sample of length $L = 1.0cm$ is shocked on the left quarter of the domain at a pressure sufficient to prompt ignition. The goal is to transition to steady detonation to measure shock features, such as detonation velocity and peak pressure. Density and energy values selected produce a pressure near $P = 0.55Mbar$. Results for this experiment have a fixed time step of $\Delta t = 1 \times 10^{-4} \mu s$ and are shown for various mesh densities on Figures 3.20(a)-3.20(f). The x-axis of these figures represents position in cm and the y-axis represents pressure in $Mbar$. Each plot contains pressure profiles at various times with an increment of $t_{plot} = 0.05\mu s$

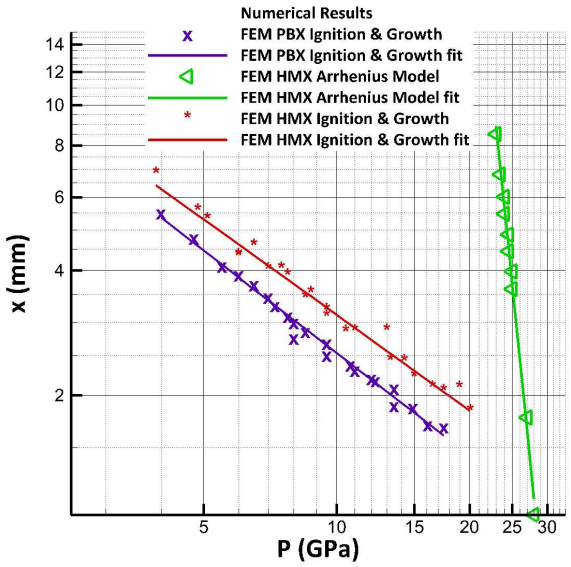

Figure 3.19: Logarithmic plots of run-to-detonation distance versus incident shock pressure for All numerical results. PBX results are more sensitive than HMX, illustrating the importance of the effects polymeric binder has on reaction rates, and sensitivity.

for a duration of $t = 0.50\mu s$. These plots show how pressure values at a specific location changes over time. Mesh fidelity size varies from 500 elements per cm to 3000 elements per cm.

Figures 3.20(a)-3.20(f) show that each experiment transitions and reaches steady detonation from the initial shock. For the initial study, Figure 3.20(a), the peak pressure at steady detonation is below the initial pressure of $P = 0.55Mbar$ and reaches a peak pressure of $P = 0.522Mbar$. As fidelity increases, the peak pressure increases until converging to a pressure above the input shock. As an example, Figure 3.20(d) has a peak pressure of $P = 0.556Mbar$ after steady detonation. At $t = 0.5\mu s$ the shock front of the $500ELM/cm$ case reaches $x = 0.646cm$. At higher fidelity, it is clear that the shock front passes this value. The shock front of the $2000ELM/cm$ is located at $x = 0.6537cm$. This shows that mesh density effects, peak pressures and shock speeds. When increasing fidelity further, the shock front of the $3000ELM/cm$ is located at $x = 0.6537cm$ showing convergence. Furthermore, Figure 3.20(f) has a peak pressure of $P = 0.57Mbar$.

To further study convergence, shock features are compared to published values. The CJ and ZND detonation theories discussed in Section 1.2 allow for the calculation of material properties along the reaction zone. Recall, the solid material is shocked to the von Neumann point. As chemical reaction occurs, pressure decreases along the Rayleigh line, through the partially-reacted region until it reaches the Chapman-Jouguet point, the point where

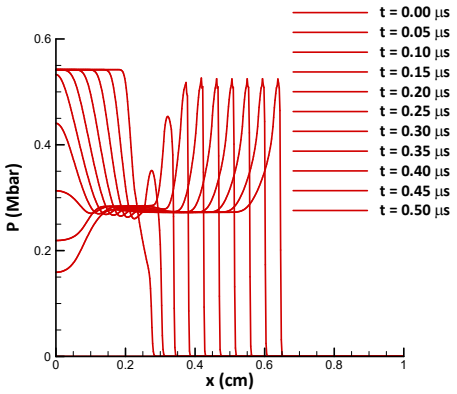

(a) 500 ELM/cm

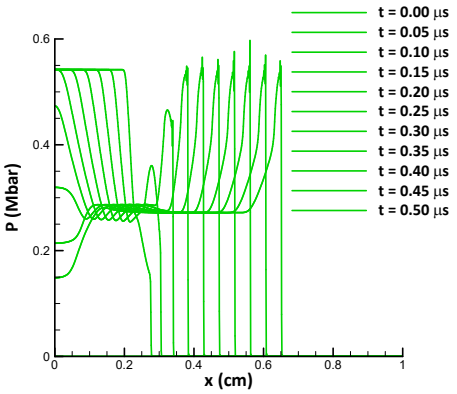

(b) 1000 ELM/cm

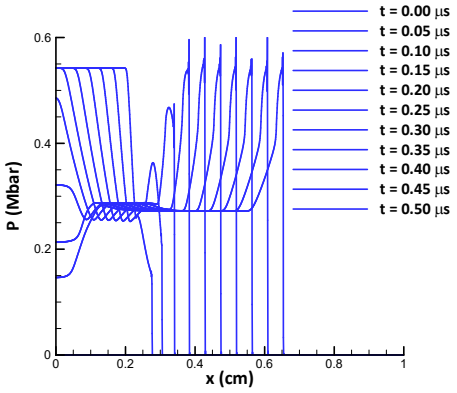

(c) 1500 ELM/cm

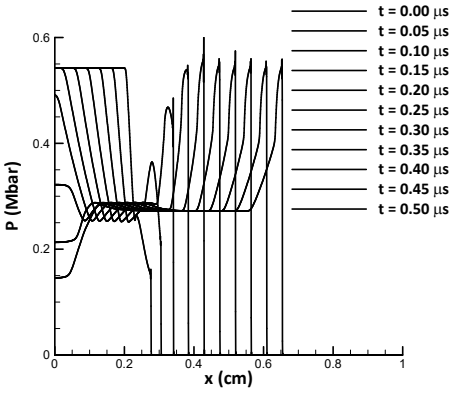

(d) 2000 ELM/cm

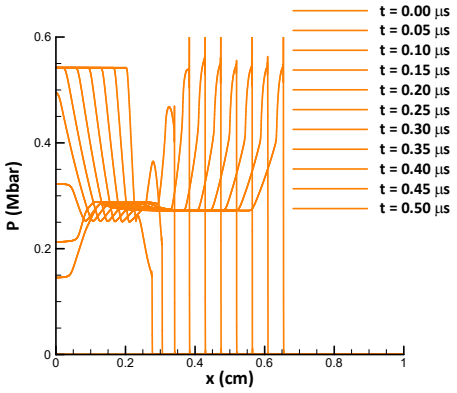

(e) 2500 ELM/cm

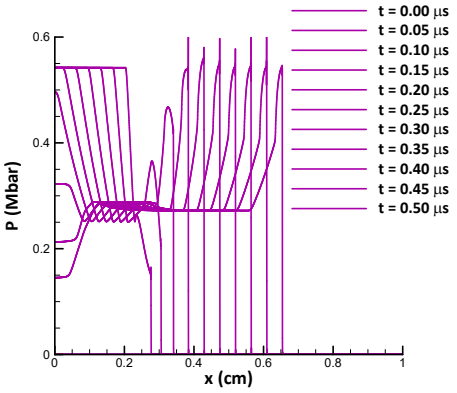

(f) 3000 ELM/cm

Figure 3.20: PBX sample shocked at various mesh densities. Pressure versus position plots show the effect fidelity has on peak pressures and wave speeds.

all reaction has occurred. This is depicted schematically on Figure 1.4. Relative error of each quantity is plotted along the y-axis of each of the following figures, where the target values are taken from references [46, 47] and are displayed on Table 3.5. The x-axis shows the time at which the quantity is measured. These times are after the material has reached steady detonation. Each bar represents a varying mesh density corresponding to the color shown on Figures 3.20(a)-3.20(f). First the detonation velocity D is considered. This is calculated by measuring the location of the detonation wave, or the inverse of the slope on Figure 3.15(b). At the initial time t_1, the detonation velocity for the $500ELM/cm$ case produces an error of 65%. As the solution continues the error is reduced and falls below 65%. In fact, each of the solutions produce larger errors at the initial time but are well converged by the end of the simulation. Adding more fidelity greatly reduces the initial error (below 20%) but does not significantly impact the error at later time points. For the detonation velocity, it is sufficient to say that the mesh has converged to the value near the published value($< 5\%$) with a best value of $D = 0.880cm/\mu s$.

Next, the von Neumann conditions are considered on Figures 3.21(b)- 3.21(d). The von Neumann Pressure is given as $P_{vn} = 0.563Mbar$ the error relative to this value is plotted on Figure 3.21(b). The initial mesh of $500ELM/cm$ produces the largest error over the duration of the simulation, never reaching below 10%. Higher fidelity is required to accurately capture the von Neumann Pressure; values above $500ELM/cm$ produce values below 5% with the best value of $P_{vn} = 0.563Mbar$ reported on Table 3.5. The velocity is also calculated at the von Neumann point and is compared on 3.21(c). Again the coarsest mesh gives the highest error ($\approx 10\%$) while increasing the fidelity produces relatively low error($\approx 5\%$) with the best value of $u_{vn} = 0.341cm/\mu s$. Next the relative volume at the von Neumann point is compared on Figure 3.21(d). Although the $500ELM/cm$ case produces the largest error, it is relatively close to the finer meshes. Error fluctuates near 5% for all cases with the best value of $V_{vn}/V_0 = 0.624$. Results from the von Neumann point indicate that a mesh size of $500ELM/cm$ is not sufficient enough to accurately capture values at that point while mesh sizes above are.

To conclude this experiment, the Chapman-Jouguet conditions are considered on Figures 3.21(e)- 3.21(f). The Chapman-Jouguet Pressure relative errors are are shown on 3.21(e). Similar to the von Neumann pressure, the $500ELM/cm$ case produces the most error. Adding fidelity to the simulation improves the accuracy but not by much. Error fluctuates near 15% with the highest fidelity $3000ELM/cm$ producing a pressure of $P_{CJ} = 0.413Mbar$, the value reported on Table 3.5. Finally, the Chapman-Jouguet Velocity is compared on Figure 3.21(f). As expected, the velocity converges with increasing fidelity; however, the relative error again is near 15%. The best velocity is reported as

$u_{CJ} = 0.250cm/\mu s$. In general, results near the von Neumann point are more accurate than those at the Chapman-Jouguet Pressure. The difference, made be attributed to differing numerical schemes, or material models. For instance reference [46] uses JWL eqeations for both reacted and unreacted explosive. To summarize, mesh sizes above $500ELM/cm$ are sufficient in capturing reaction zone properties for shock loading of PBXs.

	Lee & Tarver (1980)	Dobratz & Crawford (1985)	FEM
von Neumann			
$D(cm/\mu s)$	0.880	$0.880 - 0.883$	0.880
$P_{vn}(Mbar)$	0.563	$--$	0.563
$u_{vn}(cm/\mu s)$	0.347	$--$	0.341
V_{vn}/V_0	0.606	$--$	0.624
Chapman-Jouguet			
$P_{CJ}(Mbar)$	0.370	0.375	0.413
$u_{CJ}(cm/\mu s)$	0.229	$--$	0.250

Table 3.5: Results for von Neumann and Chapman-Jouguet values. Best numerical values are reported. Detonation velocity and von Neumann values are captured well.

Next, the same experiment is performed for a $L = 1.0cm$ sample of HMX using the Ignition and Growth model. The left quarter of the domain is shocked to a pressure of $P = 0.55Mbar$. Experiments use a fixed time step of $\Delta t = 1 \times 10^{-4}\mu s$ with mesh sizes ranging from 500 elements per cm to 3000 elements per cm. Pressure profiles are shown on Figure 3.22(a)-3.22(f) at various times with an increment of $t_{plot} = 0.05\mu s$ for a duration of $t = 0.50\mu s$. These figures show that each experiment transitions and reaches steady detonation from the initial shock. For the initial study, Figure 3.22(a), the peak pressure at steady detonation is below the initial pressure $P = 0.53Mbar$. As fidelity increases, the peak pressure increases until converging to a pressure above the input shock. As an example, Figure 3.22(a) has a peak pressure of $P = 0.57Mbar$ after steady detonation. At $t = 0.5\mu s$ the shock front of the $500ELM/cm$ case reaches $x = 0.659cm$. The shock front of the $2000ELM/cm$ is located at $x = 0.66cm$. When increasing fidelity further, the shock front of the $3000ELM/cm$ is located at $x = 0.66cm$ showing convergence. Furthermore, Figure 3.22(f) has a peak pressure of $P = 0.57Mbar$. To summarize, mesh density affects peak pressure and does not affect detonation velocity to the same degree as the previous PBX tests. Calculations above 1000 elements per cm are mesh resolved with the peak

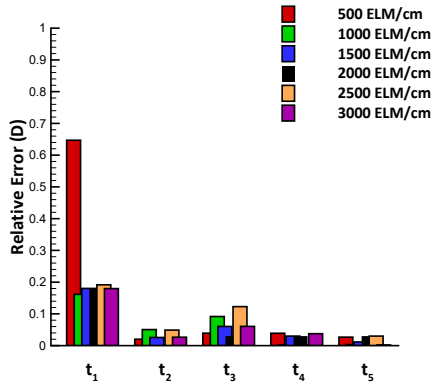

(a) Detonation Velocity

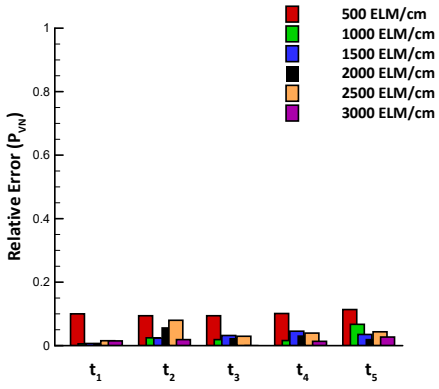

(b) von Neumann Pressure

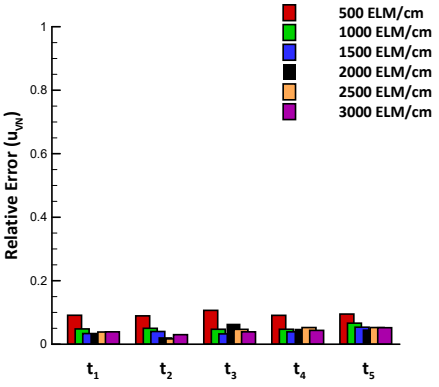

(c) von Neumann Velocity

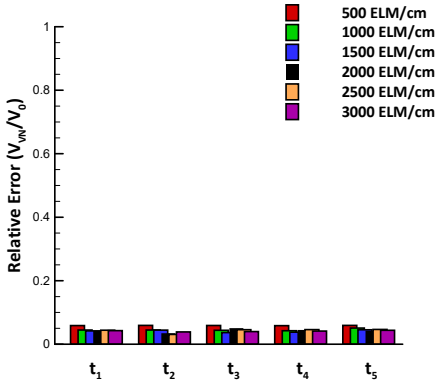

(d) von Neumann Relative Volume

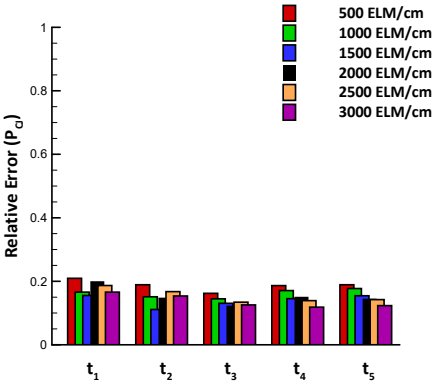

(e) Chapman-Jouguet Pressure

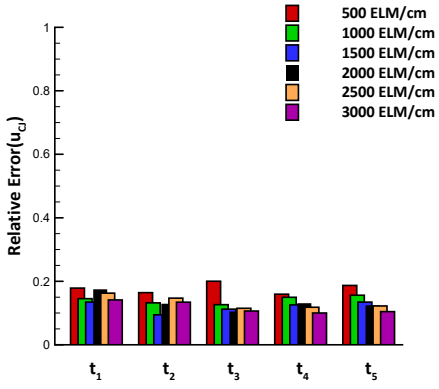

(f) Chapman-Jouguet Velocity

Figure 3.21: Mesh Density study for PBX material properties at von Neumann and Chapman-Jouguet points. Relative error is plotted versus time where each bar represents a varying mesh density. Error bars show that the reaction zone is accurately captured.

pressure and detonation velocity of HMX using the Ignition and growth model converged.

To study the convergence of detonation velocity, relative error is plotted on Figure 3.23(a) with a target velocity taken from reference [47]. Each bar represents a varying mesh density corresponding to the color shown on Figures 3.22(a)-3.22(f). The y-axis displays relative error and the x-axis shows the time at which the quantity is measured. Note, these times are after the material has reached steady detonation. The detonation velocity D is calculated by measuring the location of the detonation wave at multiple time increments. At the initial time t_1, the detonation velocity for the $500ELM/cm$ case produces an error of less than 1%. In fact, doubling the mesh size to $1000ELM/cm$ increases the error. Max error fluctuates between mesh densities with error below 5%. Again, this shows that mesh density does not affect detonation velocity as significantly as the previous PBX tests. The detonation velocity for HMX using Ignition and Growth model is converged with the best value reported on Table 3.6 as $D = 0.915cm/\mu s$.

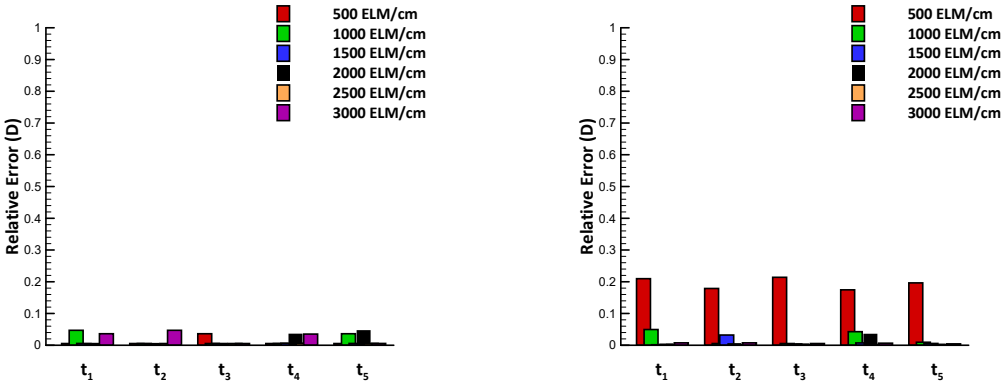

(a) Ignition and Growth Model

(b) Arrhenius Model

Figure 3.23: Mesh Density study on relative error of detonation velocity for shock loading of HMX. Detonation velocity converges for both models.

	Dobratz & Crawford (1985)	FEM (IG)	FEM (Arrhenius)
$D(cm/\mu s)$	0.911	0.915	0.9112

Table 3.6: Results for detonation velocity of HMX using Ignition and Growth model and Arrhenius model. Best values match cited works.

Next, the same experiment is performed for a $L = 1.0cm$ sample of HMX using an

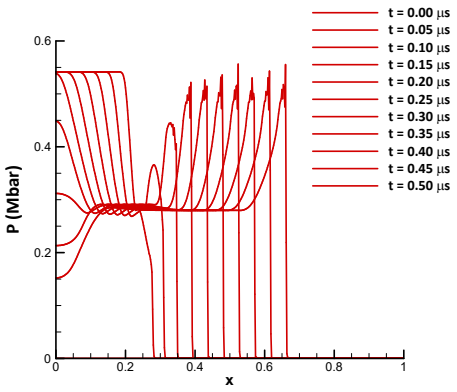

(a) 500 ELM/cm

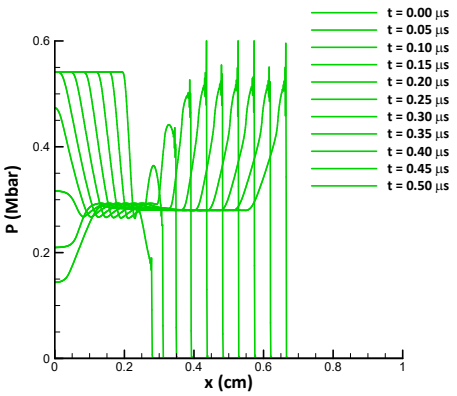

(b) 1000 ELM/cm

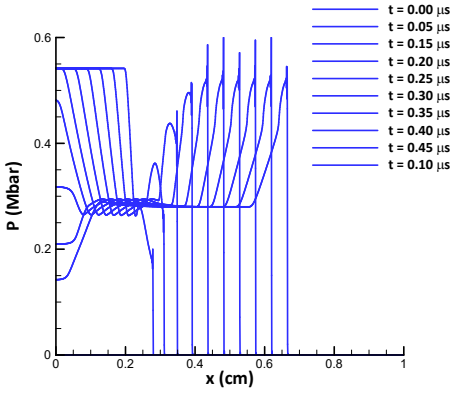

(c) 1500 ELM/cm

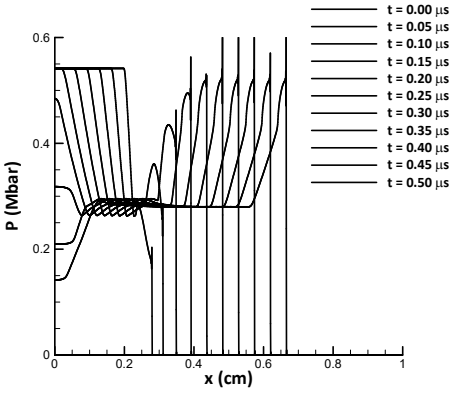

(d) 2000 ELM/cm

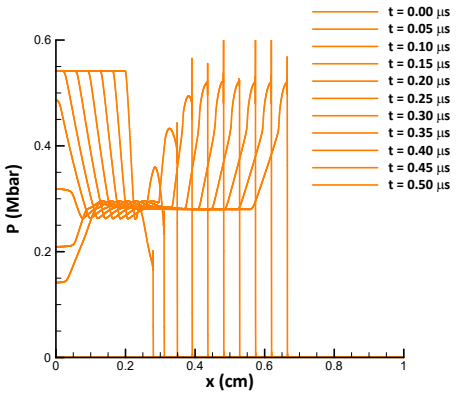

(e) 2500 ELM/cm

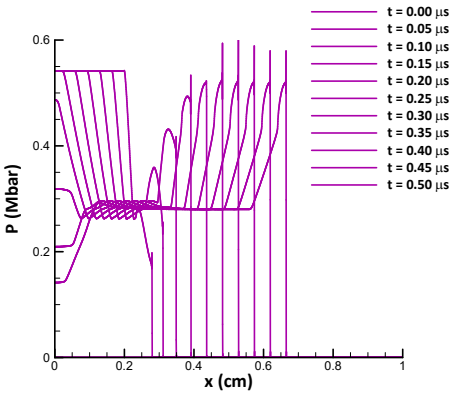

(f) 3000 ELM/cm

Figure 3.22: HMX sample shocked at various mesh densities using the Ignition and Growth model. Pressure versus position plots show the effect fidelity has on peak pressures.

Arrhenius model; therefore, results for this study are in the temperature domain. The left quarter of the domain is shocked to a pressure of $T = 3000K$. Experiments use a fixed time step of $\Delta t = 1 \times 10^{-4} \mu s$ with mesh sizes ranging from 500 elements per cm to 3000 elements per cm. Temperature profiles are shown on Figure 3.24(a)-3.24(f) at various times with an increment of $t_{plot} = 0.015 \mu s$ for a duration of $t = 0.25 \mu s$. These figures show the region of the domain where the material has reached steady detonation. For the initial study, Figure 3.24(a), the peak temperature at steady detonation is the initial temperature reaches $T = 3000K$. As fidelity increases, a spike forms and the peak temperature increases until converging to a temperature above the input shock. As an example, Figure 3.24(a) has a peak temperature of $T = 3250K$ after steady detonation. At $t = 0.25 \mu s$ the shock front of the $500 ELM/cm$ case reaches $x = 0.25 cm$. The shock front of the $2000 ELM/cm$ is located at $x = 0.20 cm$. When increasing fidelity further, the shock front of the $3000 ELM/cm$ is located at $x = 0.25 cm$ showing convergence. Furthermore, Figure 3.24(f) has a peak temperature $T = 3500K$. To study the convergence of detonation velocity, relative error is plotted on Figure 3.23(b) with the same target velocity . Each bar represents a varying mesh density corresponding to the color shown on Figures 3.24(a)-3.24(f). At the initial time t_1, the detonation velocity for the $500 ELM/cm$ case produces an error of greater than 20%. As the solution time increases, the error remains the same. Increasing mesh density increases the accuracy giving an error less than 5% for the $1000 ELM/cm$ case. Increasing mesh resolution produces an error of less than 1%. This shows that detonation velocity is resolved with the best value reported on Table 3.6 as $D = 0.911 cm/\mu s$. To summarize, mesh density affects peak temperature and detonation velocity for coarser meshes. Peak temperature increases with fidelity converging to a value of $T = 3500K$. Detonation velocity decreases with fidelity. Similar to the previous HMX experiment, calculations above 1000 elements per cm are adequate.

3.2.4 2D Results

This section considers a 2D domain, increasing the local degrees of freedom by an additional velocity component; see B for further details. The same experiments from Section 3.2.3 is repeated for PBX and HMX using the Ignition and Growth model. First, a $1.0 \times 0.5 cm$ sample of PBX is shocked at a pressure near $P = 0.55 Mbar$. Results for this experiment have a fixed time step of $\Delta t = 1^{-4} \mu s$ and are shown for a mesh density of 2000 elements per cm on Figures 3.25(a)-3.26(f). The x-axis and y-axis of these figures represents position in cm. The z-axis represents pressure in $Mbar$ for Figures 3.25(a)-3.25(f) and the burn fraction λ for Figures 3.26(a)-3.26(f). Each plot contains pressure and

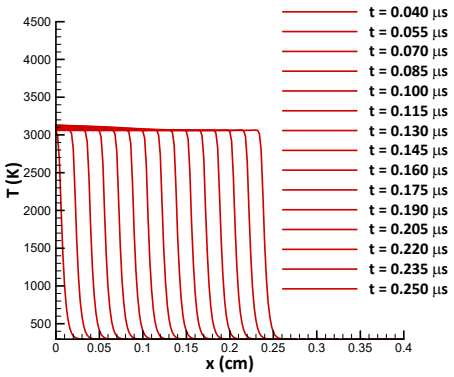

(a) 500 ELM/cm

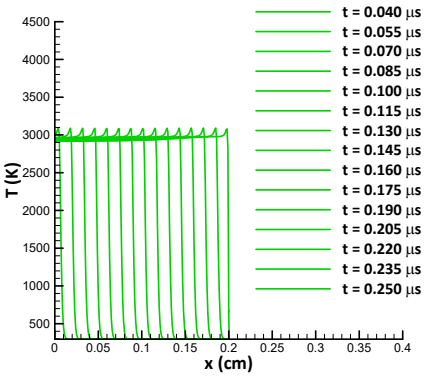

(b) 1000 ELM/cm

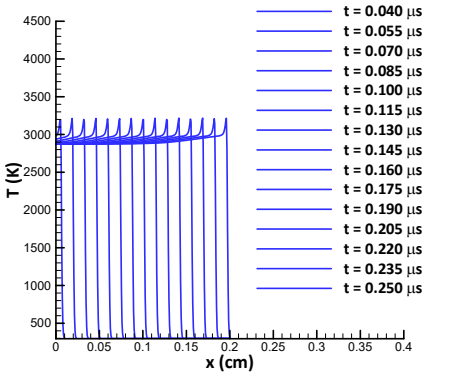

(c) 1500 ELM/cm

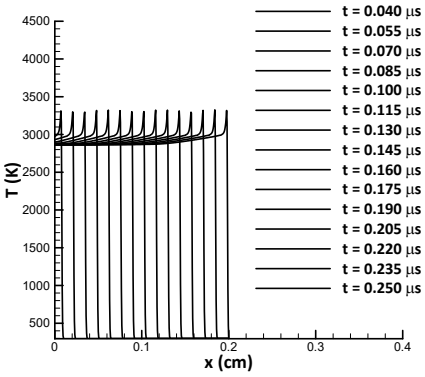

(d) 2000 ELM/cm

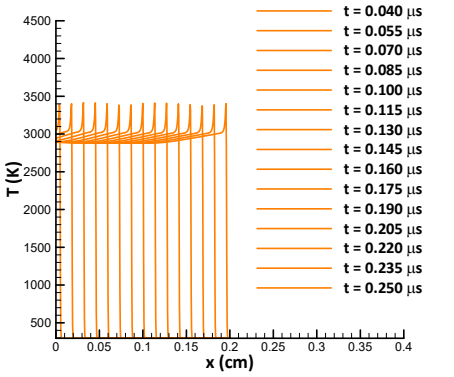

(e) 2500 ELM/cm

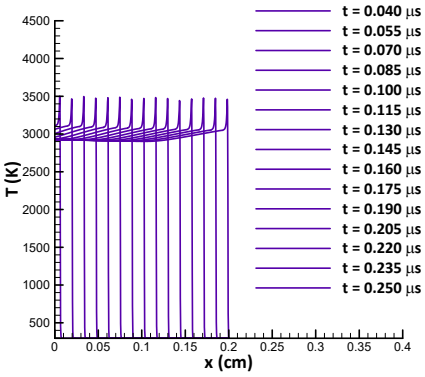

(f) 3000 ELM/cm

Figure 3.24: HMX sample shocked at various mesh densities using the Arrhenius model. Temperature versus position plots show the effect fidelity has on peak temperatures and detonation velocity.

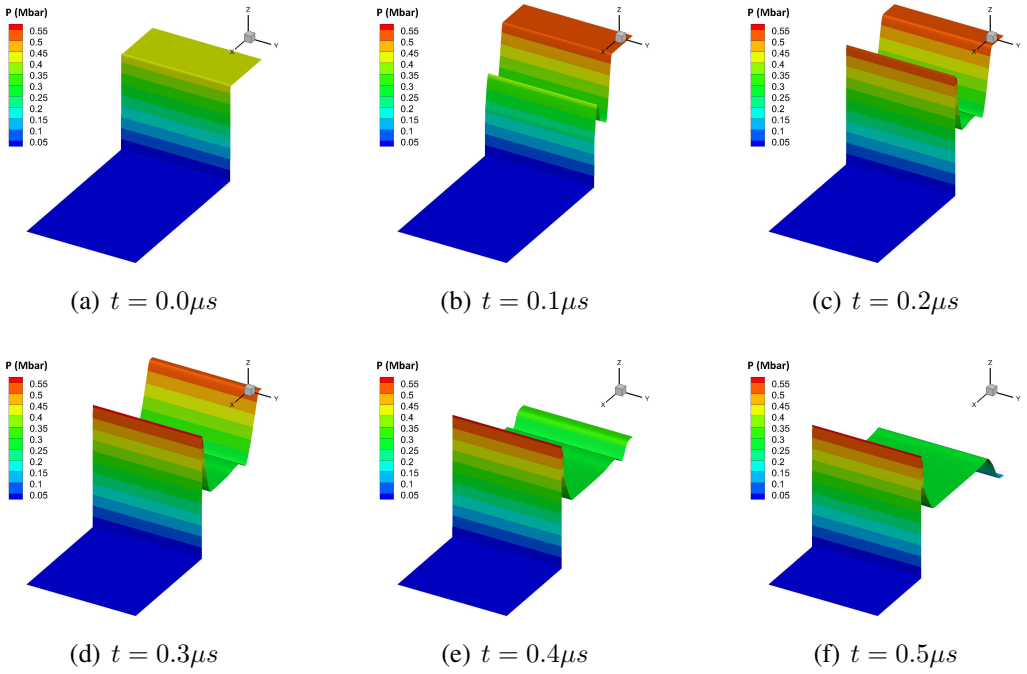

(a) $t = 0.0\mu s$ (b) $t = 0.1\mu s$ (c) $t = 0.2\mu s$

(d) $t = 0.3\mu s$ (e) $t = 0.4\mu s$ (f) $t = 0.5\mu s$

Figure 3.25: Shock loading of a $1.0 \times 0.5cm$ sample of PBX. Results are in good agreement with the corresponding 1D simulation.

burn fraction profiles at various times with an increment of $t_{plot} = 0.10\mu s$ for a duration of $t = 0.50\mu s$.

Figures 3.25(a)-3.25(f) shows the transition to steady detonation. The peak pressure reaches the value of $P = 0.565Mbar$ with the detonation wave traveling at the speed of $D = 0.880cm/\mu s$. This simulation is in good agreement with the corresponding 1D simulation shown on Figure 3.20(d). Figures 3.26(a)-3.26(f) show the material is initially a pure solid at $t = 0.0$. As the solution progresses the material reacts and converts to gaseous product as the detonation wave travels through. Next a sample of HMX is shocked to a pressure of $P = 0.55Mbar$. Again, a mesh density of 2000 elements per cm is used. Pressure profiles are shown on Figures 3.27(a)-3.27(f) with the same increments and duration. Steady detonation is achieved with a peak pressure of $P = 0.57Mbar$ and a detonation speed of $D = 0.915cm/\mu s$. This simulation is in good agreement with the corresponding 1D simulation shown on Figure 3.22(d). Figures 3.28(a)-3.28(f) show the burn fraction λ for the HMX experiment.

Finally, a $2.0 \times 2.0cm$ domain is considered with a circular initial discontinuity located at the center of the domain. The purpose of this test is to assess the unidirectional capability of the solution procedure. The shock front is represented as a circle that expands as the detonation proceeds, with an initial radius of $r = 0.25cm$. A uniform mesh is considered

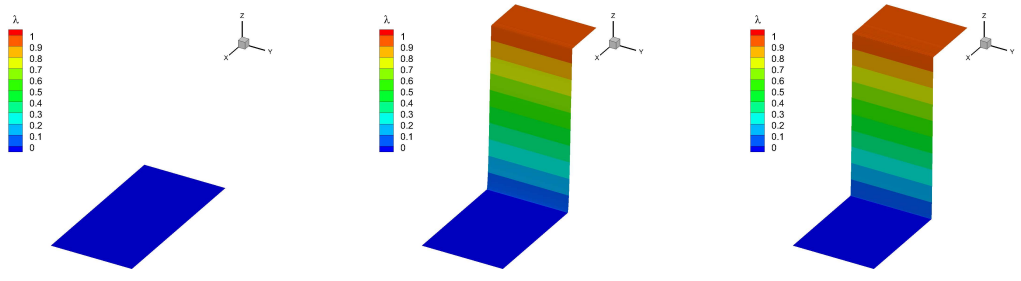

(a) $t = 0.0\mu s$ (b) $t = 0.1\mu s$ (c) $t = 0.2\mu s$

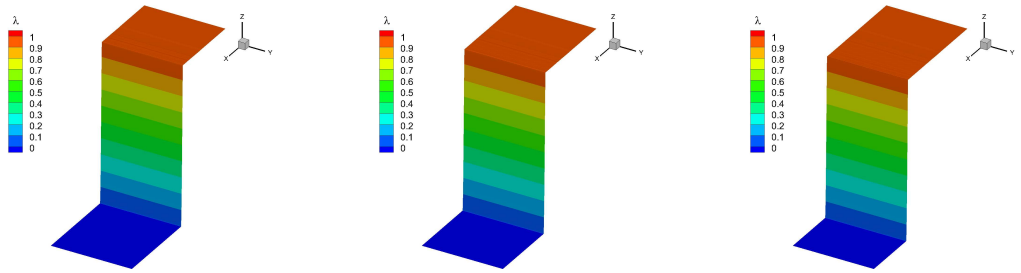

(d) $t = 0.3\mu s$ (e) $t = 0.4\mu s$ (f) $t = 0.5\mu s$

Figure 3.26: Burn fraction of PBX. Initially a pure solid, the material reacts and converts to gaseous products

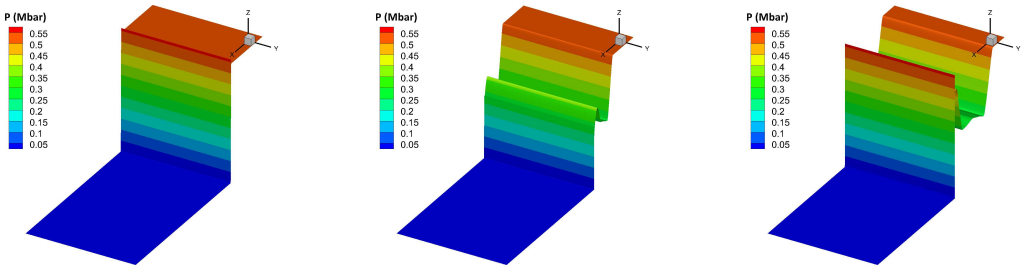

(a) $t = 0.0\mu s$ (b) $t = 0.1\mu s$ (c) $t = 0.2\mu s$

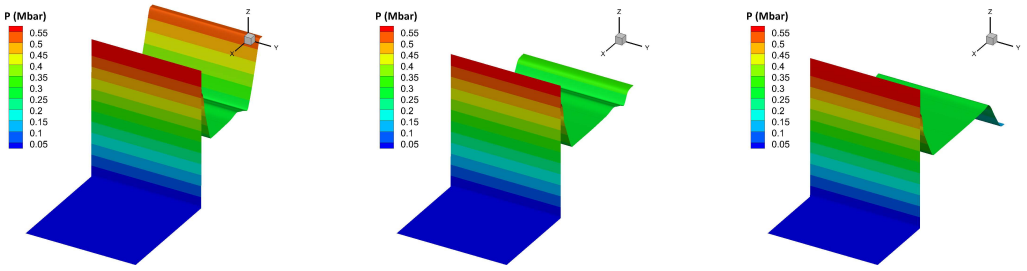

(d) $t = 0.3\mu s$ (e) $t = 0.4\mu s$ (f) $t = 0.5\mu s$

Figure 3.27: Shock loading of a $1.0 \times 0.5cm$ sample of HMX. Results are in good agreement with the corresponding 1D simulation.

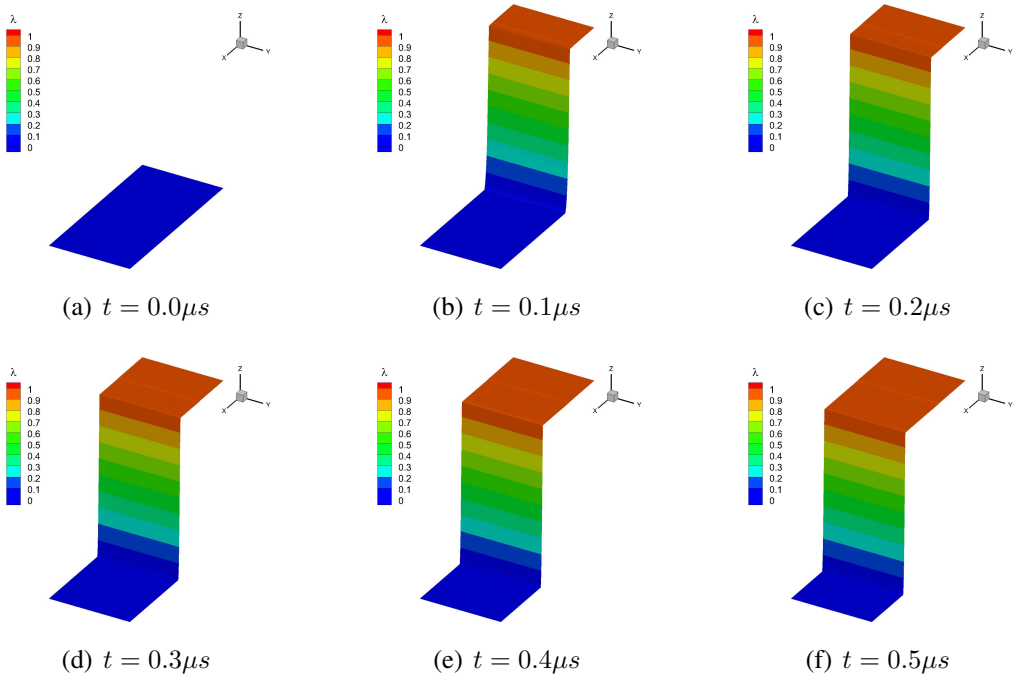

(a) $t = 0.0\mu s$ (b) $t = 0.1\mu s$ (c) $t = 0.2\mu s$

(d) $t = 0.3\mu s$ (e) $t = 0.4\mu s$ (f) $t = 0.5\mu s$

Figure 3.28: Burn fraction of PBX. Initially a pure solid, the material reacts and converts to gaseous products

using the 4-noded linear quadrilateral element developed in Section 2.2. The same mesh resolution and time step is used. Figures 3.29(a)-3.29(c) show pressure contours of shock loading of PBX with Figures 3.29(d)-3.29(f) showing the corresponding burn fractions. Plots vary by increments of $t_{plot} = 0.2\mu s$ for a duration of $t = 0.4\mu s$. Figure 3.29(a)-3.29(f) indicates that the detonation profile maintains a symmetric circular shape with a shock front traveling at a constant speed. Values for this results will be reported and studied in future sections. Figures 3.30(a)-3.30(f) show pressure and burn fraction contours of shock loading of HMX.

3.3 Summary

This chapter thoroughly validated numerical results using the continuum methods with experimental results. Numerical results compared with analytically obtained test problems showed good agreement. The free smoothing parameters were investigated in the context of these solutions showing their effects on the average error per node. Equations of state for PBXs, HMX and polymeric binder were investigated in density-energy space. Numerical results for the shock Hugoniot show good agreement with the experimental curve fit signifying that the pre and post shock states are captured accurately. Run-to-detonation

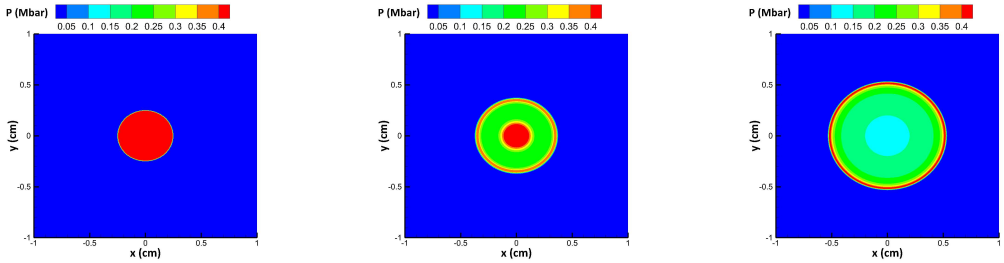

(a) $t = 0.0\mu s$ (b) $t = 0.2\mu s$ (c) $t = 0.4\mu s$

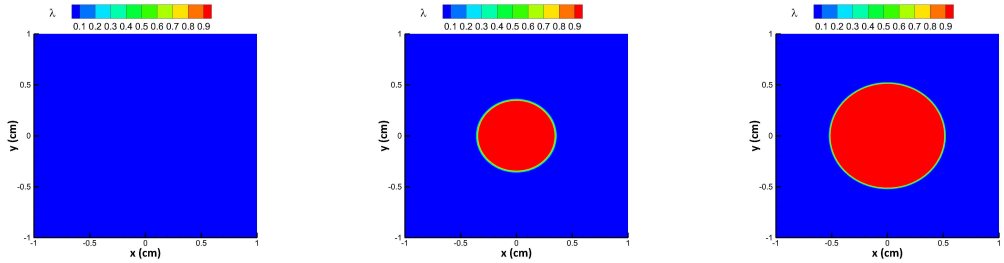

(d) $t = 0.0\mu s$ (e) $t = 0.2\mu s$ (f) $t = 0.4\mu s$

Figure 3.29: Results for pressure and burn fraction of circular shock loading of PBX. Detonation profile maintains a symmetric circular shape demonstrating the unidirectional capability of the solution procedure.

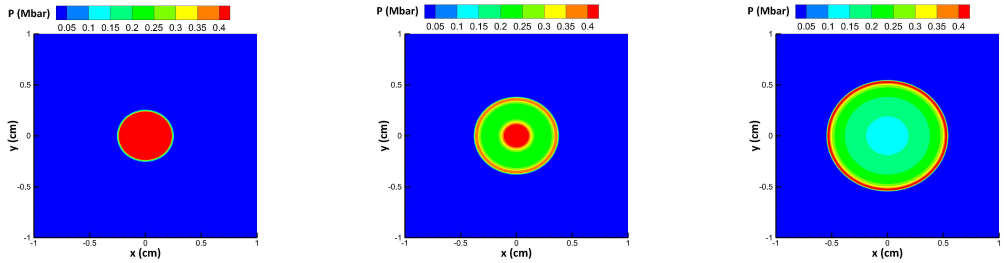

(a) $t = 0.0\mu s$ (b) $t = 0.2\mu s$ (c) $t = 0.4\mu s$

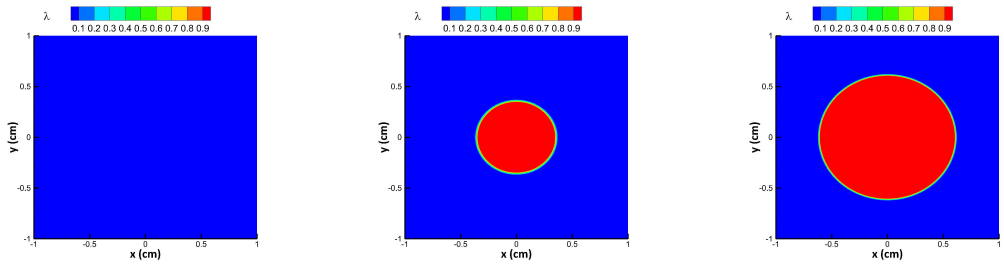

(d) $t = 0.0\mu s$ (e) $t = 0.2\mu s$ (f) $t = 0.4\mu s$

Figure 3.30: Results for pressure and burn fraction of circular shock loading of HMX. Detonation profile maintains a symmetric circular shape demonstrating the unidirectional capability of the solution procedure.

numerical studies were conducted with Ignition and Growth models and Arrhenius models for PBXs and HMX. The transition from incident pressure shock to steady detonation was captured for multiple experiments and used to create pop-plots. These plots agreed well with experimental results validating the numerical model used. Mesh densities studies were conducted to assess the accuracy of shock features. Results show good agreement with the various shock quantities including detonation velocity. Finally, 2D experiments of shock loading matched well with 1D experiments. This chapter showed that many quantities and features associated with detonation of PBXs are accurately captured with the solution method, establishing a validated baseline with which to compare other methods in future chapters.

CHAPTER 4

Direct Numerical Simulation

This chapter presents Direct Numerical Simulation (DNS) of shock loading of polymer bonded explosives. These methods explicitly model material heterogeneities where both the binder and HMX are represented. First, synthetic microstructures of polymer bonded explosives are generated using a Markov Random Field approach. Section 4.1 presents the mathematical model used to generate these microstructures at various mass fractions. Section 4.2 investigates shock initiation for various microstructures at different loading conditions. These findings are compared to the continuum approach described in the previous Chapter. Finally, Numerical results for volume averages of pressure and temperature are presented as functions of time.

4.1 Generating Synthetic Microstructures using Markov Random Fields

Microstructures are stochastic in nature and a single snapshot of the microstructure does not give its complete variability. However, it is known that different windows taken from a polycrystalline microstructure generally 'look alike' [135]. In mathematical terms, this amounts to the presence of a stationary probability distribution from which various microstructural snapshots are sampled. There are various ways of modeling this probability distribution indirectly. Feature–based algorithms have long been used that categorize various microstructural snapshots based on a common set of underlying features, and generate new synthetic images with similar features [136–138]. These features could include marginal histograms [136], multiresolution filter outputs (Gaussian [137] and wavelet [138] filters) and point probability functions (eg. autocorrelation function) [139]. These methods are good at capturing the global features of the image, however local information in the form of per–pixel data is lost. Thus, features such as grain boundaries are smeared out when reconstructing polycrystalline structures [138].

Alternatively, one could start with sampling the conditional probability density for the state of a pixel given the known states of its neighboring pixels using reference 2D or 3D experimental images. If only the nearest neighbors are chosen, this amounts to sampling from a Ising–type model [140]. For general microstructures, the correlation lengths can span several pixels [139] and a larger neighbor window may be needed. In this chapter, generalized Ising models called Markov Random Fields (MRFs) are employed to model the probability distribution. While in Ising models, a lattice is constructed with pixels (with binary states) interacting with its nearest neighbors, in MRFs, pixels take up integer or vector states and interact with multiple neighbors over a window. The sampling of conditional probability of a pixel given the states of its known neighbors is based on Claude Shannon's generalized Markov chain [141]. In the one-dimensional problem, a set of consecutive pixels is used as a template to determine the probability distribution function (PDF) of the next pixel.

Non-parameteric sampling approaches have been developed [142] for extending the sampling technique to 2D microstructures. In this approach, microstructures are grown layer–by–layer from a small seed image (3x3 pixels) taken randomly from the experimental micrograph. Here, the algorithm first finds all windows in an experimental micrograph that are similar to an unknown pixel's neighborhood window. One of these matching windows is chosen and its center pixel is taken to be the newly synthesized pixel. This technique is popular in the field of 'texture synthesis' [142–145], in geological material reconstruction literature where such sampling methods are termed 'multiple-point statistics' [146], and more recently, has been applied for modeling polycrystalline microstructures [147].

An alternate methodology based on optimization has become popular in recent years. The non-parameteric sampling method [142] is posed in the form of an expectation maximization algorithm [148–151]. The approach minimizing a neighborhood cost function that ensures that the local neighborhood of the Ising lattice taken along the x-,y- or z- directions through the 3D microstructure is similar to some neighborhood in the 2D lattice imaged along that plane. This reconstruction problem leads to anisotropic microstructures that have similar high order statistics [150], which is in contrast to other such works in literature that use assumptions of microstructural isotropy [152] or methods that use lower order statistics such as two-point correlation functions to synthesize 3D microstructures [153, 154]. The sampling approach and the optimization approach was used to create synthetic microstructures for PBXs.

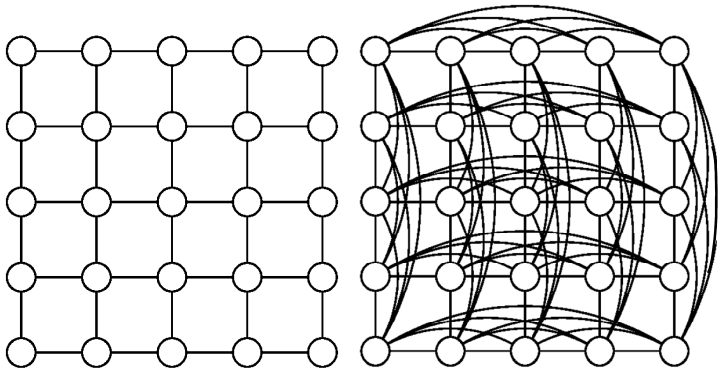

(a) (b)

Figure 4.1: Markov random field as an undirected graph model, circles are pixels in the image and bonds are used to connect neighbors: (a) Ising model with nearest neighbor interactions (b) Microstructure modeled by including higher order interactions in the Ising model.

4.1.1 Mathematical modeling of Microstructures

Some of early attempts at microstructure modeling were based on Ising models [140]. In the Ising model, a $N \times N$ lattice (L) is constructed with values X_i assigned for each particle i on the lattice, $i \in [1, .., N^2]$. In an Ising model, X_i is a binary variable equal to either $+1$ or -1 (eg. magnetic moment). In general, the values X_i may contain any one of G color levels in the range $\{0, 1, .., G-1\}$ (following the integer range extension of the Ising model in Ref. [155]). A *coloring* of L denoted by $\boldsymbol{X}$ maps each particle in the lattice L to a particular value in the set $\{0, 1, .., G-1\}$. Ising models fall under the umbrella of undirected graph models in probability theory. In order to rewrite the Ising model as a graph, neighbors are assigned to particles and link pairs of neighbors using a bond as shown in Fig. 4.1(a). The rule to assign neighbors is based on a pairwise Markov property. A particle j is said to be a neighbor of particle i only if the conditional probability of the value X_i given all other particles (except (i, j), i.e., $p(X_i|X_1, X_2, .., X_{i-1}, X_{i+1}, .., X_{j-1}, X_{j+1}, .., X_{N^2})$) depends on the value X_j.

Note that the above definition does not warrant the neighbor particles to be close in distance, although this is widely employed for physical reasons. For example, in the classical Ising model, each particle is bonded to the next nearest neighbor as shown in Fig. 4.1(a). For modelling microstructures, a higher order Ising model (Fig. 4.1(b)) is used. The particles of the lattice correspond to pixels of the 2D microstructure image. The neighborhood of a pixel is modeled using a square window around that pixel and bonding the center pixel to every other pixel within the window [156]. Using this graph structure, a Markov random field can be defined as the joint probability density $P(\boldsymbol{X})$ on the set of all possible colorings

$\boldsymbol{X}$, subject to a local Markov property. The local Markov property states that the probability of value X_i, given its neighbors, is conditionally independent of the values at all other particles. In other words, $P(X_i|\text{all particles except i}) = p(X_i|\text{neighbors of particle i})$. Next, we describe a method based on Ref. [142] to sample from the conditional probability density $p(X_i|\text{neighbors of voxel i})$. The following sections present methods to sample from the conditional probability density for generation of synthetic 2D and 3D microstructures.

4.1.2 Spatial Sampling

In this section, the MRF algorithm used to estimate microstructures over larger spatial regions from experimentally known 2D microstructures is described. Here, the color (X_i) of a pixel i is represented using G color levels in the range $\{0, 1, .., G-1\}$ each of which maps to an RGB triplet. The number of color levels is chosen based on the microstructure to be reconstructed; e.g. for binary images $G = 2$. Let $\boldsymbol{E}$ and $\boldsymbol{S}$ denote the experimental and synthesized microstructure, respectively. Let v be a pixel in $\boldsymbol{S}$ whose color needs to inferred using the sampling procedure. Let $\boldsymbol{S}_v$ denote the colors in a neighborhood window around pixel v. Let $\boldsymbol{E}^w$ denote the colors of pixels in a window of the same size in the input 2D micrograph.

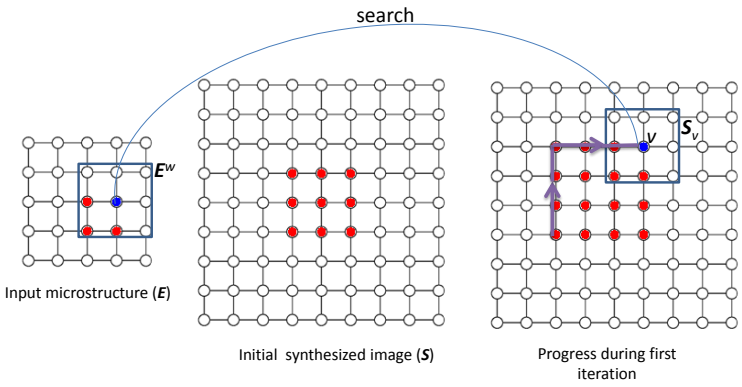

Figure 4.2: The Markov random field approach: The image is grown from a 3x3 seed image (center). As the algorithm progresses along the path shown (right), the unknown output pixel (shown in blue) is computed by searching for a pixel with a similar neighborhood in the input image (left).

In order to find the coloring of pixel v, the conditional probability density $p(X_v|\boldsymbol{S}_v)$ needs to be computed. Explicit construction of such a probability density is often computationally intractable. Instead, the most likely value of v is identified by first finding a window $\boldsymbol{E}_v$ in the input 2D micrograph that is most similar to $\boldsymbol{S}_v$ (see Fig. 4.2). This is done by solving the following problem (where $\boldsymbol{S}_{v,u}$ denotes the color of pixel u in $\boldsymbol{S}_v$ and

$\boldsymbol{E}_u^w$ denotes the color of pixel u in $\boldsymbol{E}^w$):

$$\boldsymbol{E}_v = \arg \min_{\boldsymbol{E}^w} \sum_u \omega_{v,u} (\boldsymbol{S}_{v,u} - \boldsymbol{E}_u^w)^2 \tag{4.1}$$

where, $D = \sum_u \omega_{v,u} (\boldsymbol{S}_{v,u} - \boldsymbol{E}_u^w)^2$ is a distance measure defined as the normalized sum of weighted squared differences of pixel colors. In order to preserve the short range correlations of the microstructure as much as possible, the weight for nearby pixel is taken to be greater than pixels farther away (Gaussian weighting function ω is used). If the pixel u is located at position (x, y) (in lattice units) with respect to the center pixel v (located at $(0, 0)$), $\omega_{v,u}$ is given as:

$$\omega_{v,u} = \frac{\exp(-\frac{(x^2+y^2)}{2\sigma^2})}{\sum_i \sum_j \exp(-\frac{(i^2+j^2)}{2\sigma^2})} \tag{4.2}$$

Here, the summation in the denominator is taken over all the known pixels in $\boldsymbol{S}_v$. The weights $\omega_{v,u}$ for the unknown pixels in $\boldsymbol{S}_v$ are taken to be zero. This ensures that the distance measure is computed only using the known values and is normalized by the total number of known pixels. The standard deviation (σ) is taken to be $0.16w$.

The most similar window, shown by Eq. 4.1, is solved using an exhaustive search by comparing all the windows in the input 2D micrograph to the corresponding neighborhood of pixel v. In this approach, a measure of stochasticity is introduced by storing all matches with a distance measure that is within 1.3 times that of the best matching window [142]. The center pixel colors of all these matches give a histogram for the color of the unknown pixel (X_v), which is then sampled using a uniform random number.

The synthetic microstructure is grown layer–by–layer starting from a small seed image (3x3 pixels) taken randomly from the experimental micrograph (Fig. 4.2). In this way, for any pixel the values of only some of its neighborhood pixels will be known. Each iteration in the algorithm involves coloring the unfilled pixels along the boundary of filled pixels in the synthesized image as shown in Fig. 4.2. An upper limit of 0.1 is enforced for the distance measure initially. If the matching window for a unfilled pixel has a larger distance measure, then the pixel is temporarily skipped while the other pixels on the boundary are filled. If none of the pixels on the boundary can be filled during an iteration, then the threshold is increased by 10% for the next i iteration.

The window size is the only adjustable parameter for different microstructures. Window size plays an important role in the MRF model. At window sizes much smaller than the correlation lengths, false matches lead to high noise in the reconstructions. At very high window sizes, not enough matching windows can be identified. Hence, there is an ideal window size that needs to be found through numerical trial. Results in this work use a

window size of 11, the optimal size.

The fundamental approximation in this numerical implementation is that the probability distribution function (PDF) of an unfilled pixel is assumed to be independent of the PDF of its unfilled neighbors. In other words, PDF for a pixel that is obtained by sampling may not stay valid as the rest of its neighbors are filled in. One problem with this approach is the tendency to occasionally slip into a wrong part of the search space and start growing large grains. Feature mapping [157] and k-coherence techniques [158] have been recently developed that largely address this issue. Simple color differences often fail to recognize semantic structure (e.g. grain boundary segregated phases between grains). The introduced of a feature mask helps to guide the synthesis process used within a MRF pixel-based scheme [159]. The idea is to include grain boundaries as an additional image channel prior to neighborhood analysis. The weight w given to the feature-distance channel can be varied [157]. The tradeoff is that a larger weight w downplays color differences, eventually resulting in synthesis noise.

When colors are copied from input to output during the synthesis process, it is very unlikely that they will land on random output locations. Instead, colors that are together in the input (eg. each grain in a polycrystal) ought to have a tendency to be also together in the output. This concept is called coherence [158]. Similar ideas have also appeared in other methods such as jump maps [160] and k-coherence [161]. During initialization, a similarity-set is built for each input pixel which contains a list of other pixels with similar neighborhoods. During synthesis, the algorithm copies pixel from the input to the output, but in addition to colors, the source pixel location is also copied. The algorithm gives significant improvement in reproduction of color information (in the form of crystal orientations or phases) and even exceeds the performance of exhaustive search algorithms [162]. The sampling algorithm can also be extended towards generating 3D synthetic microstructures from 3D experimental images.

4.1.3 3D Optimization

In this section, the reconstruction of 3D microstructures from three orthogonal 2D sectional images taken along the x-, y- and z- planes is developed. The information contained in these three 2D micrographs is in the form of pixels containing colors corresponding to different constituent phases. The outcome of the reconstruction is a 3D microstructure containing voxels colored consistently such that any arbitrary x-, y- or z- slice 'looks' similar to the corresponding input micrographs.

In this section, let $\boldsymbol{E}^x$, $\boldsymbol{E}^y$ and $\boldsymbol{E}^z$ denote the set of orthogonal (x, y and z, respectively)

slices of the experimental microstructure. Let $\boldsymbol{V}$ denote the solid (3D) microstructure. The color of voxel v in the 3D microstructure is denoted by X_v. In addition to the color (e.g. RGB triplet), the vector X_v may also contain other values including grain orientation and phase index. Here, the color is represented using G color levels in the range $\{0, 1, .., G-1\}$ each of which maps to an RGB triplet. The number of color levels is chosen based on the microstructure to be reconstructed; again $G = 2$ for binary images.

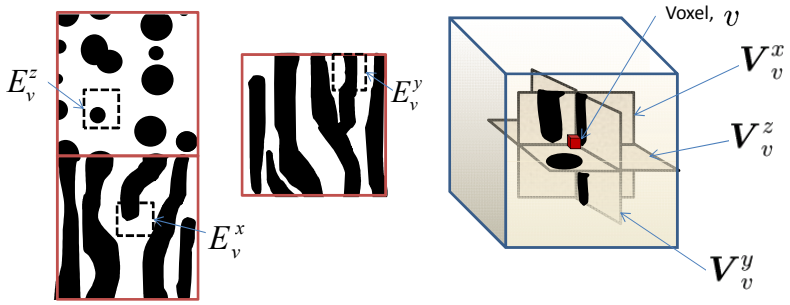

Figure 4.3: The neighborhoods of v in the slices orthogonal to the x, y, and z axis, respectively, are shown. The windows in the input 2D micrograph shown in dotted lines are denoted by $\boldsymbol{E}_v^i$ $(i = x, y, z)$. These windows closely resemble the neighborhoods of v.

The vectors denoting the spatial neighborhood of voxel v in the slices orthogonal to the x, y, and z axis, respectively, are denoted as $\boldsymbol{V}_v^x$, $\boldsymbol{V}_v^y$, and $\boldsymbol{V}_v^z$, as shown on Figure 4.3. The neighborhood is taken over a small user-assigned window around the voxel v. Let $\boldsymbol{E}^{x,w}$, $\boldsymbol{E}^{y,w}$, and $\boldsymbol{E}^{z,w}$ denote a window of the same size in the input 2D micrographs. In order to find the coloring of voxel v based on the neighbor voxels in the x–plane, one needs to compute the conditional probability density $p(X_v|\text{color of x–plane neighbors of } v)$. Explicit construction of such a probability density is often computationally intractable. Instead, the most likely value of v is identified by first finding a window $\boldsymbol{E}^{x,w}$ that is most similar to $\boldsymbol{V}_v^x$ in the input 2D micrograph. This window is denoted by $\boldsymbol{E}_v^x$ as shown on Figure 4.3. Similarly, matching windows to the y– and z– plane neighborhoods of voxel v in the corresponding 2D sectional image, denoted as $\boldsymbol{E}_v^y, \boldsymbol{E}_v^z$, are found. Each of these matching windows $\boldsymbol{E}_v^x, \boldsymbol{E}_v^y, \boldsymbol{E}_v^z$ may have different coloring of the center pixel. Thus, an optimization methodology to effectively merge these disparate values and identify a unique coloring for voxel v is needed. The optimization approach is described next.

Let the value $\boldsymbol{V}_{v,u}^x$ denotes the color of voxel u in the neighborhood $\boldsymbol{V}_v^x$. Similarly, the value $\boldsymbol{E}_{v,u}^x$ and $\boldsymbol{E}_u^{x,w}$, respectively, denote the color of pixel u in the window $\boldsymbol{E}_v^x$ and $\boldsymbol{E}^{x,w}$.

The 3D microstructure is synthesized by posing the problem as a L^2 minimization of the energy [148]:

$$\boldsymbol{V}^* = \arg \min_{\boldsymbol{V}} \sum_{i \in \{x,y,z\}} \sum_{v} \sum_{u} \omega^i_{v,u} (\boldsymbol{V}^i_{v,u} - \boldsymbol{E}^i_{v,u})^2 \tag{4.3}$$

where, $\boldsymbol{V}^*$ is the optimum synthetic microstructure. The optimization is carried out in two steps as in the 2D case. In the first step, the energy is minimized with respect to $\boldsymbol{E}^i_v$. In this step, we assume that the most likely sample from the conditional probability distribution of the center pixel in the 3D image (eg. $p(X_v|$colors of x–plane neighbors of $v)$) is the center pixel of a best matching window in an experimentally obtained 2D slice on the corresponding plane. The best matching neighborhood of voxel v along the x–plane is selected by solving the following problem:

$$\boldsymbol{E}^x_v = \arg \min_{\boldsymbol{E}^{x,w}} \sum_{u} \omega^x_{v,u} (\boldsymbol{V}^x_{v,u} - \boldsymbol{E}^{x,w}_u)^2 \tag{4.4}$$

This is an exhaustive search that compares all the windows in the input 2D micrograph to the corresponding x–slice neighborhood of voxel v and identifies a window that leads to a minimum weighted squared distance. In this process, for 2D images of size 64×64 with a 16×16 neighborhood window, a matrix of size $16^2 \times (64 - 16)^2$ is built containing all possible neighborhoods of pixels that have a complete 16^2 window around it. The column in this matrix that has a minimum distance to the 3D slice $\boldsymbol{V}^x_v$ is then found through a k–nearest neighbor algorithm [163]. Note that, only a limited 2D experimental sample along each cross–section is given, which means that the best match may not be an exact match for $\boldsymbol{V}^x_v$.

Thus, for each voxel v, a set of three best matching neighborhoods are obtained, possibly with different colors corresponding to the center pixel. A unique value of v thus needs to be found by weighting colors pertaining to location v in not only the matching windows of voxel v but also its neighbors. This is exactly done in the second step of the optimization procedure, where the optimal color of voxel v is computed by setting the derivative of the energy function with respect to X_v to zero. This leads to a simple weighted average expression for the color of voxel v:

$$X_v = \Big(\sum_{i \in \{x,y,z\}} \sum_{u} \omega^i_{u,v} \boldsymbol{E}^i_{u,v} \Big) / \Big(\sum_{i \in \{x,y,z\}} \sum_{u} \omega^i_{u,v} \Big) \tag{4.5}$$

As in the 2D case, the subscripts u and v are switched in the above expression as compared to Eq. 4.3. This implies that the optimal color of the voxel v is the weighted average of the colors at locations corresponding to voxel v in the best matching windows

($\boldsymbol{E}_u^i$) of voxels (u) in the solid microstructure. Since X_v changes after this step, the set of closest input neighborhoods $\boldsymbol{E}_v^i$ will also change. Hence, these two steps were repeated until convergence, i.e., until the set $\boldsymbol{E}_v^i$ stops changing. As a starting condition, a random color from the input 2D images is assigned to each voxel v. The process is carried out in a multiresolution (or multigrid) fashion [149]: starting with a coarse voxel mesh and interpolating the results to a finer mesh once the coarser 3D image has converged to a local minimum. Three resolution levels ($16^3, 32^3$ and 64^3) are used.

4.1.4 Synthetic Microstructures of Polymer-Bonded Explosives

For this treatment, a binary representation is considered; i.e. a single pixel represents either HMX(black) or polymeric binder(white). A 64×64 pixel seed image is used to generate a larger microstructure. The seed image (Figure 4.5 (left)) is a cut taken from an experimental micrograph [94] and converted to a binary representation, with a volume fraction near $\eta = 0.63$. The scale associated with seed image is $0.5mm$. The final synthetic microstructure size is chosen to be $5.0mm$, an order of magnitude increase. Figure 4.1.4 shows the various iterations of the sampling scheme described in Section 4.1.2. The algorithm initiates at the center of the synthetic microstructure, building outward layer by layer. This process produces the final synthetic microstructure shown in Figure 4.5(right), next to the seed image.